Université catholique de Louvain
Institute of Neuroscience
Institute of Information and Communication Technologies, Electronics and Applied Mathematics

Finger pad mechanics, tactile signals and dexterous manipulation

Allan Barrea

Ph.D. dissertation submitted in line with the requirements for the degree of
Docteur en sciences de l'ingénieur

Dissertation committee:

Prof. Jean-Louis Thonnard (UCL, advisor)
Prof. Philippe Lefèvre (UCL, advisor)
Prof. Ingvars Birznieks (UNSW Sydney, Australia)
Prof. Hannes Saal (University of Sheffield, United Kingdom)
Dr. Benoit Delhaye (University of Chicago, IL, USA)
Prof. André Mouraux (UCL)
Prof. Thomas Pardoen (UCL, secretary)
Prof. Christophe De Vleeschouwer (UCL, chairman)

November 27, 2017

À mes parents et ma sœur, qui m'ont toujours poussé à donner le meilleur de moi-même.

À Céline, qui m'aide chaque jour à y arriver.

Remerciements

Qu'est-ce qui pourrait bien pousser un ingénieur en robotique à se lancer dans une thèse sur le sens du toucher, à cheval entre mécanique et neurosciences, dans un domaine qu'il ne maîtrise pas ? Dans mon cas, ce grand saut dans l'inconnu a été motivé par la volonté de me confronter à un domaine totalement nouveau dont je sentais confusément qu'il allait m'apporter beaucoup, mais surtout par une bonne dose d'inconscience. On pourrait résumer mes motivations par « Ça a l'air fun, allons-y ». Avec le recul, le fait que l'offre d'emploi mentionnait la participation à des vols paraboliques et que l'ESA finançait tout le projet y a sans doute aussi été pour quelque chose…

Après ces quatre années de recherche, je peux affirmer que je ne regrette pas un seul instant de m'être lancé dans cette aventure scientifique, qui m'aura apporté bien plus que les connaissances résumées dans l'ouvrage que vous tenez entre vos mains. Quand je regarde en arrière pour contempler le chemin parcouru, je me rends compte du nombre de personnes brillantes que j'ai rencontrées et avec lesquelles j'ai eu la chance d'interagir. L'horizon de ma conscience s'est considérablement élargi et cette thèse m'a permis de quitter le cadre mental un peu confiné qui était le mien en sortant de mon master en robotique. J'ai pris conscience de l'incroyable diversité que représente la recherche tant fondamentale qu'appliquée. J'ai découvert et mis en pratique la démarche scientifique expérimentale, j'ai appris à formuler mes hypothèses sous la forme de questions de recherche rigoureuses et originales, je me suis ouvert aux sciences du vivant, et j'ai acquis une expérience pratique dans de nombreux domaines allant de l'optique aux statistiques en passant par le traitement d'image et l'acquisition de données.

Tout cela n’aurait pas été possible sans mes promoteurs, mes collègues, mes amis et ma famille. Aussi, je tiens à dédier le reste de cette section à les remercier, en espérant n’oublier personne, et en m’excusant d’avance auprès de ceux que j’omettrai bien malgré moi de mentionner.

Jean-Louis, ton intérêt et ton enthousiasme pour mon sujet de recherche ont été et restent pour moi un énorme facteur de motivation. Je te remercie pour ta capacité à énoncer clairement les objectifs de recherche et à garder les yeux fixés dessus même quand les résultats expérimentaux ne sont pas ceux attendus. Philippe, ton calme et ta précision m’ont été d’une grande aide tout au long de cette thèse et je continuerai à m’en inspirer tout au long de ma vie. Tes qualités se combinent parfaitement avec celles de Jean-Louis et à deux vous formez un duo imparable, motivant et rigoureux. Vous m’avez apporté beaucoup sur le plan professionnel mais aussi personnel et je vous en remercie.

Même si je n’ai officiellement que deux promoteurs, je dois bien avouer, Benoît, que tu as joué le rôle d’un promoteur à part entière, en me formant lors de mon arrivée, et ensuite en m’épaulant au quotidien tout au long de mon doctorat. Je te dois plus que je ne peux l’exprimer ici, et je t’en suis de tout cœur reconnaissant.

Je tiens à remercier également les autres membres de mon jury pour leurs commentaires éclairés qui m’ont permis d’améliorer ce texte : Pr. Ingvars Birznieks, Pr. Hannes Saal, Pr. André Mouraux, Pr. Thomas Pardoen et Pr. Christophe De Vleeschouwer. Je remercie également les équipes de recherche avec lesquelles j’ai collaboré et m’ont beaucoup apporté sur le plan scientifique : Pr Benoni Edin, Dr Ewa Jarocka, Pr Cornelius Schwarz, Maysam Oladazimi, Pr Cagatay Basdogan, and Omer Sirin.

En plus de l’équipe de choc formée par les personnes mentionnées ci-dessus, ces quatre années n’auraient pas été les mêmes sans la présence à mes côtés de David, qui a partagé mon bureau et mon quotidien durant toute la durée de mon doctorat. Je te remercie pour ton oreille attentive durant les moments de doute, pour ton calme quand j’en avais besoin et pour ton soutien sans faille. Je suis certain que notre amitié qui s’est tissée durant ces quatre ans continuera de grandir.

Je remercie également les membres de mon groupe de recherche, les anciens comme les nouveaux : Vincent, Thibault, Caroline, Jean-Jacques, Frédéric, Florian, Nicolas D., David G., Nasia, Oyéné, Laurent, Félicien, Antoine et Ghady. La bonne ambiance qui règne au sein du groupe est le fruit des efforts de chacun et partager votre expérience a été un réel plaisir.

Le support technique dont j'ai bénéficié a été un facteur déterminant dans l'aboutissement de mes projets. Pour leur aide pratique et leurs conseils, je tiens à remercier Julien L., Cécile, Sébastien, Christian, Benvenuto, François W., Etienne, Benoît H. et Massimo. Pour leur soutien administratif et pour les nombreux bons de commandes et notes de frais traités avec le sourire, je remercie Isabelle, Marie-Christine, Leila, Khira, Véronique, Cathy, Nathalie, Astrid et Pascale.

J'ai également beaucoup apprécié le fait de réaliser mes recherches au sein de deux instituts différents, à savoir l'ICTEAM à Louvain-la-Neuve et l'IoNS à Bruxelles. Je n'oublierai jamais la bonne ambiance qui règne au sein du bâtiment Euler, dont la vie quotidienne bouillonnante rend parfois difficile de se concentrer sur ses recherches. Pour les tartes, les team buildings, les tournois de kicker et pour tout le reste, je remercie Martin, Matthew, Corentin, Benjamin, Luc, François G., Pierre-Yves C., Adrien, Adeline, Romain, Nicolas B., Maguy, Balázs Emilie, Estelle, Pierre-Alexandre, Maxime, Matthieu G., Philippe D., Julien H., Jean-Charles, l'équipe du Club Elec, celle de l'IEEE Student Branch et tous les autres. Du côté de Woluwé, je remercie les collègues avec qui j'ai eu la chance de partager mon quotidien : Charlotte, Camille, Lieve, Roxanne, Emanuel, Diana, Emanuele, Giulia, Erwan, Cédric, toute l'équipe de l'IoNS Young Researchers Day, l'équipe du MSL-IN et ceux du groupe NOCIONS.

En outre, j'aimerais remercier chaleureusement mes amis qui ont contribué de près ou de loin à la réussite de cette thèse par leur présence et leur soutien. Même si vous pensez encore que je fais des robots pour manipuler des objets durant des vols paraboliques, je ne désespère pas de réussir un jour à vous faire comprendre la vraie nature de mes recherches. Merci à Nico (les deux), Mary, Léna, Thibaud, Carole, Pyg, Steph, Mika, Quentin, Johan, Dona, Nathalie, Hubert, Nayla, Astrid, Vincent, Aimeric, Max, Valéry, Hugo et tous les autres.

Un merci tout particulier à mes parents et ma sœur, qui ont toujours cru en moi et m'ont encouragé tout au long de ces (longues) études. Merci d'avoir toujours été là pour moi et pour m'avoir transmis ce que vous avez de meilleur.

Enfin, Céline, je te remercie du fond du cœur pour ta présence quotidienne à mes côtés, pour avoir supporté mes week-ends au bureau, pour m'avoir soutenu durant les moments de doute et pour avoir partagé mes joies. Notre histoire a commencé en même temps que cette thèse, mais elle se prolongera bien au-delà.

Bruxelles Allan Barrea
Novembre 2017

Abstract

Touch allows us to perceive the physical properties of the surrounding world. The numerous tactile afferents innervating the hand faithfully capture the complex mechanical interactions between the fingertips and the environment. Despite the critical importance of tactile information in a variety of tasks, the way the brain acquires and uses this information is still unclear.

This thesis explores tactile interactions from a biomechanical point of view. First, we present a new method to quickly measure friction at the fingertip-object contact while capturing its dependence on the normal contact force. Due to the compliant nature of the fingertips, localized slips occur at the fingertip contact under tangential loading. We examine how this *partial slip* phenomenon is related to the subjective perception of fingertip slip. We show that subjects can anticipate full slip and propose a new slip detection mechanism. To test this mechanism during manipulation, we develop the ActiveTouch manipulandum, which can image the fingertip contact and record fingertip interaction forces. Preliminary experiments confirm the presence of partial slips during manipulation. We suggest that these slips may help the brain to acquire information on the friction at the fingertip contact and on the dynamics of the manipulated object. Finally, we investigate how tactile afferent responses recorded *in vivo* are related to skin strain patterns measured within the fingertip contact.

This work contributes to the fundamental understanding of the biomechanical behavior of fingertips contacting objects in active and passive conditions. This thesis provides useful information for the design of rich tactile displays, bio-inspired tactile sensors, somatosensory neuro-prostheses, and haptic-enabled teleoperation systems.

Contents

CHAPTER 1

Introduction and background

"To succeed in research you need to know the field and to know yourself."

Vincent Hayward (IEEE World Haptics Conference 2017)

The sense of touch endows us with the capacity to perceive a rich variety of physical properties of the surrounding world. This capacity arises from the complex structure and mechanical properties of the fingertips. The interactions between the fingertips, acting as probes, and the environment are faithfully captured and sent to the brain by the numerous tactile afferent fibers innervating the hand. Using this information, the brain is able to manipulate objects with high dexterity. This chapter seeks to provide context to the work described in this thesis by reviewing the current knowledge in the following topics. First, we present the structure of the fingertip and explain how its mechanical properties naturally arise from its anatomy. Second, the tactile sensory system is described from the afferent fibers innervating the hand up to the brain. Third, we review evidence showing that the central nervous system critically relies on tactile information to manipulate objects skillfully. Finally, the last section of this chapter presents the research questions addressed in this thesis.

1.1. Structure and mechanical properties of the fingertip

1.1.1. Finger anatomy and functions

Bones and joints

Each fingertip is composed of three segments, except for the thumb, which has two. Each segment is supported by one bone called a phalanx. Phalanges are articulated together with highly flexible joints. This arrangement confers a great strength and mobility to the hand, allowing many configurations during manipulation.

Subcutaneous tissue

Bones are surrounded by subcutaneous tissue composed of collagen fibers and lobules of fat (Fig. 1.1). A network of collagen fibers radiating out from beneath the skin ensures that the finger pad is firmly attached of the distal phalanx (Hauck et al., 2004). The subcutaneous tissue contains a dense network of blood vessels and nerves, which supply the skin with blood irrigation and sensory innervation.

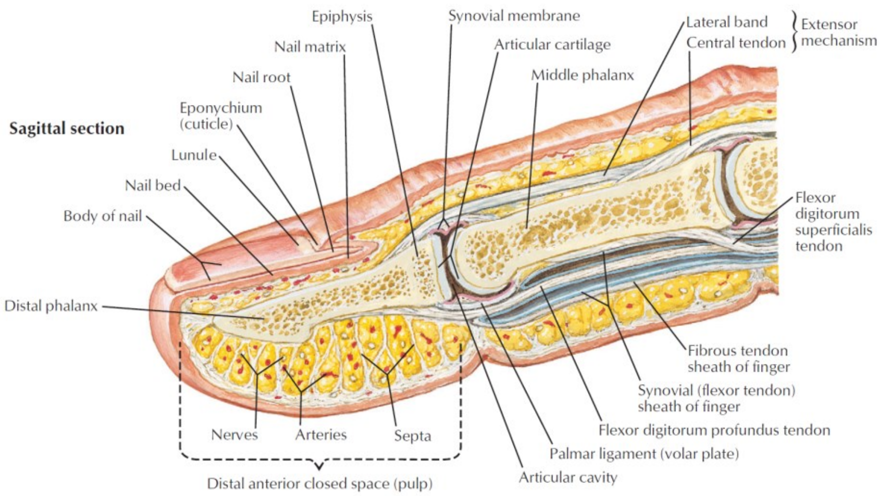

Fig. 1.1. Fingertip anatomy. The fingertip is supported by phalangeal bones articulated together by flexible joints. The subcutaneous tissue is composed of lobules of fat and collagen fibers anchoring the finger tissues to the bone. It contains a dense network of vessels and nerves providing the skin with blood irrigation and sensory innervation. Glabrous skin constitutes the protective envelope of the finger as well as a highly sensitive sensory organ. Finally, the fingertip terminates with the nail, which is anchored deeply in the skin. Adapted from Netter (2014).

Muscles

The hand contains two types of muscles: intrinsic muscles, both ends of which lie within the hand, and extrinsic muscles, which take their origin from the bones in the arm and forearm. As they approach the wrist, the bodies of extrinsic muscles are replaced by tendons that terminate in the phalangeal bones. Both types of muscles are involved in manipulation (Jones and Lederman, 2006).

Skin

The skin covering the hand acts both as a protective envelope and as a sensory organ. More precisely, it is involved in the following functions (Peckham et al., 2017):

- **Protection:** the skin protects the body against UV light, mechanical, thermal and chemical stresses, dehydration and invasion by microorganisms.
- **Sensation:** skin has receptors that sense vibrations, pressure, pain, and temperature. The human hand is innervated by more than 17.000 tactile afferent nerves encoding mechanical stimuli (Vallbo and Johansson, 1984), whose response properties and functions will be detailed later.
- **Thermoregulation:** various elements of the skin tissue are involved in regulating the temperature of the body, like sweat glands, hair, and adipose tissue.
- **Metabolic functions:** subcutaneous adipose tissue is involved in the production of vitamin D and triglycerides.

Two types of skin are found on the human body. The largest part of the body is covered with hairy skin. However, areas where there is a lot of abrasion, i.e. fingertips, palms and soles of the feet, are covered with the so-called glabrous (hairless) skin, which is thicker than the hairy skin. The glabrous skin on the volar surface of the hand is relatively rigid, but capable of bending along the flexure lines of the hand when objects are grasped. These folds enhance the security of the grasp and demarcate the areas of the hand where the skin is mobile as compared to the adjacent areas that are tightly bound to the underlying tissue and bones. In contrast, the hairy skin on the dorsal side of the hand is thin, soft and pliable (Jones and Lederman, 2006; Peckham et al., 2017).

Structure of the human glabrous skin[1]

There are three main layers in the skin: the epidermis, the dermis and the hypodermis (subcutaneous tissue) as illustrated in Fig. 1.9 later in the text. The epidermis is a thin membrane that forms the outer part of the skin and is directly in contact with the external environment. It is important for the protective function of the skin. The basal layers of the epidermis are folded to form dermal papillae (“pegs”). The epidermis is a keratinized, stratified, squamous epithelium, which means that it is composed of densely packed layers of dead keratinized cells that are continuously shed, and replaced with new cells. The glabrous skin epidermis is further divided into 5 sublayers. Cell divide in the basal layer, and move up to the layers above, changing their appearance as they move from one layer to the next. It takes around 2–4 weeks for this to happen. This continuous replacement of cells in the epidermal layer of the skin ensures that damaged cells exposed to the environment are continuously replaced by new ones. The epidermis of the glabrous skin is not smooth but instead folds into epidermal ridges and valleys forming characteristic patterns at the surface of the skin and responsible for fingerprints (Fig. 1.2). The periodicity of the ridges is approximately 400µm and sweat pores are found regularly along the ridges with a spacing of approximately 200–400µm.

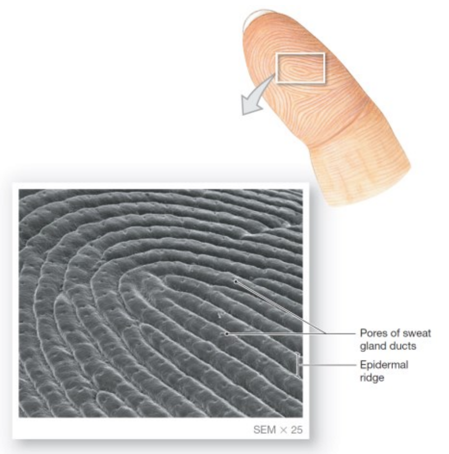

Fig. 1.2. Epidermal ridges of the glabrous skin responsible for fingerprints. Sweat pores are found regularly at the top of the ridges. They are the termination of the sweat ducts from eccrine sweat glands. Adapted from Martini et al. (2012).

[1] The material from this section is adapted from Peckham et al. (2017) unless otherwise stated.

The outermost layer of the epidermis is called the stratum corneum ("horny layer"). This layer is only composed of dead flattened cells ("squames") filled with keratin. It plays an important role in the frictional interactions between fingertips and objects. The stratum corneum is particularly thick in the volar side of the fingertips and is thicker in men than in women. It is thickest at the thumbs (around 400µm for men and 300µm for women), which are often in contact with objects. This thickness decreases linearly towards the little finger where it reaches approximately 300µm for men and 200µm for women (Fruhstorfer et al., 2000). In comparison, the thickness of the stratum corneum in the volar side of the forearm falls down to around 20µm, which is an order of magnitude smaller (Egawa et al., 2007). Thus, parts of the skin that are more in contact with objects exhibit a thicker stratum corneum than parts that are less in contact with objects are therefore less subject to abrasion. Besides, the water content varies dramatically across the thickness of the stratum corneum, dropping from approximately 70% at the inner stratum corneum to only 30% at the skin surface (Bielfeldt et al., 2009). In addition, moisture content of the stratum corneum is highly variable across individuals and influenced by many factors (Pires et al., 2016). Variations in the moisture content of the stratum corneum has dramatic impact on its mechanical properties and thus on the friction between fingertip and objects, as will be developed later.

Below the epidermis lies the dermis, a thicker inner portion of the skin involved in sensation, protection and thermoregulation. This is a tough and hydrated layer with a high water absorption and retention capacity. Water accounts for 60% of its weight. Beside water, the dermis is composed of collagen fibers (80% of its dry weight) that give the skin its tensile strength, and elastin fibers (4% of its dry weight) that provide elasticity and resilience to the skin (Uitto, 2008). The dermis also contains nerves, blood vessels, and sweat glands. It extends up into the epidermis in structures called dermal papillae, which have two functions. First, they help adhesion between the dermal and epidermal layers. Second, they provide a large surface area to nourish the epidermal layer, which does not have its own blood supply and therefore relies solely on the blood supply from the dermis.

Finally, the innermost layer of the skin is the hypodermis, which lies below the dermis. This layer mainly contains adipose tissue, which has a metabolic function: it is responsible for the production of vitamin D and triglycerides.

Sweat glands

Three major types of sweat glands are found in the skin: the sebaceous glands, the apocrine sweat glands, and the eccrine sweat glands. The sebaceous glands secrete an oily substance called sebum to lubricate the skin and help keep it waterproof. They are associated with hair follicles and are therefore not found in the glabrous skin. The apocrine sweat glands are present in the axillae (armpit), breast, perineal, and genital regions. They start secreting at puberty. The decomposition of their secretion by skin bacteria produces an acrid odor. They are most active in times of stress and sexual excitement. They open and secrete into the hair canal. Therefore, they are also not found in glabrous skin (Peckham et al., 2017; Wilke et al., 2007).

The third type of glands, the eccrine sweat glands, constitutes the majority of the sweat glands of the human body. They populate the entire skin but their density is highest in the glabrous skin of the volar side of the hands, reaching 600 glands per cm^2. The morphology of eccrine sweat glands is illustrated in Fig. 1.9 later in the text. They are formed of a tangled secretory portion, located deep in the dermis or in the superficial layers of the hypodermis, followed by an excretory duct that ascends to the superficial layers of the skin. The excretory duct penetrates an interpapillary peg of the epidermis, coils into the epidermis and then reaches the surface of the skin at the top of an epidermal ridge, forming a sweat pore (Fig. 1.2). Eccrine glands secrete a watery fluid ("sweat") that contains water, sodium chloride, potassium, urea ammonia and lactic acid (Peckham et al., 2017; Wilke et al., 2007). They are stimulated by sympathetic innervation as a result of fluctuations in body temperature. Secretion can also be induced by emotions such as anxiety, fear, stress and pain. They play an active role in thermoregulation by cooling the skin thanks to evaporation of the water contained in the secreted sweat (Gartner and Hiatt, 2015). They have also been shown to regulate skin moisture to maximize fingertip friction during object manipulation (André et al., 2010).

Finger nails

Nails can be used as tools, weapons, or for body care (Finlay, 1988). These functions are made possible by the combination of their hardness and flexibility. Nails consist of a strong plate of hard keratin that grows out from a nail bed. This constant growth ensures that nail portions damaged due to their interaction with the environment are replaced by new ones, similarly to what is observed with the human skin (Peckham et al., 2017). Nails must not be too hard otherwise they would become brittle. Moisture significantly influences the hardness of the nail: nails with a higher moisture content are more flexible and drier nails are more brittle (Farran et al., 2008). Previous investigations showed that the fingernails are optimally hard and flexible at ambient moisture levels (Farran et al., 2009). Finally, nails are involved in mechanosensation, with their tactile discrimination thresholds being comparable to those of the finger pad for dynamic stimuli and only slightly worse for static stimuli (Seah et al., 2013).

1.1.2. Intrinsic mechanical properties of the finger pad

The anatomy of the finger pad gives rise to complex mechanical properties that are described in this section.

Finger pad deformation

During tactile interactions, finger pad experiences large deformations even at small loads. An indentation depth of 1mm is observed for a flat indenter pressed with a normal force of 1N (Pawluk and Howe, 1999a). In addition, the finger pad exhibits a strongly non-linear force-displacement relationship with hysteresis (Serina et al., 1997). The non-linear stiffening of the finger pad observed for large deformations is due to the nature of the collagen fiber networks in the fingertip skin. The collagen fibers themselves are very stiff (Wenger et al., 2007) but arranged in a randomly coiled fashion so that they do not carry stresses at rest. When loaded, fibers become oriented and straightened out in the direction of the load and start carrying stresses. As more and more of these fibers are loaded, the effective stiffness of the skin increases (Daly, 1982; Fratzl et al., 1998).

Fingertip skin itself is not a homogeneous medium since the epidermis folds to form fingerprint ridges. The effective Young's modulus of the skin along and across the ridges is markedly different and skin is on average three times stiffer along the ridges than across them. This allows the skin to undergo large deformations perpendicularly to the direction of the ridges while preserving its strength along the ridges. As a result, fingertip skin can sustain a local relative deformation of 100% in stretching or in shearing without damage (Wang and Hayward, 2007). Besides, fingerprints have been shown to shape fingertip skin deformation, with fingerprints aligning perpendicularly to the tangential loading direction (Delhaye et al., 2016).

Finally, the mechanical properties of the stratum corneum are dramatically affected by its moisture content. In a dry state, the stratum corneum is brittle; when hydrated it becomes plastic and highly compliant. The elastic modulus of the stratum corneum has been shown to vary by two orders of magnitude over the range 40%-100% relative humidity (Adams et al., 2007; Lévêque and Rasseneur, 1988). The plasticization of the stratum corneum with moisture also dramatically affects its frictional properties as will be developed in the next section (Pasumarty et al., 2011).

Visco-elastic properties

During dynamic loading, the finger pad exhibits a visco-elastic behavior. Its mechanical properties are characterized by elasticity for stimulation frequencies ranging from DC to 100Hz and by viscosity above this frequency (Wiertlewski and Hayward, 2012). This visco-elastic response of the finger pad has been measured for normal (Jindrich et al., 2003; Pawluk and Howe, 1999a; Serina et al., 1997) as well as lateral loadings (Pataky et al., 2005). During unloading, the finger pad displays a non-linear behavior with marked hysteresis and an exponentially decaying relaxation with a time constant of about 10s (Pataky et al., 2005; Pawluk and Howe, 1999a; Serina et al., 1997). Fingertip skin is also locally visco-elastic during loading with a large amount of hysteretic loss upon unloading (Wang and Hayward, 2007).

Vibration propagation and tuning

Vibrations generated at the fingertips during tactile exploration travel throughout the hand up to the forearm without losing their information content. They spread through the tissues via different mechanisms including bone and tendon conduction and surface waves in the skin. The skin has been proven to act as a linear medium for wave propagation, therefore allowing for the application of the principle of superposition when studying vibration propagation (Fradet et al., 2017). These vibrations allow the tactile system to capture mechanical events generated at a distance from the transduction sites, as will be exposed later (Delhaye et al., 2012; Manfredi et al., 2012; Shao et al., 2016).

Besides, fingerprints also play a role in the transmission and tuning of vibrations generated during texture exploration. Indeed, they have been shown to enhance those vibrations in a frequency range corresponding to the peak sensitivity of tactile afferent fibers involved in the perception of fine textures (Manfredi et al., 2014; Prevost et al., 2009; Scheibert et al., 2009).

1.1.3. Finger pad tribology

After looking at the intrinsic mechanical properties of the finger pad, this section focuses on the mechanical behavior of the finger pad in contact with a countersurface. The tribology[2] of the human skin is inherently complex due to the layered nature of the skin, its visco-elastic properties and its sensitivity to humidity (Persson et al., 2013).

Contact area

The surface of the fingertip skin is discontinuous at several length scales. The epidermal ridges form the gross, visible asperities of the skin. However, ridges themselves present irregular asperities (Dzidek et al., 2017b). The roughness of the fingertip skin can therefore be modeled as a random height profile following a normal distribution with self-similar asperities at different length scales (Persson, 2007; Persson et al., 2013; Wiertlewski et al., 2016). Because of this particular roughness profile, the contact area formed by a fingertip pressed against a flat, smooth and rigid surface can also be considered at different length scales (Dzidek et al., 2016). The apparent or gross contact area (A_{gross}) is defined as the contour of all asperities in contact with the countersurface and has an elliptical shape. However, not all parts of A_{gross} are actually in contact with the surface. The ridge contact area (A_{ridge}) only considers the ridges in contact with the surface and excludes the interstitial spaces between them. A_{ridge} is therefore smaller than A_{gross} and closer to the real contact area A_{real}, formed by the asperities actually contacting the countersurface. Several studies showed that the real contact area varies with the normal load W following a power law of the form given in equation (1.1), where n is the *load index* and k is a scaling factor (Adams et al., 2007; Dzidek et al., 2017b; van Kuilenburg et al., 2013). The Hertzian theory of contact predicts that n has a value of 2/3 for a large elastic sphere normally loaded against a flat, homogeneous, and elastic surface. Empirical measurements found values of n ranging from 0.15 to 1.33 (van Kuilenburg et al., 2013).

$$A_{real} = kW^n \tag{1.1}$$

The Hertzian theory of contact provides only a simplified view of the mechanical interactions between two bodies in contact. The JKR model of adhesive contact extends Hertz's model by taking into account the presence of adhesive forces between the two bodies in contact (Johnson et al., 1971). Another model of adhesive contact extending Hertz's theory is the DMT model (Derjaguin et al., 1975; Muller et al., 1983; Pashley, 1984). Recently,

---

[2] Tribology is the science that studies the friction, lubrication, and wear of interacting surfaces in relative motion.

these models have in turn been extended to the case of the adhesive contact of viscoelastic spheres (Haiat et al., 2003; Hui et al., 1998). In future experiments, these more accurate contact models should be applied to describe the mechanical behavior of the finger pad in contact with a countersurface, taking into account adhesive forces at the contact and the visco-elastic properties of the finger pad. The interested reader will find more details about the development of the models of adhesive elastic contact in a recent review (Barthel, 2008).

When the normal loading increases, the apparent contact area A_{gross} rapidly reaches an ultimate value. However, the contact made by the ridges A_{ridge} is initially formed from unconnected micro-contacts or junctions, whose number, size and connectivity increase for several seconds. The real contact area, which drives the friction at the interface, thus evolves smoothly for several seconds (Dzidek et al., 2016). This is due to the occlusion phenomenon arising when the finger pad is pressed against a flat, non-porous surface like smooth glass. Because the contact is occluded, moisture excreted by the sweat pores accumulates at the interface between the fingertip and the surface (Pasumarty et al., 2011). The accumulated moisture plasticizes the stratum corneum, making it softer and allowing it to better conform to the countersurface. This causes the increase of the real contact area with a relatively large time constant in the order of 20s (Adams et al., 2013; Dzidek et al., 2017a, 2014; Persson et al., 2013). In contrast, when pressed against a rough surface, the contact is not occluded and moisture does not accumulate, resulting in a much lower plasticization of the stratum corneum and therefore a lower increase of the real contact area (Dzidek et al., 2014).

The apparent contact area A_{gross} has a value of around 100mm² on average for a normal load of 1N. It increases with increasing load as suggested by equation (1.1) and saturates at values reaching 300mm² above 10N due to non-linear stiffening of the finger pad (André et al., 2011). Under tangential loading, the apparent contact area systematically decreases during incipient slip before stabilizing after full slip. This reduction of the contact area is a consequence of fingertip rolling, i.e. tissues losing contact with the countersurface during tangential traction. This behavior has been attributed to the stiffening of the finger pad with the tangential load, resulting in an increased effective Young's modulus (Delhaye et al., 2014). The evolution of the contact area depends on numerous factors including morphological properties of the fingertips such as intrinsic stiffness and curvature of the finger pulp. Therefore, it is highly variable between subjects. The angle formed between the fingertip and the surface has also been shown to affect the contact area by modifying the apparent stiffness of the finger pulp (Serina et al., 1997; Warman and Ennos, 2009).

The pressure distribution within the contact is not homogenous, as illustrated in Fig. 1.3. At low normal forces, the pressure is characterized by round profiles, as qualitatively suggested by the Hertzian theory of contact. However, at higher normal loads the pressure distribution becomes asymmetric and conical (Fig. 1.3A) (Derler et al., 2013). The point of maximum pressure is shifted towards the distal part of the contact with increasing normal loading, due to the bone structure underlying the soft tissues of the finger pad (Fig. 1.3B) (Pawluk and Howe, 1999b).

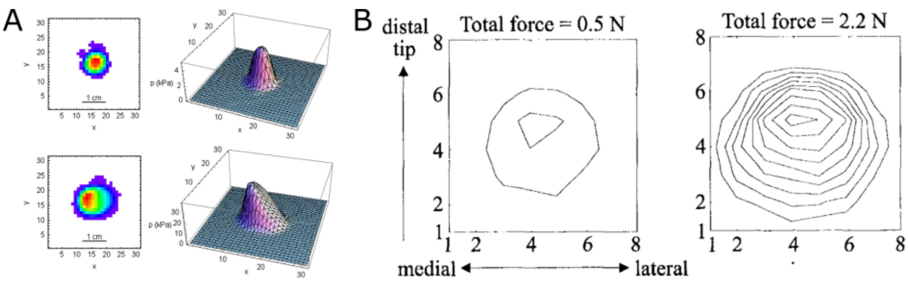

Fig. 1.3. Normal pressure distribution within the fingertip contact. (A) Normal pressure distribution for the index finger pad pressed against a flat surface with a normal force of 0.25N (top row) and 3.2N (bottom row). Reproduced from (Derler et al., 2013). **(B)** Contour plots of the normal pressure distribution for a flat indenter pressed against the index finger pad with a normal force of 0.5N (left) and 2.2N (right). Contours indicate increasing pressure levels of 4kPa. Reproduced from Pawluk and Howe (1999b).

The traction distribution is influenced by the friction of the contact interface. Contact with a more slippery surface results in a greater amount of localized slipping and creeping in the contact area than with a surface exhibiting a higher friction. Therefore, the local traction in the contact is lower and thus tangential stress in the finger pad is lower (Johansson and Flanagan, 2009).

The variation of the contact area is faithfully captured by the nervous system. Indeed, the change of the contact area acts as a proprioceptive cue (Moscatelli et al., 2016) and helps subjects discriminate surface softness

(Bicchi et al., 2000). In addition, the variation of the contact area alone can create the illusion of haptic shape (Dostmohamed and Hayward, 2005).

Friction

Fingertip friction plays a critical role in tactile exploration and object manipulation. Owing to its visco-elastic properties, friction of the skin does not follow the classical Amontons-Coulomb's law of friction stating that the friction force is (1) directly proportional to the normal load and (2) independent of the area of contact between the surfaces (Comaish and Bottoms, 1971). Instead, friction of the fingertip skin is affected by normal force, contact area, hydration, surface roughness, motion direction and sliding speed (Tomlinson et al., 2007).

Static coefficient of friction and its dependence on normal force

The friction force F of viscoelastic materials like the skin is explained by the sum of an adhesive interfacial term F_{int} and a deformation term F_{def} due to hysteresis (equation (1.2)). Adhesion is due to local bonds occurring at the asperities of the skin in contact with the countersurface, and F_{int} is the force required to break these adhesive bonds. The deformation term F_{def} arises from the incomplete recovery of the energy dissipated by sub-surface visco-elastic deformations and visco-elastic stretching of the skin (Adams et al., 2007; Tomlinson et al., 2007).

$$F = F_{int} + F_{def} \approx F_{int} \tag{1.2}$$

Because of the soft and highly deformable nature of the finger pulp, the fingertip rolls against the countersurface when loaded tangentially. As a result, the deformation term is small and may be ignored so that only the interfacial term is considered in the friction force, as expressed in equation (1.2) (Adams et al., 2007). The friction force of rubbery materials has been shown to be proportional to the real contact area through the interfacial shear strength τ (Schallamach, 1952):

$$F_{int} = \tau A_{real} \tag{1.3}$$

The static coefficient of friction μ_{static} is defined as the ratio of the friction force to the normal force. The friction force is the force acting tangentially to the surface required to break all adhesive junctions and thus cause relative motion between the two bodies in contact. Therefore, μ_{static} corresponds to the ratio of the tangential to the normal force at slip onset. Combining expressions (1.2) and (1.3) with the definition of μ_{static} yields the following model:

$$\mu_{static} = \frac{F}{W} \approx \frac{F_{int}}{W} = \frac{\tau A_{real}}{W} \quad (1.4)$$

For rough contacts, A_{real} is approximatively proportional to the normal load W, hence the friction coefficient becomes constant and independent of the normal load, as predicted by the Amontons-Coulomb's law of friction. In the Hertzian theory of contact however, A_{real} is proportional to $W^{2/3}$ for a contact between a sphere and a surface and to $W^{1/2}$ for a contact between a cylinder and a surface. In this case, the model of μ_{static} is given by equation (1.5), where n is the load index and k a scaling factor (Dzidek et al., 2016).

$$\mu_{static} = kW^{n-1} \quad (1.5)$$

This model highlights the dependence of μ_{static} on the normal force W, confirming that skin friction does not follow the Amontons-Coulomb's law of friction. Empirical measurements made by several previous studies are well explained by this model, with values of the load index ranging from 0.5 to 1, i.e. from a purely Hertzian contact to a rough contact (van Kuilenburg et al., 2013).

The parameters k and n vary with the load range being considered and do not reflect some material properties of the two bodies in contact (Adams et al., 2007). For large normal forces, the load index is close to 1 and the friction is Coulombic. However, for low values of normal force, i.e. below 5N, the load index becomes smaller than 1 and μ_{static} increases dramatically with decreasing normal force (André et al., 2009; van Kuilenburg et al., 2013).

Impact of moisture on fingertip friction

Because of the impact of moisture on the real contact area, which drives the friction as exposed above, moisture also dramatically affects the friction at the fingertip contact. It has been observed that in the case of smooth non-porous surfaces, the friction force increased progressively with occlusion time until reaching a constant value. This resulted in a temporal evolution of the parameters k and n in equation (1.5) following a first-order kinetic relationship with a large time constant of approximately 20s (Dzidek et al., 2014).

Previous studies quantified the effect of hydration on fingertip friction, showing that friction was dependent on moisture following a bell-shaped relationship. When water is added between the fingertip and the countersurface, friction starts increasing up to a given point. This increase is due to capillary adhesion between the ridges of the skin and the contacting surface. Past this points, the addition of more water reduces the friction because water begins to form a layer of separation between the fingertip and the surface (Pasumarty et al., 2011; Tomlinson et al., 2007). Besides, a similar relationship is observed between friction and the moisture content of the stratum corneum, with an intermediate level of skin moisture maximizing the coefficient of friction, which decreases for damper or dryer skin (André et al., 2009). The increase of friction with skin moisture is due to the plasticization, i.e. softening, of the stratum corneum, which increases the real contact area and thus the number of adhesive bonds between the fingertip and the surface (Pailler-Mattei et al., 2007; Tomlinson et al., 2011). This effect is larger for smooth and non-porous surfaces like glass than for rough surfaces because of the larger accumulation of moisture in an occluded contact (Adams et al., 2013).

Besides, André et al. found that an excess of moisture reduced the tendency of the contact to slip, regardless of the variations of the coefficient of friction. For a given contact state, they showed that a 10% increase in the tangential loading can lead to full slip when skin hydration is low, whereas a 40% increase is needed with a well-hydrated skin (André et al., 2011). They also showed that fingertip skin moisture is modulated during object manipulation so as to maximize the coefficient of friction. They hypothesized that moisture was increased via sweating and reduced via passive reabsorption in the skin (André et al., 2010).

Dynamic coefficient of friction and the effect of sliding speed

Steady-state sliding is often encountered during tactile exploration, with a sliding velocity comprised between 1cm/s and 20cm/s (Guest et al., 2012; Libouton et al., 2010). To quantify friction in these conditions, the dynamic coefficient of friction is defined as the ratio of the tangential to the normal force under steady-state sliding of the fingertip against the countersurface. This dynamic coefficient of friction is affected by sliding speed in a complex manner. It is maximum at intermediate velocities within the range relevant to tactile exploration. In addition, the dynamic coefficient of friction varies also with the hydration level of the contact (Adams et al., 2013; Pasumarty et al., 2011).

Finally, in some cases no static coefficient of friction can be defined because the tangential force increases smoothly and monotonically until reaching a plateau. In these cases, the dynamic coefficient of friction is the only way to measure friction in a reproducible manner across trials. Appendix

A presents empirical measurements of the dynamic coefficient of friction on various materials, including some exhibiting this behavior.

Partial slip

The finger pad is not rigid and undergoes large local deformations when loaded tangentially against a surface (Delhaye et al., 2016). Contact mechanics and in vivo experiments highlighted the existence of partial slip, i.e. localized slippage of the contact before full slip, under tangential loading of the fingertip. A simplified mechanical model of partial slip is first derived, and then experimental evidence of this phenomenon is briefly presented.

First, let us assume that the fingertip is a large homogeneous elastic sphere pressed normally against a flat, rigid countersurface, forming a circular contact. Under these assumptions, Hertz found that the pressure distribution at the interface between the sphere and the surface had a profile given by equation (1.6), where p is the pressure, r is the distance from the center of the contact, a the radius of the contact, and p_0 a constant factor (Johnson, 1985). This pressure profile is illustrated in Fig. 1.4.

$$p(r) = p_0\left(1-\frac{r^2}{a^2}\right)^{\frac{1}{2}} \tag{1.6}$$

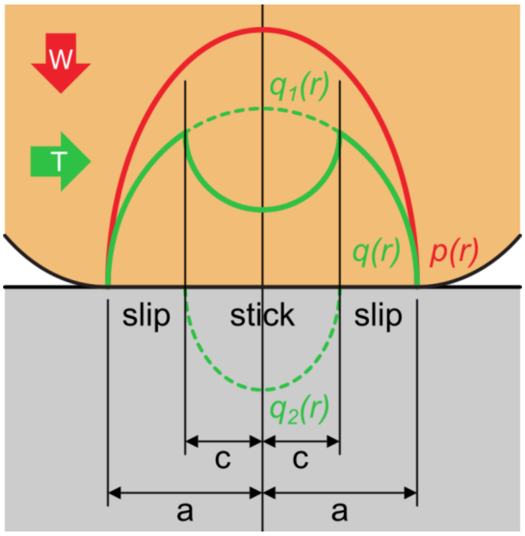

Fig. 1.4. Schematic illustration of force profiles during partial slip. Pressure (p, red) and traction (q, green) profiles under normal (W, red) and tangential (T, green) loading of an elastic sphere in contact with a rigid surface. The radii of the contact and no-slip areas are denoted by a and c, respectively. Adapted from (Johnson, 1985) with material from Tada et al. (2006).

When the elastic sphere experiences tangential loading, the periphery of the contact, where the pressure is lower, starts slipping while the center of the contact sticks to the surface, forming a no-slip area. As tangential loading increases, the circular no-slip zone at the center of the contact reduces until the whole contact is slipping. A simple expression of the traction profile that is a close approximation to the actual traction profile at the contact was found by Cattaneo and Mindlin. It is expressed as the superposition of two terms derived from the Hertzian pressure distribution: (1) a traction profile $q_1(r)$ in the whole contact area and (2) a similar traction profile $q_2(r)$ in the no-slip area. This traction profile is given by equation (1.7) and it is illustrated in Fig. 1.4. In this equation, q is the traction, c is the radius of the circular no-slip area, and μ is the coefficient of friction. It is assumed here that the Amontons-Coulomb's law of friction is valid locally within the contact. Therefore, a given point of coordinate r_0 sticks to the surface until $q(r_0) > \mu p(r_0)$, at which moment it starts slipping.

$$q(r) = q_1(r) + q_2(r) \tag{1.7a}$$

$$q_1(r) = \mu p_0 \left(1 - \frac{r^2}{a^2}\right)^{\frac{1}{2}} \quad (0 < r < a) \tag{1.7b}$$

$$q_2(r) = -\frac{c}{a}\mu p_0 \left(1 - \frac{r^2}{c^2}\right)^{\frac{1}{2}} \quad (0 < r < c) \tag{1.7c}$$

This traction profile can be integrated over the whole contact area to find the radius of the no-slip area as a function of the tangential (T) and normal (W) forces, as developed in equation (1.8) (Johnson, 1985).

$$T = \iint q(r)\, dr\, r\, d\theta \tag{1.8a}$$

$$T = \int_0^a 2\pi r\, q_1(r)\, dr + \int_0^c 2\pi r\, q_2(r)\, dr \tag{1.8b}$$

$$T = \mu W \left(1 - \left(\frac{c}{a}\right)^3\right) \tag{1.8c}$$

$$\Rightarrow \frac{c}{a} = \left(1 - \frac{T}{\mu W}\right)^{\frac{1}{3}} \tag{1.8d}$$

To easily quantify the amount of slippage within the contact, Tada et al. introduced the stick ratio (SR), which is defined as the ratio of the no-slip area to the whole contact area. Under the assumptions made above, SR is related to the normal (W) and tangential (T) forces according to equation (1.9) (Tada et al., 2006). Starting from a fully stuck contact (SR = 1) and keeping the normal force constant, this model predicts that the increase of the tangential force will make the no-slip area decrease monotonically until full slip (SR = 0), with slip propagating from the periphery of the contact towards its center like a bushfire.

$$SR = \frac{\pi c^2}{\pi a^2} = \left(1 - \frac{T}{\mu W}\right)^{\frac{2}{3}} \tag{1.9}$$

Of course, the finger pad is not a homogenous elastic sphere and the expressions derived above are not directly applicable to predict the mechanical behavior of an actual fingertip loaded tangentially against a rigid surface. However, partial slips have been observed in vivo with the same qualitative behavior as the theoretical model (André et al., 2011; Delhaye et al., 2014; Tada et al., 2006), which is illustrated in Fig. 1.5.

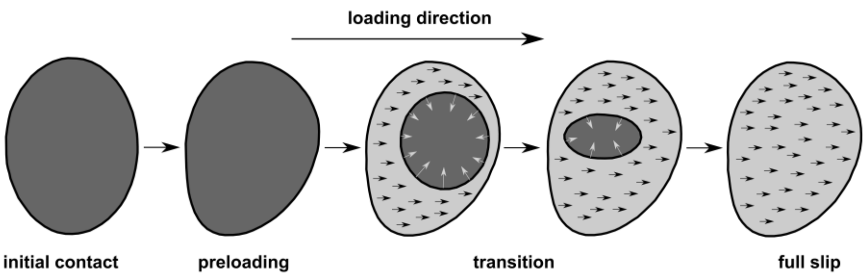

Fig. 1.5. Partial slip of fingertip contact under tangential loading. From left to right: initial stuck contact (dark grey), preloading, slip onset starting at the trailing edge, growth of the slip region (light grey) from the periphery to the center of the contact, and full slip. The stick ratio is defined as the ratio of the no-slip area (dark grey) to the whole contact area. Adapted from André et al. (2011).

1.1.4. Imaging of the fingertip contact

Several optical systems have been developed to image the surface of a fingertip in contact with a flat glass plate. These systems are based on the frustrated total internal reflection (FTIR) phenomenon. First, FTIR is briefly described. Then, different optical systems used to image the fingertip contact are reviewed.

FTIR is based on the evanescent wave phenomenon. When light is incident on the interface of two media, it is partly transmitted into the second medium and partly reflected back to the first. If the second medium is optically less dense than the first, i.e. has a lower index of refraction, and if the angle of incidence of the light beam exceeds a critical angle, total internal reflection occurs, i.e. the light beam is totally reflected back in the first medium and it does not propagate in the second medium. However, even in case of total reflection, the incoming light penetrates a little bit into the second medium because the electric and magnetic fields cannot be discontinuous at the interface. The amount of light entering in this way into the second medium falls off exponentially with penetration depth. This phenomenon is thus called the *evanescent wave* even though this is not a wave properly speaking, because it does not propagate. The penetration depth of this evanescent wave is of the order of magnitude of the wavelength of the light, i.e. a few hundred nanometers in the case of visible light. Now, if a third medium is placed at a small distance to the first medium, reducing the second medium to a thin film whose thickness is of the same order of magnitude as the light wavelength, then the incident light is transmitted to the third medium, thereby reducing the amount of light reflected into the first medium. This phenomenon is called frustrated total internal reflection (FTIR) (You et al., 2008; Zhu et al., 1986).

This principle allows imaging the asperities of a fingertip close to a flat, transparent glass plate up to a few hundred nanometers using visible light. In this configuration, glass plays the role of the first, optically dense medium, the thin air gap between the fingertip and the plate is the second medium and the fingertip is the third medium, disrupting ("frustrating") the reflection of the light when close enough to the plate. However, when asperities of the fingertip are more than a few hundred nanometers away from the plate, the reflection is not frustrated and all the light is reflected back in the glass.

A first imaging system taking advantage of FTIR is described in Fig. 1.6A. In this configuration, the glass plate is illuminated sideways and acts as a light trap. Asperities of the fingertip close to the glass up to a few hundred nanometers scatter the light out of the glass, which is captured by an imager. This system produces images with a dark background, i.e. where there is no contact and thus no scattered light, and a bright picture of the real fingertip contact area. Wiertlewski et al. showed that the brightness of the image is strongly correlated with the friction force and that FTIR can thus be used as a proxy to measure interaction forces at temporal and spatial scales out of reach to standard force sensors (Wiertlewski et al., 2016). This configuration has the advantage of being compact and it was integrated into a manipulandum to study incipient slip of the fingertip contact during object manipulation (Tada et al., 2000, 2002). However, it produces images with fuzzy contour of the contact.

In another configuration using a glass prism, the light reflected in the glass is imaged instead of the light scattered by the asperities close to the glass (Fig. 1.6B). This system produces images with a white background where the fingerprints in contact with the glass appear in black, with a sharp contour of the contact. Such system was used to measure skin strain during tactile exploration (Levesque and Hayward, 2003) and to study the effect of fingertip hydration on the frictional properties of the contact (André et al., 2011). Images acquired with this system require aspect-ratio correction because the camera axis is not perpendicular to the contact surface. In addition, the depth of field of the imager must be large to capture a clear image of the whole contact (Bochereau et al., 2017).

A variant of the prism-based configuration using normal, coaxial illumination with the help of a half-mirror was introduced by Tada et al. (Tada and Kanade, 2004). This system is illustrated in Fig. 1.6C. It offers the advantage of being more compact than the prism-based version and allows the glass medium to be easily moved and replaced while still producing a clear image of the real contact area with sharp contact edges. In addition, images do not require aspect-ratio correction because the camera axis is perpendicular to the contact surface. However, the image contrast is lower than with the prism-based system because of the lesser amount of light reflected back to the imager. This system has been used to image incipient slippage of the fingertip contact and to study the effect of normal force and stroking speed on the evolution of slip in the contact (Tada et al., 2006). Using a similar configuration, Delhaye et al. studied the evolution of the contact area, partial slip and surface strains in the contact under four tangential loading directions with different levels of normal force and tangential speed (Delhaye et al., 2014, 2016).

Each FTIR-based system has its strengths and weaknesses in terms of quality of images produced and compactness. A recent study combined several of these systems into a single experimental setup able to record and render the forces generated during tactile exploration while simultaneously imaging the fingertip contact. This system allows measuring the dynamics of the fingertip contact during exploration of a broad range of textured surfaces (Bochereau et al., 2017).

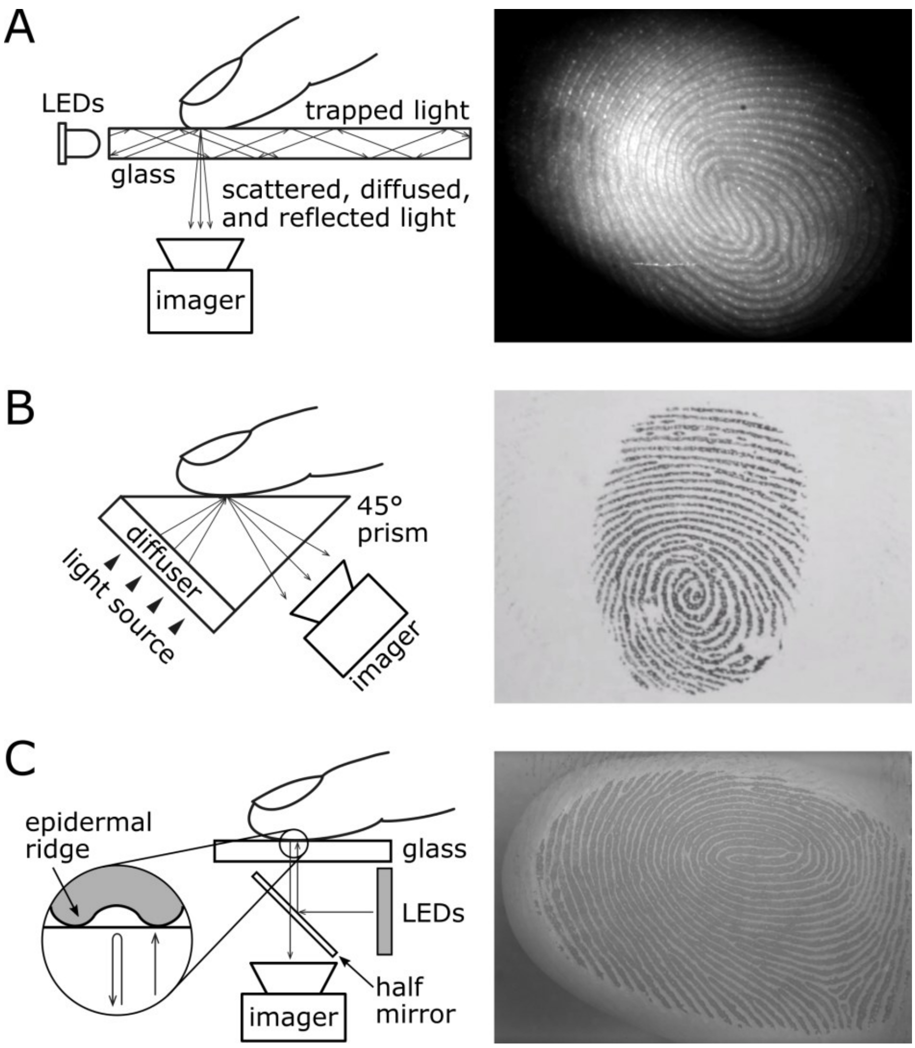

Fig. 1.6. Three optical configurations based on FTIR allowing imaging of the fingertip contact. (A) Imaging fingertip contact with side illumination of the glass plate. The resulting image combines light scattered at the points of contact, tissue-diffused light and reflected light. **(B)** Prism-based FTIR to image fingertip contact. Asperities of the fingertip surface close to the plate up to a few hundred nanometers disrupts reflection of the light and appears black on the image. **(C)** Optical configuration using coaxial light source and camera with the help of a half-mirror. The principle is the same as in panel B but with lower contrast. Adapted from Bochereau et al. (2017) and Tada and Kanade (2004).

Finally, FTIR is not the only optical effect that can be used to image the fingertip contact. Liu et al. demonstrated that optical coherence tomography (OCT) also allows local imaging of the fingertip contact (Liu et al., 2013). They used OCT to image sub-surface slices of the fingertip skin, with a depth of 2mm (Fig. 1.7). This technique was used to investigate the relationship between skin structure and its frictional properties (Liu et al., 2015). In addition, by combining several slices, local 3D imaging of the skin was possible but only for areas of a few square millimeters (Liu et al., 2017). OCT therefore offers an interesting view of the real contact area by imaging the sub-surface structure of the skin, but does not allow imaging of the whole contact area. Besides, the temporal resolution of OCT is of the order of a few hertz, i.e. far below the framerate of direct imaging techniques based on FTIR, which can reach one kilohertz (Bochereau et al., 2017).

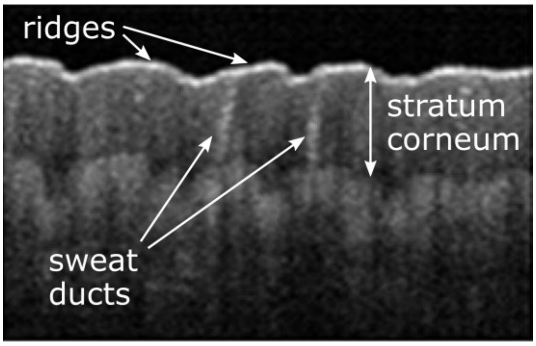

Fig. 1.7. Optical coherence tomography (OCT) image of the fingertip skin surface and sub-surface with a depth of 2mm. Fingertip ridges are visible along with sweat ducts and the stratum corneum. Slice dimensions are 4mm (width) by 2mm (depth). Adapted from Liu et al. (2013).

1.2. Response properties and functions of tactile afferent fibers

1.2.1. Overview

The glabrous skin is innervated with several types of tactile afferent fibers exhibiting markedly distinct response properties. Here we examine the so-called low-threshold afferent fibers (“tactile afferents”), mediating light touch. These neurons have myelinated fibers of type Aβ, characterized by high conduction velocities ranging between 16m/s to 100m/s (Abraira and Ginty, 2013). Tactile afferents are classified based on their response to different stimuli.

Two broad categories of afferents are defined based on the temporal dynamics of their response to static indentation: fast-adapting (FA) vs. slow-adapting (SA) fibers. The former have a phasic response, i.e. respond only to onset and offset of skin indentation, while the latter have a tonic response, i.e. maintain firing during sustained indentation of the skin. These two categories are further refined into the so-called type 1 fibers, which possess small receptive fields with distinct borders, and type 2 fibers, which exhibit larger receptive fields with diffuse borders. Four types of tactile afferents are thus present in the glabrous skin: FA1, SA1, FA2, and SA2. It has been estimated that approx. 17,000 tactile afferents innervate the human hand, in the following proportions: 43% FA1, 25% SA1, 13% FA2, and 19% SA2 (Johansson and Vallbo, 1983; Vallbo and Johansson, 1984).

Type 1 afferents innervate the superficial layers of the skin, with a particularly high density in the fingertips. They are sensitive to small deformations of the skin, with FA1 afferents encoding dynamic skin deformations of relatively high frequency and SA1 afferents being stimulated by continuous and lower-frequency indentation. FA1 afferents are highly sensitive to dynamic deformations in the 5–50Hz range while SA1 afferents respond primarily to static and low-frequency deformations below 5Hz. Beyond these peak sensitivity ranges, these two classes of afferents respond to a larger spectrum of stimulation frequency.

In contrast, type 2 afferents are found deeper in the skin and innervate the hand with a lower and roughly uniform density. FA2 afferents are extremely sensitive to vibrations ranging from 5Hz to about 1000Hz (LaMotte and Mountcastle, 1975; Mahns et al., 2006; Mountcastle et al., 1972; Talbot et al., 1968) with a peak sensitivity around 250–300Hz (Freeman and Johnson, 1982; Muniak et al., 2007; Talbot et al., 1968). SA2 afferents respond to skin stretch and present a low dynamic sensitivity (Johansson and Flanagan, 2009). These properties are summarized in Table 1.1.

When skin is stimulated, mechanical interactions elicit electrical signals in the nerves in a process called mechanotransduction. The molecular mechanisms behind mechanotransduction are still largely unknown. However, the concept of mechanically-gated ion channels in the membrane of the sensory neurons mediating mechanotransduction is generally accepted (Lumpkin and Caterina, 2007). In short, when a cell membrane is stretched due to the local deformations of the tissue, this activates stretch-sensitive ion channels in the membrane. The opening of the channels causes

Table 1.1. Properties of the tactile afferent fibers. Adapted from Abraira and Ginty (2013), Johansson and Flanagan (2009), Johnson (2002), and Vallbo and Johansson (1984).

	Small receptive field		Large receptive field	
Afferent type	FA1	SA1	FA2	SA2
Associated end-organ	Meissner corpuscle	Merkel corpuscle	Pacinian corpuscle	Ruffini corpuscle
Location of end-organ	Dermal papillae (close to skin surface)	Tip of epidermal sweat ridges	Dermis and deeper tissues	Dermis and nail border
Conduction velocity	26–91m/s	16–96m/s	30–90m/s	20–100m/s
Innervation density (finger pad)	140/cm²	70/cm²	20/cm²	10/cm²
Innervation density (palm)	25/cm²	10/cm²	10/cm²	20/cm²
Effective stimuli	Dynamic skin deformation	Static skin indentation	Vibration	Skin stretch
Receptive field area (measured with rapid 0.5mm indentation)	22mm²	9mm²	Entire finger or hand	60mm²
Spatial acuity	3mm	0.5mm	>10mm	>7mm
Response to sustained indentation	None (rapid adaptation)	Sustained (slow adaptation)	None (rapid adaptation)	Sustained (slow adaptation)
Frequency range of maximum sensitivity	5–50Hz	<5Hz	40–400Hz (peak around 250Hz)	0–?Hz
Stimulus features encoded	Transmit enhanced representations of local spatial discontinuities (e.g. edges and Braille-like dots).		Respond to distant events acting on hand-held objects.	Respond to remotely applied stretching of the skin.

an influx of cations and a local depolarization of the cell, triggering an action potential if the depolarization is strong enough. The varying sensitivity to pressure and desensitization rates of the different cation channels may shape the response properties of the various classes of afferents (Delmas et al., 2011).

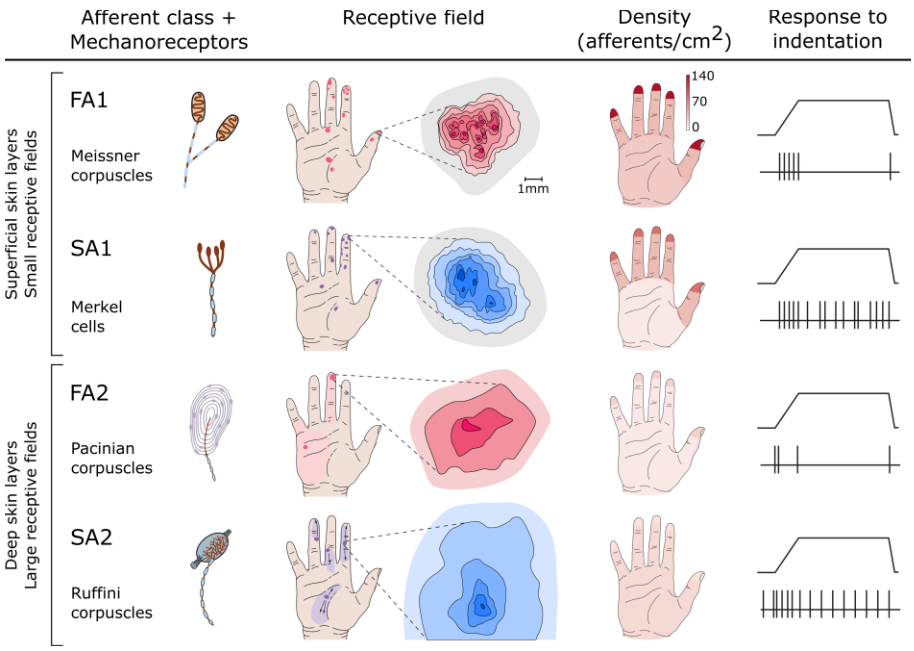

Fig. 1.8. Properties of tactile afferents innervating the human hands. Each fiber is associated with a specialized end-organ called a mechanoreceptor modulating the response of the fiber to external stimuli. The receptive fields of single afferents are represented. Receptive fields of FA1 and SA1 fibers are small oval-shaped spots will sharp borders. Those of FA2 and SA2 are large with diffuse borders because the associated mechanoreceptors are located deeper in the skin. FA1 and SA1 fibers innervate clusters of mechanoreceptors, giving rise to complex receptive fields with multiple hotspots. FA2 and SA2 innervate only one large receptor cell. Innervation density of the fibers is represented for the entire hand. A very high density of FA1 and SA1 units are found in the fingertips. Finally, the response of units to static indentation is presented with the upper part of the diagrams representing the indentation and the lower part the neural spike train elicited in the afferent in response to the stimulus. Adapted from Vallbo and Johansson (1984), with material from Gardner (2010) and Johansson and Flanagan (2009).

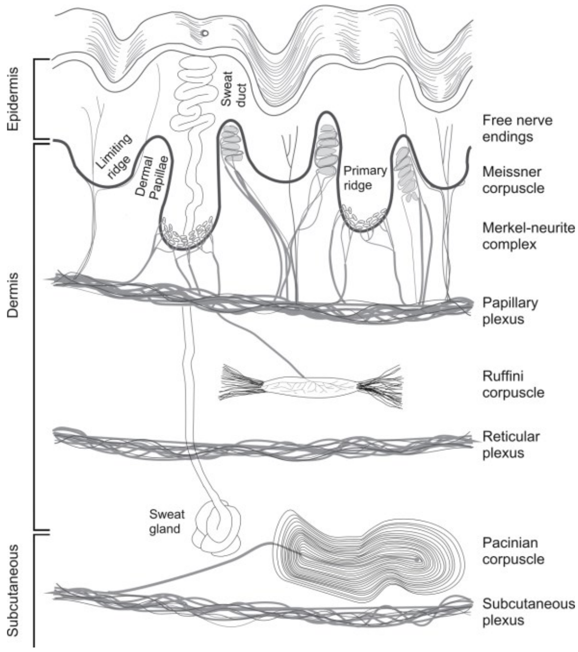

Fig. 1.9. Innervation of the human glabrous skin. Glabrous skin contains three layers: the epidermis, the dermis and the hypodermis (subcutaneous tissue). The thickness of the epidermis is fairly constant over the glabrous surface of the hand; the distance from the skin surface to the dermal papillae is typically 0.6mm, whereas the distance to the tips of the primary ridges, which contain the sweat ducts and coincide with prominent ridges ("fingerprints") on the finger surface, is typically 1mm. The dermis is 2mm to 3mm thick and contains connective tissue (predominantly collagen and elastin fibers), blood vessels, sweat glands and nerve plexuses. The hypodermis lies under the dermis, and mainly contains adipose tissue. The mechanoreceptors associated with the tactile afferent fibers are illustrated on the figure. The Meissner's corpuscles are located in the tips of the dermal papillae. Each corpuscle is innervated by several FA1 afferents and a given FA1 afferent branches in the skin to innervate several Meissner's corpuscles, giving rise to spatially complex and overlapping receptive fields. Merkel cells are specialized epidermal cells located in the tips of the primary epidermal ridges. A single SA1 afferent innervates many Merkel cells on several ridges, also giving rise to complex receptive fields. Pacinian corpuscles are located in the deeper parts of the dermis and in the subcutaneous tissues. A single FA2 axon innervates a single Pacinian corpuscle and, likewise, a single Pacinian corpuscle is innervated by a single FA2 axon. Ruffini corpuscles are supposed to be spindle-shaped receptors innervated by a single SA2 afferent and constituted of encapsulated strands of connective tissue and nerve endings. However, their existence in the glabrous skin is questioned and therefore much controversy remains as of the actual termination of the SA2 afferents. Adapted from Johnson (2002).

Tactile afferent fibers terminate in specialized end-organs called the mechanoreceptors. Together with the response properties of the fibers themselves, mechanoreceptors associated with the fibers help tune the afferent response to particular features of somatic stimulation. Fig. 1.8 present the mechanoreceptor associated with each afferent class and Fig. 1.9 illustrates their relative location in the skin. There is a common agreement as of which afferent terminates in which receptor, backed by numerous neurophysiological and histological studies (see (Abraira and Ginty, 2013; Iggo and Andres, 1982; Vallbo and Johansson, 1984) for reviews). However, the precise role played by mechanoreceptors in the mechanotransduction remains unclear for several afferent classes. In addition, considerable controversy remains regarding the termination of SA2 afferents, as exposed in a dedicated section below.

Tactile afferents of type 2 terminate in a single end-organ. However, afferents of type 1 branch in the skin and innervate a large number of mechanoreceptors, forming many transduction sites (Fig. 1.9). This gives rise to spatially complex and multi-hotspots receptive fields, as illustrated in Fig. 1.8. This complex receptive field structure endows first-order tactile neurons with the capacity to encode the orientation of edges pressed against the finger pad (Pruszynski and Johansson, 2014; Pruszynski et al., 2017). In addition, complex receptive fields improve sensing by increasing the discrimination performance of neurons in the presence of noise (Zhao et al., 2017).

The receptive field of a tactile afferent viewed as the set of all stimuli giving rise to the discharge of the afferent is actually much more complex than the receptive field measured by indenting the skin with a probe in various locations and counting the number of spikes elicited in the afferent. Indeed, the information conveyed by tactile afferents depends on many factors, including the branching of the nerve terminal, the mechanical properties of the mechanoreceptors and their anchoring in the surrounding tissue and the overall material properties of the surrounding tissue (Johansson and Flanagan, 2009). In addition, given that vibrations generated by the interaction with an object propagate throughout the skin without losing their information content (Delhaye et al., 2012; Manfredi et al., 2012; Shao et al., 2016), the actual receptive field of an afferent is considerably larger than the one probed by local skin indentation and illustrated in Fig. 1.8.

Finally, for a long time, each tactile afferent class has been attributed a dedicated function (Johnson, 2001). This overly simplified view of the functional properties of the tactile system has recently been proved inexact. Instead, afferents from different classes actually contribute together to many functions (Birznieks et al., 2001; Jenmalm et al., 2003; Khamis et al., 2014a, 2015, 2014b; Saal and Bensmaia, 2014). In the following sections, the response properties of the different classes of tactile afferents will be presented along with the main functions associated with these afferents. However, this does not mean that a given function is limited to the associated afferent, but rather that the afferent has the capacity to contribute effectively to the function given its response properties.

1.2.2. FA1 afferents and Meissner's corpuscles

FA1 afferents terminate in Meissner's corpuscles located in the dermal papillae, close to the surface of the skin (Fig. 1.9) (Cauna, 1956; Paré et al., 2001). These corpuscles are elongated receptors formed by a connective tissue capsule that comprises several lamellae of Schwann cells (Fig. 1.10). The center of the capsule contains 2–6 afferent fibers that terminate as disks between the Schwann cell laminae, a configuration thought to contribute to the transient response of these afferent to skin deformation (Iggo and Andres, 1982). A single Meissner's corpuscle is innervated by several FA1 afferents. Likewise, FA1 afferents branch in the skin to terminate into several Meissner's corpuscles (Paré et al., 2001, 2002a). This gives rise to spatially complex and overlapping receptive fields (Fig. 1.8) (Vallbo and Johansson, 1984).

FA1 afferents respond to transient deformation of the skin and are four times more sensitive than the SA1 afferents, but with a lower spatial acuity. Like SA1, they densely innervate the fingertips. They respond with short latency to skin stimulations such as the ones caused by tiny slips (Johansson and Vallbo, 1979; LaMotte and Whitehouse, 1986). This makes these fibers ideally suited for grip control. Indeed, their relative insensitivity to the static force and low-frequency vibrations allows them to extract signals related to transient events arising at the fingertip contact, such as a sudden slip e.g., rather than due to the forces required to grip the object (Abraira and Ginty, 2013; Johnson, 2001). They have been shown to contribute to slip detection between skin and object during grip (Johansson and Westling, 1984, 1987; Macefield and Johansson, 2003; Macefield et al., 1996) and during tactile exploration (Srinivasan et al., 1990). In addition, they contribute to the perception of textures moved across the skin (Weber et al., 2013).

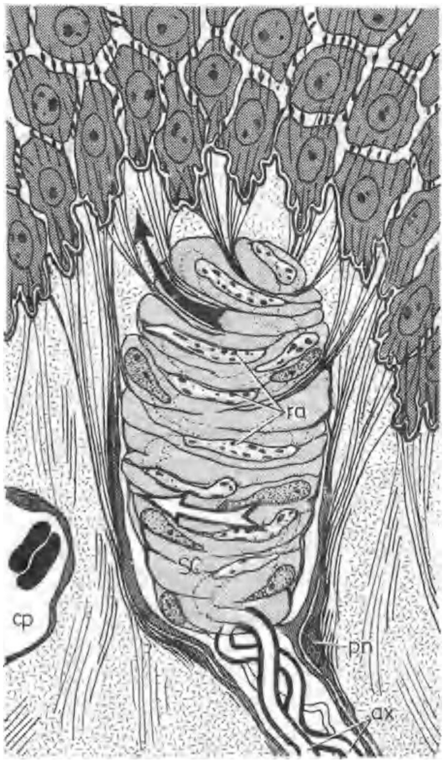

Fig. 1.10. Schematic representation of a Meissner corpuscle along with the collagen fibers that connect the basal epidermis to lamellar cells of the corpuscle. When the skin is deformed, the collagen network deforms the corpuscle (black arrow), which triggers a train of action potentials that quickly stops because of the adapting nature of the Meissner receptor. When the stimulus is removed, the corpuscle regains its shape, which induces another train of action potentials. Reproduced from Albe-Fessard et al. (1973).

1.2.3. SA1 afferents and the Merkel cell-neurite complex

Unmyelinated terminations of SA1 afferents innervate Merkel cells, which are specialized epidermal cells located in the tips of the primary epidermal ridges (Fig. 1.9) (Iggo and Muir, 1969). Merkel cells play an essential role in the response of SA1 afferents (Ikeda et al., 2014; Maricich et al., 2009). A single SA1 afferent branches heavily in the skin and innervates a large number of Merkel cells on several ridges (Paré et al., 2002a), giving rise to complex receptive fields with multiple hotspots (Fig. 1.8) (Vallbo and Johansson, 1984). Together, the afferent and the receptor cell form the Merkel cell-neurite complex. Recent investigations demonstrated a division of labor in the Merkel cell-neurite complex, with the Merkel cells signaling static stimuli, such as pressure, and the termination of the sensory afferent transducing dynamic stimuli, such moving gratings (Fig. 1.11) (Maksimovic et al., 2014). As a result, SA1 afferents respond to ramp-and-hold skin indentation with a burst of spikes followed by a sustained response decaying exponentially with irregular interspike intervals (Wellnitz et al., 2010; Williams et al., 2010). However, the Merkel cell-neurite complex does not account for all the variability in the firing properties of SA1 afferents. Indeed, the structure of the terminal branching of this afferent has also been shown to shape its response properties (Lesniak et al., 2014).

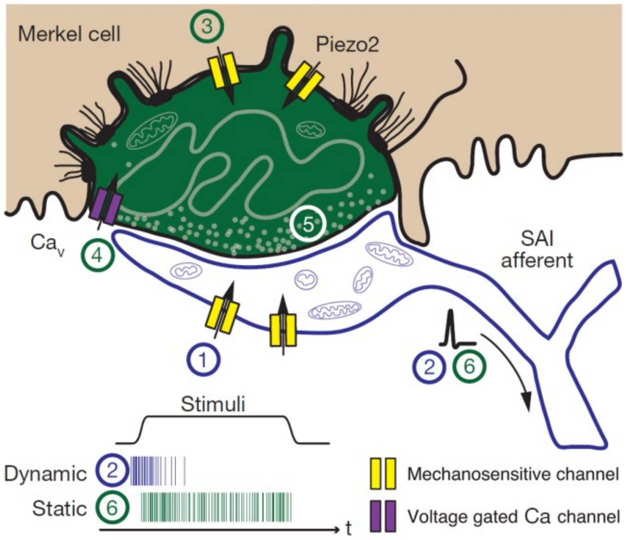

Fig. 1.11. Schematic representation of the Merkel cell-neurite complex and its role in touch reception. The interaction between Merkel cells and the termination of SA1 afferents explains the response to these fibers to sustained indentation of the skin. Deformation of the skin opens mechanotransduction channels in SA1 afferents (1) to initiate action potential firing at the onset of dynamic stimuli (2). The presence of Merkel cells boosts the dynamic response of SA1 afferents. Skin deformation simultaneously activates the *Piezo2* mechanotransduction channels in Merkel cells (3) to depolarize these cells, which produces calcium entry through voltage-activated calcium channels (CAv) (4) and release of neurotransmitters (5) that trigger sustained firing (6). Adapted from Maksimovic et al. (2014).

Like FA1 afferents, SA1 fibers densely innervate the fingertips (Vallbo and Johansson, 1984). SA1 afferents have the highest spatial resolution of all the sensory afferents; individual SA1 afferents can resolve spatial details of 0.5mm. In addition, SA1 afferents respond linearly to the indentation depth of a pattern scanned across their receptive field (Blake et al., 1997). This high spatial sensitivity makes them ideally suited for processing information about form and coarse texture (Johnson, 2001). In particular, SA1 afferents have been shown to encode pressure (Ge and Khalsa, 2002) and coarse spatial features like edges (Phillips and Johnson, 1981), curvature (Goodwin et al., 1995; Jenmalm et al., 2003) and embossed dots patterns like braille characters (Phillips et al., 1990). Given their sensitivity to static as well as low-frequency dynamic stimuli, they also participate in texture discrimination (Maricich et al., 2012).

1.2.4. FA2 afferents and Pacinian corpuscles

Each FA2 afferent terminates in a single Pacinian corpuscle (Paré et al., 2002a). These corpuscles are large receptors (up to 1mm) located deep in the dermis or in the subcutaneous tissue (Fig. 1.9). This onion-shaped receptor is formed of an unmyelinated neurite wrapped by an inner core, an outer core, and an external capsule (Fig.1.12) (Bell et al., 1994). The fluid-filled laminar structure of the receptor acts as a mechanical high-pass filter with a very sharp frequency response (Quindlen et al., 2016), which shapes the response of the afferent. Indeed, without the Pacinian receptor, FA2 afferents lose their phasic response to tactile stimuli (Loewenstein and Skalak, 1966).

FA2 afferents adapt more rapidly than FA1 afferents and therefore are sensitive to higher-frequency stimuli. They have the lowest sensory thresholds of all tactile afferents, with the ability to detect skin indentations as small as 10nm at 200Hz (Brisben et al., 1999). This extreme sensitivity combined with the deep location of their receptor causes the FA2 fibers to have almost no spatial resolution and a large receptive field that can span an entire hand with no clear boundaries (Fig. 1.8) (Vallbo and Johansson, 1984).

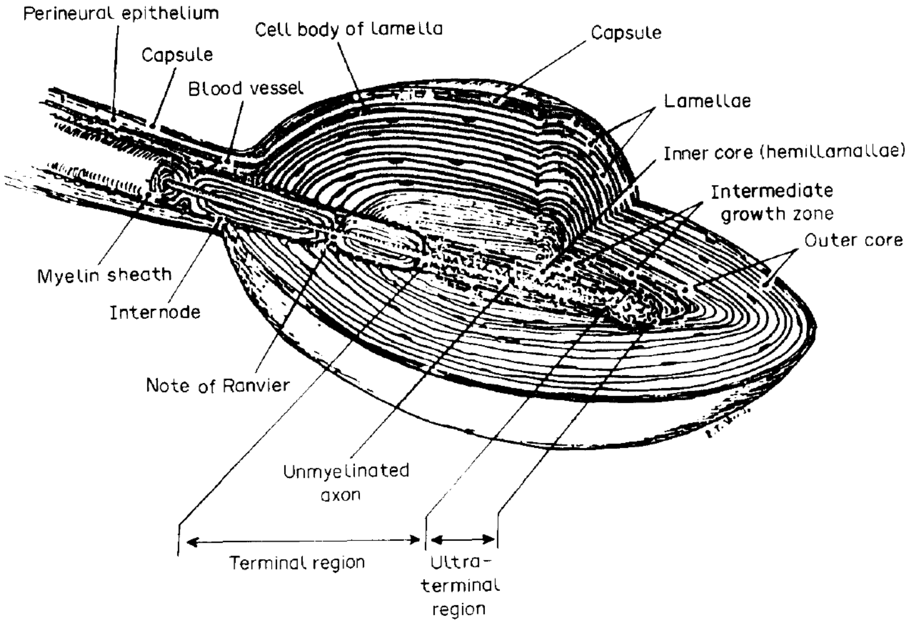

Fig. 1.12. Structure of the Pacinian mechanoreceptor. The receptor is formed of an unmyelinated dendrite wrapped tightly with non-neuronal cells constituting the inner core. This inner core is surrounded by an outer core also composed of non-neuronal concentric lamellae with the interlamellar spaces filled with fluid. The outer core in enclosed by the external capsule of the corpuscle. The fluid-filled laminar structure of the receptor acts as a mechanical high-pass filter, with the pressure at the center of the corpuscle being proportional to the deformation velocity. Reproduced from Bell et al. (1994).

Given their sharp response to high-frequency stimuli and their insensitivity to low-frequency forces and deformations of the skin, FA2 afferents are well suited to encode skin vibrations (Johnson, 2001). Indeed, they have been shown to detect vibrations almost as precisely as the auditory system (Formby et al., 1992). They can capture vibrations generated in the hand during tactile exploration (Bensmaïa and Hollins, 2005, 2003; Manfredi et al., 2012) and therefore contribute to the perception of fine textures (Hollins et al., 2001; Manfredi et al., 2014; Weber et al., 2013) and allow the tactile system to perceive extremely fine surface features (Skedung et al., 2013). Hand-held tools interacting with the environment generate high-frequency vibrations (Yoshioka et al., 2007) that can propagate through the skin without losing their frequency content (Manfredi et al., 2012). FA2 afferents therefore also contribute to the perception of texture explored with tools or probes as if they were explored with the fingers.

1.2.5. SA2 afferents and Ruffini corpuscles

SA2 afferents are 2–4 times more sensitive to skin stretch than SA1 afferents and less sensitive to skin indentation (Edin, 1992; Johnson, 2001). These afferents can fire spontaneously and they respond to ramp-and-hold skin stimulation with sustained firing with regular interspike intervals. Their receptive field is larger, with no clear borders (Fig. 1.8) (Vallbo and Johansson, 1984). Their capacity to encode skin stretch in a robust manner makes them suited for the following functions. First, in combination with SA1 afferents, they have been shown to encode the motion direction of an object moving over the surface of the skin causing skin stretch (Olausson et al., 2000). Second, they capture fingertip joint angle and hand configuration by encoding the specific patterns of skin stretch caused by each finger or hand configuration. In this, they present response properties similar to muscle spindles and joint afferents and are therefore thought to play a role in proprioception (Edin, 1992, 2004; Edin and Johansson, 1995). Third, a special type of SA2 afferents found in the border of the nail has been shown to encode forces applied to the fingertip, therefore conferring them a role in object manipulation (Birznieks et al., 2009).

Despite the clear role played by SA2 afferents in proprioception and object manipulation through their capacity to encode skin stretch, considerable controversy remains regarding the precise mechanisms mediating the response of these afferents. For a long time, SA2 afferents have been hypothesized to terminate in Ruffini corpuscles (Iggo and Andres, 1982). These corpuscles are elongated spindle-shaped receptors of relatively large dimensions (0.5mm to 2.0mm in length and 50–200μm in diameter) containing collagen bundles that are closely intermingled with highly branched, thin endings supplied by a large myelinated axon. They have been identified as the SA2 cutaneous mechanoreceptors in the cat, with discharge properties of the axons innervating Ruffini corpuscles presenting the same functional characteristics as SA2 afferents (Chambers et al., 1972). However, there is no evidence that SA2 afferents terminating in the human glabrous skin are associated with Ruffini corpuscles (Paré et al., 2002a, 2003). In addition, unlike other classes of afferents, the electrical stimulation of SA2 fibers does not evoke robust and reproducible sensations in human subjects (Vallbo et al., 1984). Therefore, the actual ending of SA2 afferents remains unknown. It is possible that several sub-classes of SA2 afferents exist, with different terminations. However, it is very unlikely that all SA2 afferents terminate in Ruffini corpuscles.

1.2.6. Up to the brain

Innervation of the human hand

The human hand is innervated by the radial, ulnar and median nerves. These nerves contain both efferent and afferent nerve fibers, conveying signals from and to the central nervous system, respectively, i.e. motor and sensory signals. Muscles involved in the precision grip are innervated by the radial nerve (fingers extension) and the median nerve (fingers flexion). Regarding sensory innervation (Fig. 1.13), the radial nerve innervates the radial portion of the dorsal side of the hand and the dorsal surface of the thumb. It also supplies sensibility to the dorsal surfaces of the index finger and the radial half of the middle finger. The median nerve innervates the palmar surface of the thumb, index and middle fingers and the radial side of the ring finger. The ulnar nerve innervates the little finger and the ulnar half of the ring finger on the palmar surface as well as the dorsal side of the hand over the ulnar half of the middle finger and over the ring and little fingers (Jones and Lederman, 2006).

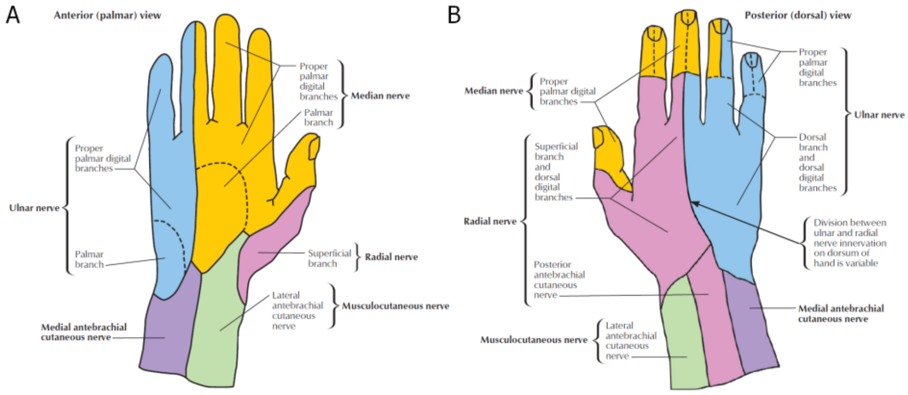

Fig. 1.13. Sensory innervation of the human hand. (A) Anterior (palmar) view. (B). Posterior (dorsal) view. Reproduced from Netter (2014).

The medial lemniscal pathway

The axons of the mechanosensory afferents grouped in the radial, ulnar and median nerves enter the spinal cord through the dorsal roots. These first-order neurons ascend ipsilaterally through the dorsal columns of the spinal cord to the brainstem, where they synapse on neurons in the cuneate nucleus of the medulla (Fig. 1.14). The second-order neurons in the cuneate nucleus send their axons to the contralateral somatic sensory portion of the thalamus. More precisely, they project in the ventral posterior lateral nucleus (VPL), where they synapse with thalamic neurons on the other side of the body. Finally, third-order neurons in the VPL send their axons to the cerebral cortex, in a region known as the anterior parietal cortex (APC) (Purves et al., 2012).

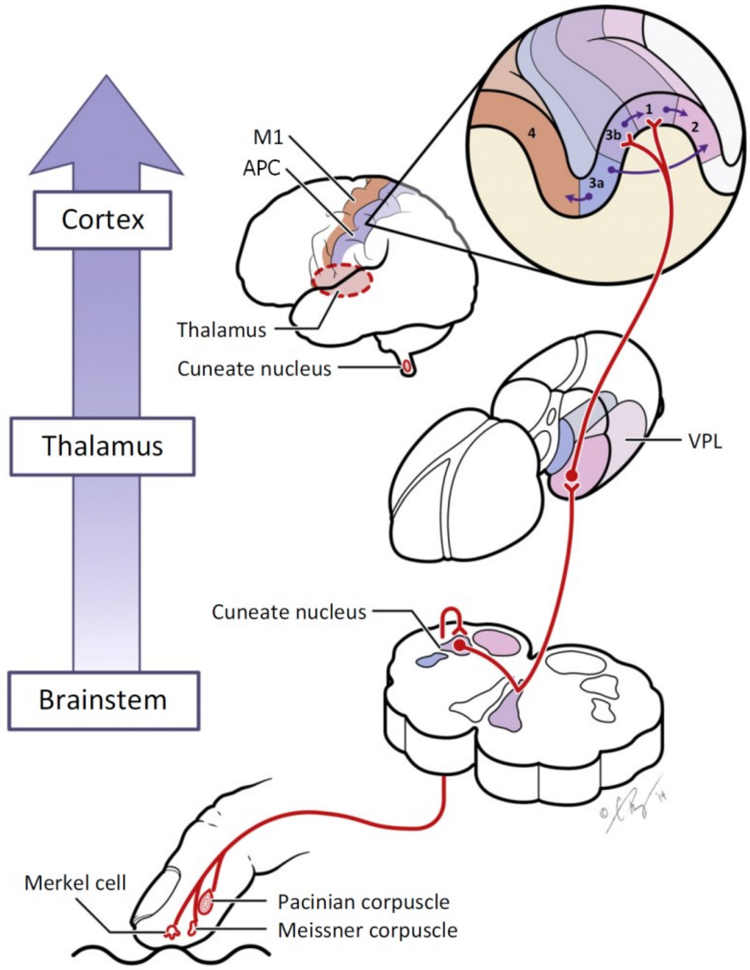

Fig. 1.14. Medial lemniscal pathway conveying mechanosensory information from the upper limb to the brain. Sensory information from the hand is conveyed from the peripheral transduction sites in the upper limb by the radial, ulnar and median nerves into the central nervous system. First-order neurons from the hand synapse in the cuneate nucleus of the medulla on second-order neurons. In turn, these second-order neurons synapse in the ventral posterior lateral nucleus (VPL) of the thalamus on third-order neurons that reach the anterior parietal cortex (APC) in Brodmann areas 3b and 1. Adapted from Saal and Bensmaia (2014) (original drawing from Christopher Raney).

The cerebral cortex

Signals elicited by tactile interactions ultimately reach the anterior parietal cortex (APC) in Brodmann areas 3b and 1. The APC is organized somatotopically, i.e. signals coming from different parts of the body are processed in separate regions. Parts of the body that are important for tactile discrimination, such as the tip of the tongue, the fingers, and the hand, have disproportionately large representations reflecting greater degrees of innervation (Kandel et al., 2000).

Signals from several classes of tactile afferents converge in the APC. Most neurons found in this brain region are neither slow adapting nor fast adapting but present a continuum of adaptation rates, with their response to skin indentation being explained by a combination of SA1 and FA1 responses (Pei et al., 2009). This convergence supports the hypothesis of a functional segregation of somatosensory neurons rather than a segregation based on the class of afferents that project to them (Saal and Bensmaia, 2014). In consequence, the brain is able to extract high-level features of tactile stimuli, which are briefly reviewed in the next section.

Besides the Brodmann areas 3b and 1, whose neurons respond primarily to cutaneous stimulations, the APC is also composed of two other areas, namely 3a and 2. Neurons in area 3a have a proprioceptive response, i.e. they respond primarily to muscle stretch and joint motion. Neurons in area 2 exhibit both cutaneous and proprioceptive responses (Taoka et al., 2000).

Behavioral studies indicate that the APC plays a crucial role in grasp control. Indeed, disturbances in the hand-related region of the contralateral APC induced via transcranial magnetic stimulation (TMS) delay the parallel increase in grip and load forces during object lift, resulting in a longer duration of the pre-load phase, presumably because of a disturbed processing of the somatosensory information (Lemon et al., 1995). Similarly, TMS-induced virtual lesions in the primary motor cortex (M1, corresponding to Brodmann area 4) affect the temporal relationship between changes in grip and load forces (Schabrun et al., 2008). Moreover, TMS-induced perturbations on the left anterior intraparietal area and the left dorsal premotor cortex also affect the coordination between grip and load forces during grasp control (Davare et al., 2006, 2007). Finally, the posterior parietal cortex has also been shown to be involved in the coordination of fingertip forces for grasp stability in manipulation (Ehrsson et al., 2003).

A detailed description of the cortical areas involved in grasp control is beyond the scope of this text. More information on this topic is available in review papers for the interested reader (Davare et al., 2011; Grafton, 2010). The important information from this section is that grasp control is a complex process that results from the interaction of many brain areas and relies on multiple sensory modalities, including touch, proprioception, and vision, as well as on sensorimotor memories (Johansson and Flanagan, 2009).

1.2.7. The richness of high-level tactile perception

The integration of signals from several classes of afferents endows the central nervous system with the capacity to extract complex and high-level features of the tactile stimuli. For instance, FA1 and SA1 afferents combine their high temporal and spatial resolution, respectively, to provide the central nervous system with a precise image of the shape of surfaces stroking the skin.

Similarly, signals from several classes of tactile afferents are combined in the encoding of the following features: stimulus intensity (Bensmaia, 2008; Muniak et al., 2007), texture (Weber et al., 2013), surface curvature (Jenmalm et al., 2003), slip between fingertip and object during manipulation (Johansson and Westling, 1987) or tactile exploration (Srinivasan et al., 1990), and forces and torques applied to the finger pad (Birznieks et al., 2001, 2009, 2010; Paré et al., 2002b). This makes sense because these physical stimuli are prone to excite afferents from several classes, each class being sensitive to the stimuli in its own way. Therefore, the combination of signals from different classes of afferents enables the brain to form a more accurate image of the features listed above than would be possible by relying only on one afferent class.

Building upon the many features captured by the peripheral tactile system, the brain is able to extract abstract features of the stimuli such as tactile speed (Dallmann et al., 2015; Moscatelli et al., 2014; Salada et al., 2004), friction (Johansson and Westling, 1984; Smith and Scott, 1996), object shape (Hsiao, 2008), surface roughness (Boundy-Singer et al., 2017; Goodman and Bensmaia, 2017), or edge orientation (Pruszynski and Johansson, 2014; Pruszynski et al., 2017).

In conclusion, the complex neural circuitry underlying the tactile system provides us with a rich and multi-dimensional perceptual probe (Hayward, 2011) to sense our environment, the understanding of which is still in its early stages.

1.3. Tactile feedback in object manipulation

Humans are able to manipulate objects with high dexterity. They can optimally adjust the grip force (GF) exerted on objects to the object load and to the fingertip contact friction (Cadoret and Smith, 1996; Flanagan and Wing, 1997; Westling and Johansson, 1984). The control of GF relies on many factors, including the mechanical properties of the contact surface (Johansson and Westling, 1984), the sensory information provided by tactile afferents (Witney et al., 2004), proprioceptive afferents (Macefield and Johansson, 2003), and vision (Diamond et al., 2015; Johansson et al., 2001), and the expected dynamics of the object, also called internal models (Flanagan et al., 2006; Wolpert and Flanagan, 2001). Therefore, two distinct control processes interact during manipulation: (1) feedforward control based on predicted object dynamics, and (2) feedback control based on sensory information sent to the central nervous system (CNS). It is believed that these two processes are combined in a Bayesian integration process in which each signal is given a relative importance proportional to its reliability (Crevecoeur et al., 2010; Körding and Wolpert, 2004). For instance, during the early moments of object grasping, GF is controlled in feedforward because of the lack of sensory information due to the large delays in the sensorimotor control loop (approximately 100ms) (Miall et al., 1993). However, the CNS soon uses the sensory feedback arising from the tactile and proprioceptive afferents to adapt its motor commands to the behavior of the object.

Proprioceptive feedback arises from fast-conducting myelinated afferents that provide information about joint configurations and muscles states. More precisely, proprioceptive afferents can convey information about joint kinematics and torques (Binder et al., 2009) and complex signals linked to muscle dynamics and coupling between muscle groups (Dimitriou, 2014; Dimitriou and Edin, 2010). Mechanical perturbations to the digits evoke a well-known series of events starting with the spinal stretch response, followed by long-latency responses known to express flexible and task-specific modulation (Macefield and Johansson, 1996; Manning and Bawa, 2011; Marsden et al., 1976; Rothwell et al., 1982). In addition, perturbations to the upper limb during manipulation evoke a coordinated response in arm and hand muscles starting at around 60ms (Crevecoeur et al., 2016).

Tactile feedback arises from tactile afferents innervating the hand and arm that have been described in the previous section. Given the complex response properties and receptive fields of these afferents, their response is modulated simultaneously by several parameters relevant to object manipulation, such as the shape and curvature of the contacting object, the position of contact on the skin, and the magnitude and direction of contact force (Goodwin and Wheat, 2004). Therefore, all classes of tactile afferents contribute to object manipulation, so that it is difficult to assess how a given parameter is encoded in the neural signals (Saal and Bensmaia, 2014). FA1 afferents have been shown to respond to transient slip during manipulation (Westling and Johansson, 1987). Together with SA1 afferents, they also encode object curvature (Jenmalm et al., 2003), and forces and torques applied on the object by the fingers (Birznieks et al., 2001, 2010). FA2 afferents being sensitive to vibrations, they respond during initial contact between fingers and object (Westling and Johansson, 1987), and to vibrations generated by slips between fingers and object (Johansson and Westling, 1987; Srinivasan et al., 1990). Because these vibrations propagate through the tissues, tactile responses are also evoked in FA2 afferents away from the contact (Manfredi et al., 2012). Finally, SA2 afferents in the borders of fingernails encode fingertip forces (Birznieks et al., 2009) whereas other SA2 afferents contribute to proprioceptive feedback (Edin, 1992; Edin and Johansson, 1995).

Previous studies demonstrated the importance of tactile feedback during manipulation. First, the loss of tactile feedback through digital anesthesia disrupts GF control even when subjects had prior experience with the object (Augurelle et al., 2003; Monzée et al., 2003). Second, there is evidence that tactile feedback not only assists GF control in providing information about the state of the fingertip contact but also plays a critical role in providing a tonic excitatory drive to intrinsic hand muscles, which is required to set and maintain the background level of GF (Augurelle et al., 2003; Witney et al., 2004). Besides, tactile feedback has been shown to trigger corrective motor responses during manipulation (Birznieks et al., 1998; Garnett and Stephens, 1980; Macefield and Johansson, 2003; Macefield et al., 1996; Pruszynski et al., 2016). Therefore, it is clear that tactile signals contribute to online feedback control of GF. In addition, a continuous tactile feedback is required for efficient manipulation in order to not only update but also maintain internal models driving anticipatory (feedforward) control of GF (Witney et al., 2004).

However, it is not clear how proprioceptive and tactile signals are integrated within sensorimotor control loops, even though there is evidence that each sensory system contributes to force control during manipulation.

A recent study attributed distinct roles to proprioceptive and tactile afferents during online control of finger forces, with proprioception being involved in a rapid, automatic sensorimotor response, and tactile signals driving a slower, goal-directed response (Crevecoeur et al., 2017). There is evidence that multiple sensory modalities are integrated within the CNS using maximum-likelihood estimation (Ernst and Banks, 2002). However, beyond that, the neural mechanisms of multisensory integration during GF control remain a puzzle.

Observing that manipulation tasks are characterized by a sequence of action phases separated by contact events that define task subgoals, Johansson and colleagues proposed that the CNS implements a “discrete-event sensory-driven control policy” to control manipulation. This control model seeks to explain how predictive feedforward mechanisms integrate somatosensory and visual information with expected object properties and sensorimotor memories to control manipulation in a robust, yet flexible manner (Johansson and Cole, 1992; Johansson and Flanagan, 2009). In this model inspired by finite-state control systems in engineering, a given manipulation task like grasping and holding an object is divided into subtasks separated by discrete control points where actual and expected sensory information are compared. For instance, the subtasks would be to reach, load, lift and then hold the object. The goal of the initial reach phase is marked by the digits contacting the object and the goal of the subsequent load phase is marked by the breaking of contact between the object and the support surface. Therefore, in addition to generating motor commands, each action-phase controller predicts the sensory events that signify subgoal attainment. Mismatches between actual and expected sensory events trigger corrective actions, providing flexibility to the overall control scheme. This model does not explain, however, why tonic input, i.e. continuous activation, from tactile afferents is necessary for successful force coordination during manipulation (Witney et al., 2004).

As suggested by the discrete-event control policy, feedforward and feedback control processes are not opposed but complementary during manipulation, with sensory feedback signals updating predictions of internal models and feedforward control compensating for the delays and noise between peripheral sensory receptors and the central nervous system. Even though statistical frameworks based on Bayesian integration (Körding and Wolpert, 2004) and computational frameworks based on optimal control (Scott, 2004) have been proposed to explain how these two control schemes are integrated, much work remains to be done to understand precisely the interplay between these two processes during manipulation.

1.4. Thesis content

1.4.1. Open questions

During object manipulation, the minimum grip force required to avoid object slippage depends on the frictional properties of the fingertip contact. Therefore, fingertip friction should be measured and taken into account when seeking to understand subjects' performance during manipulation. Friction is affected by the complex mechanical properties of the fingertip and in particular, it has been shown to vary dramatically with the contact force. However, no method is available to date that allows a rapid and reproducible measure of fingertip friction, taking into account its dependence on normal load.

Partial slips have been shown to arise systematically prior to full slip under tangential loading of the fingertip. Although the mechanics of partial slips is well characterized, the perception of such events remains unclear as well as the mechanisms allowing subjects to perceive slip under their fingertip.

Besides, tactile feedback plays a critical role during object manipulation. This feedback arises from the precise response of the tactile afferents to the complex mechanical deformations of the finger pad during manipulation. However, very few studies monitored the mechanical behavior of the fingertip contact during manipulation. In addition, it is not clear how partial slips and surface deformations at the finger contact are encoded in the tactile system.

To address these gaps, a series of studies were performed with the following research questions in mind:

- Given that fingertip friction is affected by fingertip morphology and properties like the intrinsic level of skin hydration that varies from subject to subject, how to quickly measure fingertip friction with a given subject, including its dependence on the normal force?
- What are the physical factors influencing the perception of fingertip slip? Given the smooth transition from stick to slip on smooth surfaces, are subjects able to perceive fingertip slip before full slip?

- Given the systematic occurrence of partial slips under tangential loading of the fingertip in passive conditions, are partial slips also present during active object manipulation? If so, do they provide relevant information to the central nervous system that would help it to control finger forces during manipulation?
- How are skin deformations caused by partial slips encoded in the somatosensory periphery?

1.4.2. Overview

In this introduction (Chapter 1), we present the general context of the work by reviewing the current knowledge about mechanical properties of the finger pad, the structure and functions of the tactile system, and its role during object manipulation. In Chapter 2, we describe a novel method allowing the static coefficient of friction at the fingertip contact to be measured easily, taking into account its dependence on the normal load. In addition, we explain how this measure allows the static coefficient of friction and therefore the safety margin to be estimated during manipulation. In Chapter 3, we examine the perception of partial slip by human subjects as well as the physical parameters involved in fingertip slip perception. Based on the observations made in this study, a new mechanism of slip perception on smooth surfaces is proposed. In addition, it is demonstrated that subjects have the ability to anticipate full slip of the fingertip contact. This has functional consequences for object manipulation because this early slip detection may allow subjects to correct their grip force before dropping the object. To investigate the dynamics of partial slips and surface strains at the fingertip contact during manipulation, we built a novel manipulandum combining sensing of the forces applied by the fingers holding the object and imaging of the fingertip contact. This device is described in Chapter 4 along with preliminary results highlighting the presence of partial slips during manipulation. To better understand how tactile feedback arises from finger pad mechanics during manipulation, Chapter 5 examines tactile afferent responses elicited by strain patterns produced at the surface of the skin under fingertip shearing in conditions compatible with object manipulation. Finally, in Chapter 6, we summarize the contributions of this thesis, we identify new research questions that are worth investigating, and we discuss potential applications of the work.

1.4.3. Publications and communications

Journal papers

Simple and reliable method to estimate the fingertip static coefficient of friction in precision grip. Barrea* A., Córdova Bulens* D., Lefèvre P., and Thonnard J.-L. (*) equal contribution. IEEE Transactions on Haptics (2016) 9(4): 492-498.
http://dx.doi.org/10.1109/TOH.2016.2609921

This paper is presented in Chapter 2.

Surface strain measurements of fingertip skin under shearing. Delhaye B.P., Barrea A., Edin B.B., Lefèvre P., and Thonnard J.-L. Journal of the Royal Society Interface (2016) 13: 20150874.
http://dx.doi.org/10.1098/rsif.2015.0874

My contribution to this paper was to participate in the development of the image analysis code and of the theoretical model of the deformations within the fingertip contact. In addition, I contributed to the drafting of the manuscript.

Multisensory components of rapid motor responses to fingertip loading. Crevecoeur F., Barrea A., Libouton X., Thonnard J.-L., and Lefèvre P. Journal of Neurophysiology (2017) 118(1): 331-343.
http://dx.doi.org/10.1152/jn.00091.2017

My contribution to this paper was to measure the deformations occurring in the fingertip contact during stimulations and to contribute to the drafting of the manuscript.

Submitted paper

Perception of partial slips under tangential loading of the fingertip. Barrea A., Delhaye B.P., Lefèvre P., and Thonnard J.-L. Submitted to Nature Scientific Reports.

This paper is presented in Chapter 3.

Conference communications

A simple and reliable method to measure the fingertip coefficient of friction at different levels of grip force. Barrea* A., Córdova Bulens* D., Lefèvre P., and Thonnard J.-L. (*) equal contribution. 24th Annual Meeting of the Society for the Neural Control of Movement, Amsterdam, The Netherlands (2014). Poster presentation.

Perception of partial slips under tangential loading of the fingertip. Barrea A., Delhaye B.P., Lefèvre P., and Thonnard J.-L. 45th Annual Meeting of the Society for Neuroscience, Chicago, IL (2015). Poster presentation.

Perception of partial slips under tangential loading of the fingertip. Barrea A., Delhaye B.P., Lefèvre P., and Thonnard J.-L. Eurohaptics 2016 (10th International Conference on Haptics), London, UK (2016). Work-in-progress paper and poster presentation.

Human tactile afferent responses to skin strain patterns caused by fingertip shearing. Barrea* A., Jarocka* E., Lefèvre P., Thonnard J.-L., Edin B.B., and Delhaye B.P. (*) equal contribution. 46th Annual Meeting of the Society for Neuroscience, San Diego, CA (2016). Poster presentation.

Finger pad mechanics during dexterous object manipulation. Barrea A., Delhaye B.P., Lefèvre P., and Thonnard J.-L. IEEE World Haptics Conference 2017, Munich, Germany (2017). Work-in-progress paper and poster presentation. **Best work-in-progress paper award.**

CHAPTER 2

Simple and reliable method to estimate the fingertip static coefficient of friction in precision grip

"The heart of science is measurement."

Erik Brynjolfsson

Published as: A. Barrea*, D. Cordova Bulens*, P. Lefèvre and J.-L. Thonnard, "Simple and Reliable Method to Estimate the Fingertip Static Coefficient of Friction in Precision Grip," in IEEE Transactions on Haptics, vol. 9, no. 4, pp. 492-498, Oct.-Dec. 2016. (*) equal contribution.

The static coefficient of friction (μ_{static}) plays an important role in dexterous object manipulation. Minimum normal force (i.e., grip force) needed to avoid dropping an object is determined by the tangential force at the fingertip-object contact and the frictional properties of the skin-object contact. Although frequently assumed to be constant for all levels of normal force (NF, the force normal to the contact), μ_{static} actually varies nonlinearly with NF and increases at low NF levels. No method is currently available to measure the relationship between μ_{static} and NF easily. Therefore, we propose a new method allowing the simple and reliable measurement of the fingertip μ_{static} at different NF levels, as well as an algorithm for determining

μ_{static} from measured forces and torques. Our method is based on active, back-and-froth movements of a subject's finger on the surface of a fixed six-axis force and torque sensor. μ_{static} is computed as the ratio of the tangential to the normal force at slip onset. A negative power law captures the relationship between μ_{static} and NF. Our method allows the continuous estimation of μ_{static} as a function of NF during dexterous manipulation, based on the relationship between μ_{static} and NF measured before manipulation.

2.1. Introduction

Humans have the remarkable capacity to manipulate small objects with great dexterity. In precision grip (i.e., when holding an object between the thumb and index finger), contact forces at the fingertip-object interface are typically decomposed into two components: the force normal to the object's surface and directly controlled by the subject (normal force, NF), and the force tangential to the object's surface and resulting from the object's weight an inertial forces (tangential force, TF) (Johansson and Westling, 1984). To ensure a stable grasp of the object under predictable conditions, the central nervous system continuously scales and synchronizes NF to the varying TF (Flanagan and Wing, 1993, 1995).

To examine how NF follows the variations of TF, Westling and Johansson introduced the concept of the "safety margin", defined as the difference between the exerted NF and the minimum NF that would prevent slippage (Westling and Johansson, 1984). This indicator is widely used when examining human performance in dexterous manipulation tasks (Augurelle et al., 2003; de Freitas et al., 2009; Hadjiosif and Smith, 2015). To compute the safety margin, one must measure the instantaneous NF and estimate the minimum NF necessary to prevent object drop. The latter is achieved by measuring the static coefficient of friction (μ_{static}) at the fingertip-object contact. In precision grip, μ_{static} is defined as the ratio of TF over NF when the object starts slipping.

In contact mechanics, Amontons' law describes frictional forces as being proportional to the applied load and independent of the apparent contact area (Gao et al., 2004). This property indicates that μ_{static} is constant and independent of the normal force (i.e., the force perpendicular to the contact surface). However, several studies have reported that the human skin μ_{static} varies nonlinearly with normal force (Adams et al., 2007, 2013; André et al., 2009; van Kuilenburg et al., 2013), such that Amontons' law cannot be applied to fingertip-object contact. Normal force varies continuously during object manipulation, in order to compensate for inertial forces. Therefore, to obtain a good estimate of μ_{static} at each moment during a manipulation task, μ_{static} must be measured at the fingertip-object interface for the whole range of normal force variation.

To evaluate the fingertip μ_{static}, the slip onset must be accurately detected. Several methods for this detection have been developed. The most popular method in dexterous manipulation is the one proposed by Westling and Johansson in (Westling and Johansson, 1984). In this seminal study, the authors asked subjects to grasp and lift an instrumented manipulandum with the thumb and index finger. Then, subjects released the grip slowly until the object dropped.

Despite its popularity, this technique suffers from several drawbacks. First, it does not account for the dependence of μ_{static} on NF. Indeed, inertial forces are negligible in this method and therefore NF at slip onset is only determined by the weight of the manipulated object. Second, the measurements vary significantly between trials. Indeed, the slip onset is very difficult to detect because of the rapid variation of force signals at this moment. Thus, obtaining a reliable estimate of μ_{static} with this method would require very long and tedious testing, with numerous repetitions to compensate for variability and different manipulandum weights to test different values of NF. Finally, this method requires fine motor coordination. Therefore, it is difficult to use with patients exhibiting motor impairments or with children.

To overcome these limitations, André et al. proposed a method able to capture the dependence of μ_{static} on NF in (André et al., 2009). They asked subjects to pinch a manipulandum equipped with force sensors between the thumb and index finger, and to maintain NF at a prescribed level. Then, springs connected to the manipulandum were loaded by a linear actuator, which progressively increased TF. This caused the fingers to slip on the contact surface. Although this procedure allows μ_{static} to be measured for several values of NF, it also has some shortcomings. Specifically, this method requires a dedicated device to move the manipulandum, and the procedure cannot be carried out quickly. Similarly to this method, other studies have also investigated the idea of moving the contact surface relative to the finger with an actuator (Han et al., 1996; Savescu et al., 2008).

In short, μ_{static} is necessary to estimate the safety margin in dexterous manipulation, and varies with NF. However, no method is currently available that is able to capture quickly the dependence of μ_{static} on NF. Here, we propose a new method to measure μ_{static} while accounting for the effect of NF. This method enables the continuous estimation of μ_{static} during dexterous object manipulation, based on the relationship between μ_{static} and NF measured before manipulation. Our experimental procedure is accompanied by a dedicated algorithm able to detect slip onsets automatically from the data in order to compute μ_{static}.

2.2. Material and methods

2.2.1. Subjects

Twelve healthy subjects (age: 18–60 years; 9 men, 3 women) participated in the study. All subjects provided informed consent to participate in the procedure, which was approved by the local ethics committee.

2.2.2. Apparatus

For this experiment, we used a manipulandum (Fig. 2.1A) equipped with two six-axis force and torque sensors (Mini-40 F/T sensors, ATI Industrial Automation, NC, USA) covered with Kapton polyimide film (DuPont, DE, USA). The manipulandum was fixed on a table (Fig. 2.1B). Forces and torques were recorded at a rate of 1kHz with resolutions of 1/50N (for force) and 1/4000Nm (for torque). A screen, placed in front of subjects, provided real-time visual feedback of the average NF applied on the manipulandum by the thumb and index finger.

The fingertip moisture of the subjects was measured with a dedicated moisture sensor (Corneometer CM 825, Courage + Khazaka electronic GmbH, Köln, Germany), measuring moisture content at the level of the stratum corneum. This sensor provides measures ranging from 20 to 120 arbitrary units, a higher number corresponding to a moisture skin (Fluhr et al., 1999; Heinrich et al., 2003).

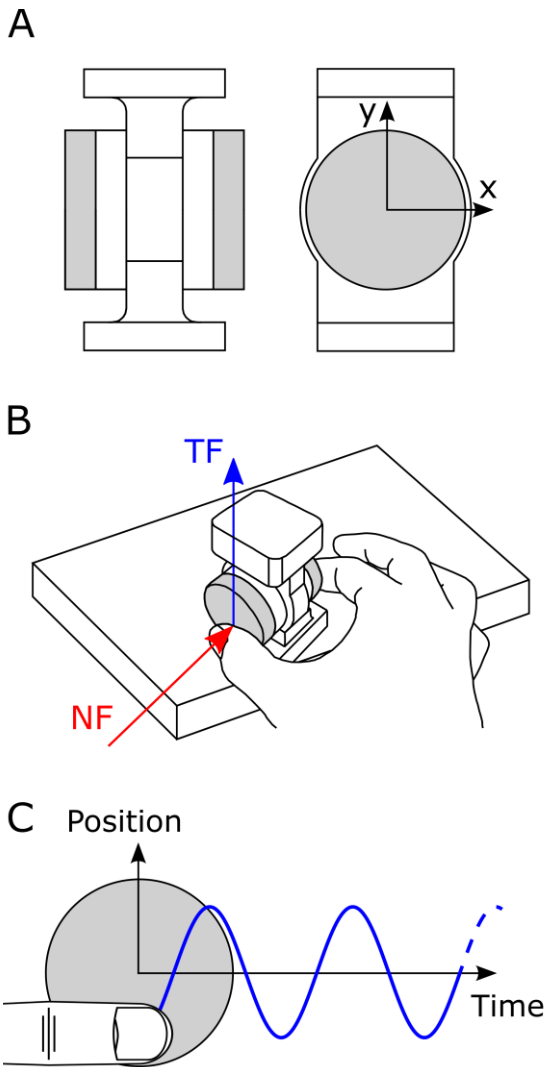

Fig. 2.1. Setup. (A) Manipulandum used for the experiment. The manipulandum was equipped with two six-axis force and torque sensors (shaded in gray), which were covered with Kapton polyimide film (DuPont, DE, USA). **(B)** Subjects pinched the manipulandum, which was fixed on a table, between their thumb and index finger. Fingertip-object interaction forces were decomposed into components normal (NF) and tangential (TF) to the sensor surface. **(C)** During trials, subjects performed vertical back-and-forth movements with their hand without releasing their grip. Blue curve shows the vertical trajectory of a finger moving on a force sensor.

2.2.3. Experimental procedure

Before performing the experiment, all subjects washed their hands using water and soap. The hands were rested for approximately 10 minutes, to allow the skin to regain its natural hydration level. Subjects sat in front of the table to which the manipulandum was fixed. The temperature in the room was kept constant at 21°C. During a typical trial, subjects pinched the fixed manipulandum and performed five vertical back-and-forth movements with their hand at moderate speed without releasing their grip (Fig. 2.1C). with the help of visual feedback, subjects were asked to adjust their NF to a given reference level at the beginning of each trial, and to maintain their NF close to this reference level throughout the trial. Subjects were invited to rub the manipulandum at a moderate pace. The measured rubbing speed ranged between 5 and 15mm/s. After completing five vertical back-and-forth movements, subjects stopped rubbing the manipulandum and released their grip. Moisture levels of the thumb and index finger were measured at the beginning of the experiment and after each trial. Forces and torques were continuously recorded during trials.

Reference NF levels for the five trials were 0.5, 1, 2, 4, and 8N. This range was tested in a previous study (André et al., 2009), which found that μ_{static} varied dramatically with NF values below 5N. Subjects found it difficult to maintain their NF precisely at the instructed level during a trial, as illustrated in Fig. 2.2C. However, as their NF values remained close to the reference NF value for each trial, the goal of spanning the whole range of NF values across repetitions was achieved. The complete procedure lasted 15 minutes or less with unexperienced subjects.

2.2.4. Data processing

For data processing and analysis, we considered the two force sensors independently. Indeed, the method described here considers only one force sensor at a time. Given that each force sensor was dedicated to a single finger, μ_{static} was analyzed independently for the thumb and the index finger. The force exerted by a finger normally to a single force sensor was denoted as NF. The force exerted by a finger tangentially to the force sensor was denoted as TF. These forces are illustrated in Fig. 2.1B.

We computed the center of pressure (COP) of the fingertip from the measured forces and torques. COP was defined as the point where the resultant interaction force between the fingertip and the force sensor was acting on the sensor. The x-y coordinates of COP on the force sensor were computed by using the following formula:

$$COP = \left(-\frac{T_y}{NF}, \frac{T_x}{NF}\right) \quad (2.1)$$

where T_x and T_y denote torques measured about the x and y axes, respectively, which are tangential to the surface of the sensor (Fig. 2.1A). Measured force signals were low-pass filtered using a 4^{th}-order Butterworth filter with a cut-off frequency of 75Hz.

2.2.5. Data analysis

We developed a method to compute μstatic, based solely on the forces and torques measured under a given fingertip. Fig. 2.2 presents a portion of a typical trial for the index finger of subject S03.

Fig. 2.2A shows the COP trajectory on the force sensor. Because vertical back-and-forth movements were made, we considered only the vertical component of the COP trajectory in the analysis (Fig. 2.2B). In support of this choice, we found that the discrepancy between the total and vertical amplitudes of the COP trajectory was less than 5 percent. We chunked the vertical component of the COP trajectory into several individual movements, using the extrema of the COP trajectory as separating points.

As mentioned earlier, computing μ_{static} requires identifying slip onset on each movement. To this end, we defined a "useful zone" in each movement, where slip is expected to occur (Fig. 2.2B). Due to varying fingertip morphologies between subjects and given that individual movements started from different vertical positions on the force sensor, we set the threshold delimiting useful zones beyond and above half the range of the sensor, to guarantee that each zone would be sufficiently large to include the slip onset of the corresponding movement. This threshold was determined arbitrarily and was kept constant across all subjects and all normal force conditions.

Next, we searched for the slip onset in each useful zone by looking for the maximum TF/NF in each zone (red dots in Fig. 2.2E). TF/NF maxima provide good markers for slip onsets because the material covering the force sensors exhibits a static coefficient of friction that is larger than the dynamic one. As a result, the TF and TF/NF values decrease slightly at slip onset. Implementation of the overall procedure in MATLAB (MathWorks, Natick, MA, USA) and tools for visualizing the data are described in Appendix B.

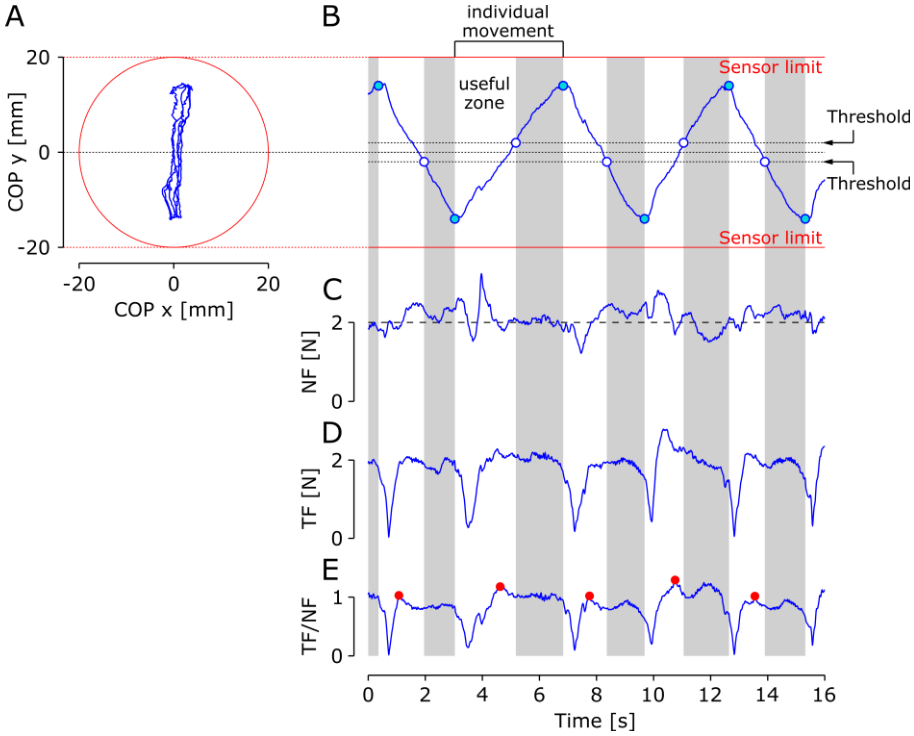

Fig. 2.2. Typical traces and description of the method. Data represent a subset of the complete trial for subject S03 with a reference NF of 2N. **(A)** COP trajectory (blue curve) on the force sensor and force sensor boundary (red circle). **(B)** Data were chunked into individual movements based on the extrema (blue dots) of the vertical COP trajectory (blue curve). "Useful zone" (white) for each movement starts at an extremum of the COP and ends when the COP crosses a custom threshold (white dots). Such a zone corresponds to the portion of a movement where the slip onset is expected to occur. Red lines indicate force sensor boundaries. **(C)** Force exerted by the subject normally to the surface of the sensor (NF, blue curve) and reference NF level (black line). **(D)** Force exerted by the subject tangentially to the surface of the sensor (TF, blue curve). **(E)** Ratio of TF/NF (blue curve) and maxima of TF/NF in each useful zone (red dots), indicating slip onsets. μ_{static} was measured as TF/NF at slip onsets. Finally, we observed that the COP position could be 10mm away from the reversal point when slip is detected. This is due to finger pad compliance and fingertip rolling against the surface of the force sensor.

2.2.6. Statistical analysis

For each subject, a negative power law was fitted to the data to quantify the relationship between μ_{static} and NF. This power law, which has been used in several previous studies (Adams et al., 2013; André et al., 2009; Wolfram, 1983), was expressed as:

$$\mu_{static} = k(NF)^{n-1} \tag{2.2}$$

Fit parameters k and n were obtained by using an ordinary least-squares regression procedure. Paired t-tests were carried out to test for differences in the fit parameters between the two fingers and to assess the repeatability of the method.

2.3. Results

Fig. 2.3 presents the measured values of μ_{static} and the corresponding normal force (NF) values for the 12 tested subjects. This figure clearly shows the relationship between μ_{static} and NF for all subjects. For high values of NF (> 5N), μ_{static} had a constant low value. As NF decreased, μ_{static} increased dramatically, often reaching values above 2 for forces below 0.5N.

A negative power function of the form $\mu_{static} = k(NF)^{n-1}$ was fitted to the data to capture the relationship between μ_{static} and NF for each subject (solid lines in Fig. 2.3). Table 2.1 reports the values of parameters k and n, the coefficient of determination (R^2) of the fit, and the moisture levels for the thumb and index finger for all subjects. The R^2 values were large for all fits, with a mean (M) of 0.84 and standard deviation (SD) of 0.14, indicating that the power law correctly captured the effect of NF on μ_{static}.

To test whether data acquired for the thumb and index finger were different, we conducted paired t-tests on fit parameters k and n from both groups of data. Fit parameters were not significantly different for thumb versus index finger data ($t(11) = 1.65$, $p > 0.05$ for k; $t(11) = 0.23$, $p > 0.05$ for n). In addition, the correlations between thumb and index finger data were 0.85 and 0.84 for k and n, respectively. Therefore, measuring μ_{static} of only one of the two fingers can be considered as sufficient to capture the influence of NF on μ_{static} for a given subject.

For six of the twelve subjects, a second measurement session was performed a week after the first. To test the repeatability of the measurements from the two test sessions, we used paired t-tests conducted separately on the two fit parameters, with the measurement session as the independent variable. No significant difference was found between fit parameters from the two sessions ($t(5) = 0.98$, $p > 0.05$ for k; $t(5) = 0.98$, $p > 0.05$ for n). Thus, results obtained by the proposed method were not significantly different across measurement sessions. In addition, the correlations between data from the two sessions were 0.84 and 0.61 for k and n, respectively.

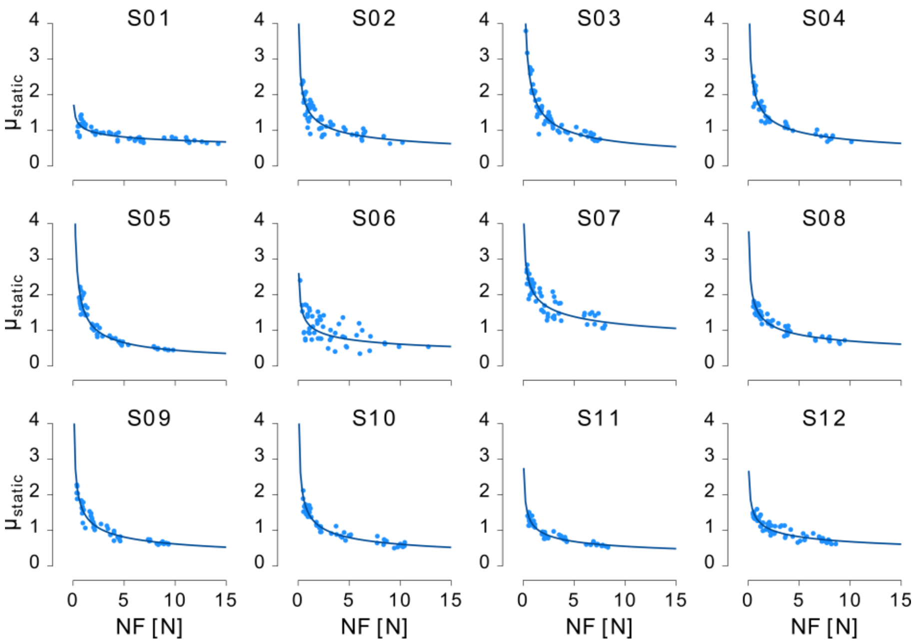

Fig. 2.3. Relationship between μ_{static} and NF. For each of the 12 unexperienced subjects (S01 to S12), μ_{static} data for the index finger were plotted against corresponding values of NF at slip onset (blue dots). A power law function was fitted to individual subject data (blue curve).

Table 2.1. Experimental data. Fit parameters k and n, coefficient of determination (R^2) of the fits, and moisture level for the 12 subjects (M ± SD) for the thumb and index finger. Moisture measurements are provided in arbitrary units ranging from 20 to 120.

	Thumb				Index			
Subject	k	n	R^2	Moisture (M ± SD)	k	n	R^2	Moisture (M ± SD)
S01	1.26	0.76	0.80	30 ± 6	1.07	0.83	0.65	36 ± 5
S02	1.60	0.59	0.86	34 ± 3	1.56	0.66	0.77	58 ± 11
S03	2.05	0.55	0.90	76 ± 9	2.02	0.52	0.92	86 ± 13
S04	1.49	0.64	0.94	40 ± 5	1.75	0.63	0.90	65 ± 7
S05	1.69	0.54	0.94	61 ± 7	1.61	0.44	0.91	52 ± 4
S06	1.35	0.76	0.50	72 ± 8	1.18	0.72	0.42	75 ± 5
S07	2.05	0.69	0.93	38 ± 3	2.06	0.75	0.81	51 ± 2
S08	1.54	0.71	0.90	95 ± 6	1.50	0.67	0.90	114 ± 4
S09	1.48	0.61	0.94	99 ± 5	1.53	0.61	0.92	105 ± 8
S10	1.68	0.65	0.93	83 ± 7	1.49	0.61	0.92	93 ± 6
S11	1.15	0.71	0.81	62 ± 25	1.14	0.69	0.90	61 ± 14
S12	1.55	0.76	0.74	91 ± 11	1.27	0.73	0.83	95 ± 9

2.4. Discussion

2.4.1. Advantages of our method

In this paper, we propose a new method to measure μ_{static} at the fingertip-object contact. Our method allows μ_{static} to be measured quickly and accounts for the effect of the normal force (NF), which has already been highlighted by several previous studies (Adams et al., 2007; André et al., 2009; van Kuilenburg et al., 2013). During dexterous object manipulation, inertial forces can significantly influence the tangential force at the fingertip-object interface, hence affecting the minimum normal force that would prevent object drop and therefore the safety margin. Accordingly, it is important to measure μ_{static} for several normal forces before manipulation to estimate the safety margin continuously during manipulation.

Our method is applicable to subjects exhibiting skin moisture levels spanning the whole range of moisture measurable with the Corneometer (cf. skin moisture measurements in Table 2.1). It is also applicable to one or several fingers, provided that there is a single six-axis force and torque sensor dedicated to each finger contacting the object. Results obtained with this method are reproducible. Therefore, the relationship between μ_{static} and NF for a given subject can be measured before an experimental session and used during the entire subsequent session. Consequently, the experimenter can continuously estimate the minimum NF that would prevent slippage and thus continuously estimate the safety margin (i.e., the difference between the actual and minimum NF) during a dexterous manipulation experiment. Finally, this method works with normal forces spanning the whole range of forces used in tactile exploration (Klöcker et al., 2013; Smith et al., 2002) and dexterous object manipulation (Augurelle et al., 2003; Edin et al., 1992; Johansson and Flanagan, 2009; Johansson and Westling, 1984), namely from 0.5N to above 8N. André et al. reported that the fingertip skin μ_{static} becomes constant for NF values above 5N (André et al., 2009). Given these advantages, our method is well suited for studies involving tactile exploration or dexterous object manipulation.

2.4.2. Comparison with previous methods

Our method only necessitates a single six-axis force and torque sensor to acquire data for different values of normal force. In comparison, several other methods used more complicated apparatuses (André et al., 2009; Fagiani et al., 2012; Han et al., 1996; Savescu et al., 2008; Seo and Armstrong, 2009).

Our method overcomes several limitations of the classical μ_{static} measurement method introduced by Westling and Johansson (Westling and Johansson, 1984), in which subjects slowly release their grip until dropping the manipulandum. First, our method accounts for the dependence of μ_{static} on NF with no change in the apparatus, thereby allowing continuous estimation of the safety margin. Second, the intrinsic variability of the measurements is not a problem in our method, which is able to acquire numerous measurements rapidly, thereby reducing measurement error. Finally, our method does not require subjects to lift an object or release their grip slowly until the manipulandum is dropped. As a result, our method is easier to use for patients with motor impairments.

2.4.3. Limitations of our method

In addition to the aforementioned advantages, our method also has some limitations. First, our method requires that the material covering the force sensors exhibits a higher static than dynamic frictional coefficient. This is because the tangential force needs to decrease when the fingertip begins to slip, in order for our algorithm to detect slip onsets correctly.

The second limitation regards the moisture level of the subject's fingertip. Variations in fingertip skin moisture during object manipulation (André et al., 2010) and across subjects (Tomlinson et al., 2011) have been shown to impact μ_{static} (André et al., 2009; Tomlinson et al., 2011). In this study, we measured the average moisture level of subjects' fingertips. Some of the variability in our data might be explained by the variation in moisture levels across individual measurements. This is a possible explanation for the higher variability of μ_{static} exhibited by subject S06 in Fig. 2.3. We advise researchers to measure μ_{static} frequently and, if possible, to measure the fingertip moisture of each subject before and at different times during each data acquisition session.

Finally, our method was designed to measure the static coefficient of friction (i.e., at slip onset). Adapting our method to measure the dynamic coefficient of friction (i.e., during slippage) would require a complementary study. The latter measurement is not straightforward because the dynamic coefficient of friction depends on many factors, including the slipping speed and normal force (Pasumarty et al., 2011).

2.4.4. Validity of the negative power law

To capture the relationship between μ_{static} and NF, we used a negative power function that has been used in previous studies (Adams et al., 2013; André et al., 2009; Wolfram, 1983). Reference (Adams et al., 2007) indicated that the parameter n must lie between 2/3 and 1, which was most often the case in our data (Table 2.1). The case where n = 2/3 corresponds to a purely Hertzian contact. When n = 1, the model simplifies to μ_{static} = k (constant). This case is equivalent to Amontons' law, which states that the friction force (TF) is proportional to the normal force (NF). As n < 1 for all subjects (Table 2.1), Amontons' law cannot be considered as valid for the fingertip-object contact at low normal force (< 5 N). Our model better describes the reality in this case.

2.4.5. Influence of tangential force rates

As previously stated, the inertial component of tangential force in dexterous object manipulation can vary significantly due to object's acceleration. In this study, we observed the tangential force rates during measurement of the relationship between μ_{static} and NF to be below 60N/s. When tangential force rates during object manipulation are comparable to those applied during measurement, the measured relationship between μ_{static} and NF can be used to predict μ_{static} during object manipulation. By inspecting typical traces in previous studies, we found tangential force rates to be around 50N/s for point-to-point movements (Flanagan and Wing, 1993) and around 10N/s for oscillatory movements (Augurelle et al., 2003). However, some tasks involve large levels of acceleration and therefore rapid variation of tangential forces, e.g. collision tasks where force rates can be above 500N/s (White et al., 2011). In this case, when tangential force rates are larger than the ones applied during measurement, the non-linear, visco-elastic properties of the fingertip skin might make the measured relationship between μ_{static} and NF invalid. This limitation is worth investigating in future studies.

2.5. Conclusion

Our method enables μ_{static} at the fingertip-object contact to be measured easily by using a six-axis force and torque sensor, while accounting for the dependence of μ_{static} on the normal force. Using our method, it is possible to estimate μ_{static} continuously and quickly during object manipulation and tactile exploration, provided that the material covering the force sensor exhibits a higher static than dynamic frictional coefficient. Under the assumption that the fingertip moisture level is constant, μ_{static} measured at the beginning of an experimental session remains valid during the course of the experimental session. Finally, the continuous estimation of μ_{static} during object manipulation enables continuous monitoring of the minimum NF to prevent object drop and, accordingly, of the safety margin (i.e., the difference between the actual and minimum NF values).

2.6. Supplemental material

Fit parameters from Table 2.1 were plotted as a function of mean fingertip moisture for each of the twelve subjects (Fig. 2.S1). No significant relationship was found between the fit parameters and the fingertip moisture level.

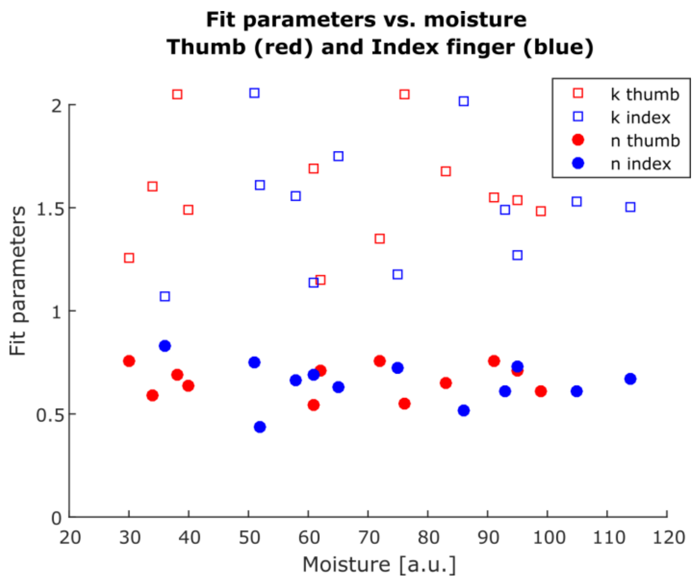

Fig. 2.S1. Fit parameters k and n vs. fingertip moisture. Fit parameters from Table 2.1 plotted against the corresponding fingertip moisture: k (open squares) and n (solid circles). Parameters were plotted separately for the thumb (red) and for the index finger (blue).

CHAPTER 3

Perception of partial slips under tangential loading of the fingertip

"Getting lost opens new horizons."

J. Edward Colgate (IEEE World Haptics Conference 2017)

During tactile exploration, partial slips occur systematically at the periphery of fingertip-object contact prior to full slip. Although the mechanics of partial slips is well characterized, the perception of such events is unclear. Here, we performed psychophysical experiments to assess partial slip detection ability on smooth transparent surfaces. In these experiments, the index fingertip of human subjects was stroked passively by a smooth, transparent glass plate while we imaged the contact slipping against the glass. We found that subjects were able to detect fingertip slip before full slip occurred when, on average, only 48% of the contact area was slipping. Additionally, we showed that partial slips and plate displacement permitted slip detection, but that the subjects could not rely on tangential force to detect slipping of the plate. Finally, we observed that a low level of contact friction impeded slip detection. Together, these results demonstrate that partial slips play an important role in fingertip slip detection and support the hypothesis that the central nervous system relies on them to adjust grip force during object manipulation.

3.1. Introduction

Our tactile sense provides a wealth of information about our environment. Stroking our fingertips over a surface allows us to perceive many physical properties, including texture (Hollins and Risner, 2000), relative speed between the fingertip and the surface (Dallmann et al., 2015; Salada et al., 2004), friction (Smith and Scott, 1996), and submicron-scale features (Gueorguiev et al., 2016; Skedung et al., 2013). Thus, mechanical interactions between finger pads and the surfaces they contact play a critical role in tactile perception.

When a fingertip is loaded tangentially against a surface, slippage occurs progressively with a very reproducible two-phase pattern. In the first phase, called incipient slip, slippage occurs at the periphery of contact. The no-slip area in the center of the contact area decreases gradually with increasing loading until gross slippage occurs. In the second phase, called full slip, the entire contact area slips. The biomechanics of the partial slip phenomenon has been described thoroughly *in vivo* in passive conditions (André et al., 2011; Delhaye et al., 2014, 2016; Tada and Kanade, 2004; Tada et al., 2006) and modelled mathematically within the framework of contact mechanics for an ideal elastic sphere (Johnson, 1985). Although a fingertip is not an ideal elastic sphere, the model predictions were qualitatively confirmed *in vivo* (Delhaye et al., 2014, 2016).

Stick ratio (SR) was proposed to quantify partial slip at the fingertip contact (André et al., 2011; Tada et al., 2006). SR is defined as the ratio of the no-slip area to the entire contact area. SR falls progressively from 1 (no slip) to 0 (full slip) as partial slip develops within the contact, starting from the periphery of the contact and propagating towards its center until there is a full slip.

Srinivasan et al. demonstrated the capacity of tactile afferents to encode stimulus features related to fingertip slip (Srinivasan et al., 1990). They performed psychophysical experiments wherein human subjects detected the relative motion (i.e. slip) of plates stroked under their fingertip. In addition, they recorded the responses evoked in tactile afferent fibers of macaque monkeys exposed to the same paradigm. The human subjects detected loading direction but not slippage of a smooth glass plate. Importantly, the plate was pressed against the fingertip with a very low normal force (NF), inducing very little fingertip deformation. However, when micrometer-sized protrusions were added to the glass, subjects were able to detect the plate slipping. The firing rate of rapidly adapting afferent fibers innervating the hand of monkeys increased when they were exposed to the non-smooth plates. The authors concluded that surface protrusion-induced vibrations generated in the skin by the non-smooth plates caused the increased firing rate, which in turn helped the central nervous system detect slippage. Similarly, Johansson and Westling had demonstrated previously that rapidly adapting afferent fibers are responsive to fingertip slip during object grasping (Johansson and Westling, 1987).

To our knowledge, no prior study has examined the perception of fingertip slip while simultaneously imaging incipient slip and measuring fingertip contact dynamics. Here, we conducted two psychophysical experiments in which the right index fingertip of human subjects was stroked passively with a speed of 5mm/s by a smooth, transparent glass plate in successive trials (Fig. 3.1A–B). After each trial, we asked the subjects whether they felt the plate slip under their fingertip or not. At the same time, we quantified the amount of partial slip taking place between the fingertip and the plate by imaging the finger pad through the transparent plate (Fig. 3.1C). Plate displacement was varied randomly across trials and ranged between a small displacement corresponding to almost no slip to a large displacement bringing the fingertip contact close to full slip. In the first experiment, we contrasted two levels of NF (2N vs. 5N) and in the second one, we contrasted two levels of friction (high vs. low). The experimental conditions are summarized in Fig. 3.1D.

We interpreted subjects' responses against three different predictors: plate displacement (PD), stick ratio (SR), and tangential force (TF) applied to the plate by the fingertip. Psychometric curves were fitted on subjects' answers, allowing us to extract the slip detection threshold for each one of the three predictors. Each threshold was defined as the value of the corresponding predictor for which the subject felt the plate slip 50% of the time. To determine which predictor underlay slip detection, thresholds were compared across experimental conditions. If the threshold was consistent across conditions, then we inferred that the predictor was reliable for slip detection. In contrast, if the threshold differed significantly across conditions, then we inferred that the predictor was ambiguous and not a useful cue for slip detection.

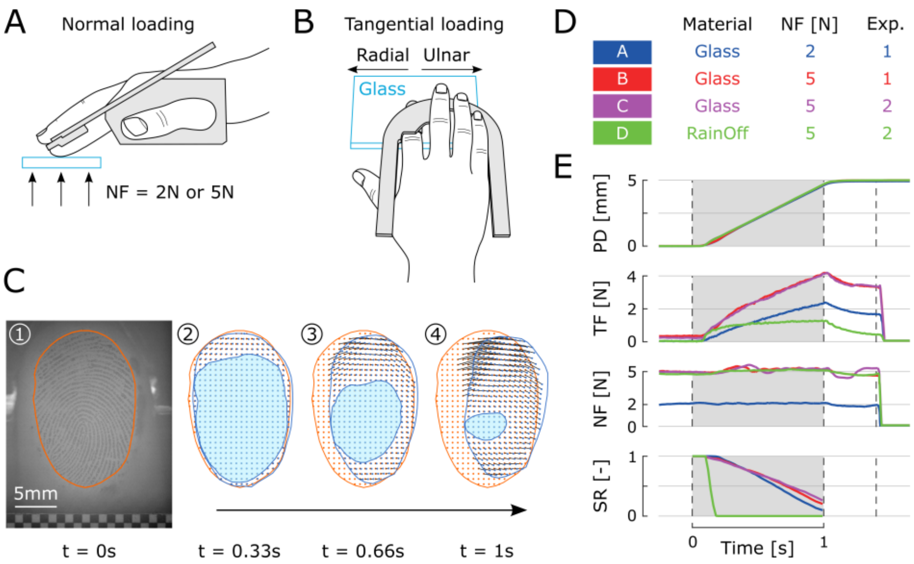

Fig. 3.1. Apparatus, experimental conditions and typical traces. (A) The right index fingertip of the subject (side view) is kept in place with a rigid support (in grey). A glass plate (blue) is pressed vertically against it with a controlled NF of 2N or 5N. **(B)** The glass plate is then moved horizontally with a speed of 5mm/s in the radial or ulnar direction before retracting from the fingertip (top view). **(C.1)** Typical fingerprint image acquired with the imaging system composed of a coaxial light source and camera. The orange contour delimits the contact between the fingertip and the plate. **(C.2–C.4)** Illustration of finger pad deformation under ulnar loading at constant speed (5mm/s) over a distance of 5mm with NF = 2N (corresponding to blue curves in panel E). The orange contour is the initial contact area reproduced from subpanel C.1. The blue contour is the contact area imaged at different times. The no-slip area (light blue) decreases with increasing tangential loading, while the periphery of the contact area experiences slippage. Orange dots sampled regularly in the initial contact area are linked with black lines to corresponding blue dots in the contact area under loading. **(D)** Summary of experimental conditions. Two stimuli were used: a bare glass plate ("Glass") and a glass plate covered with a hydrophobic solution strongly reducing the surface-skin friction ("RainOff"). **(E)** Typical traces from subject S01 with a total displacement of 5mm in the ulnar direction: plate displacement (PD), tangential force (TF), normal force (NF) and stick ratio (SR). The grey window represents the time period during which the robot was receiving a tangential displacement command and fingerprint images were recorded. Colors correspond to experimental conditions described in panel D.

3.2. Results

3.2.1. Experiment 1: NF contrast

The first experiment contrasted two NF levels: 2N vs. 5N. Fig. 3.2A presents the responses of three typical subjects. Data are presented from stick to slip and are therefore plotted against 1 – SR. This quantity monotonically increases from 0 to 1 between full stick and full slip and thus represents the actual slippage level between the fingertip and the plate. The subjects perceived fingertip slip before the actual full slip, i.e. before SR = 0, consistently under both the 2N and 5N NF conditions. The average slip detection threshold across all participants in the two conditions corresponded to a SR of 0.52 (95% confidence interval (CI) = [0.4 ; 0.64]). The detection thresholds from Fig. 3.2A are summarized in Fig. 3.2B for all subjects; no significant difference was found between the two NF conditions (paired t-test, $t(9) = 2.12$, $p > 0.05$). Similarly, PD threshold did not differ between the two NF conditions (paired t-test, $t(9) = 1.52$, $p > 0.05$; Fig. 3.2C–D). The average slip detection threshold across all participants in the two NF conditions corresponded to a PD of 2.26mm (95% CI = [1.92 ; 2.62]). For TF (Fig. 3.2E–F), detection thresholds differed significantly across the two NF conditions (paired t-test, $t(9) = 15.76$, $p < 0.001$), indicating that subjects could not rely on TF to detect fingertip slip. In contrast, the threshold invariance for SR and PD suggests that subjects could rely on at least one of these predictors or a combination of both to perceive fingertip slip.

Trials were performed randomly in the ulnar or radial direction (see Methods), with an equal total number of trials in each direction, in order to prevent stimulus habituation. There was no effect of stimulation direction on subject responses (Kolmogorov-Smirnov test on individual subjects' answers, $p > 0.05$).

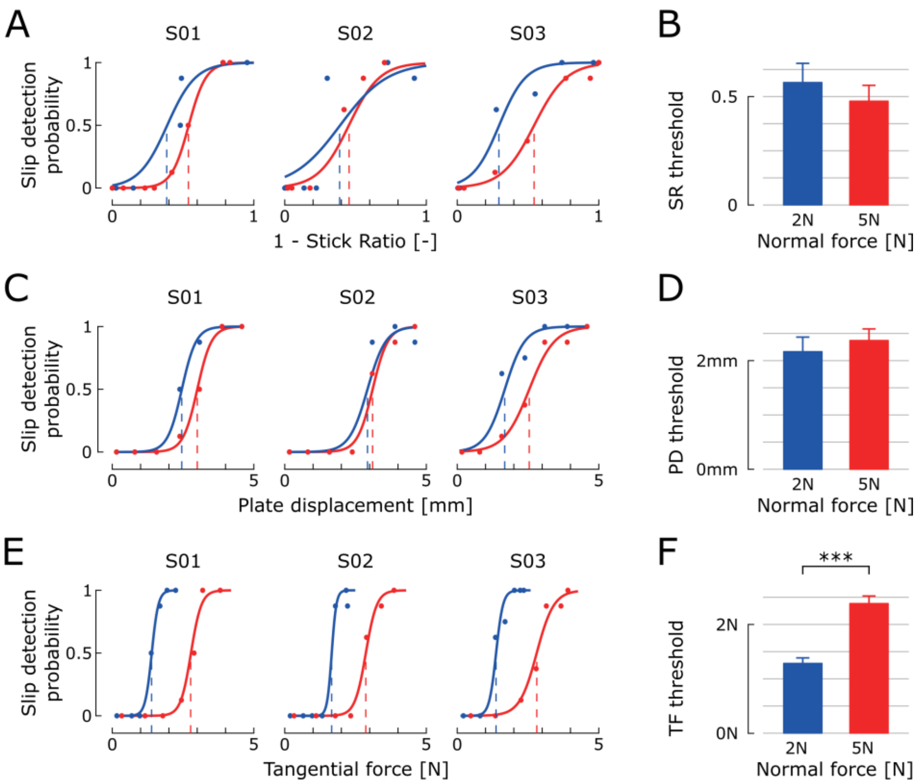

Fig. 3.2. Experiment 1: Slip detection thresholds on bare glass with two NF levels. Subjects detected fingertip slip before full slip and could not rely on TF to detect slip. Slip detection responses from three typical subjects are plotted against 1 – SR, PD, and TF in panels A, C, and E, respectively. Psychometric curves were fitted on subjects' answers from the two experimental conditions (NF = 2N, blue, vs. 5N, red), which allowed computation of slip detection thresholds, i.e. predictor values corresponding to a 50% probability of slip detection. Thresholds from all subjects were compared between the two conditions in panels B, D, and F for SR, PD, and TF, respectively. Bar charts summarize the thresholds in each condition as means ± standard errors across subjects. Remarkably, subjects detected slip before full slip in both conditions. Slip detection thresholds for TF, but not for PD and SR, varied across conditions, indicating that TF was unreliable for slip detection. For readability, subjects' answers are plotted against 1 – SR in panel A, such that increasing values on the x-axis correspond to greater partial slip. In panels A, C, and E, the coordinates of blue and red dots were computed as the average of all trials with the same PD within a given condition. They are displayed for illustrative purposes only; psychometric curves were fitted on data from individual trials.

3.2.2. Experiment 2: Friction contrast

In the second experiment, two friction conditions were contrasted: a high-friction condition using bare glass as in Experiment 1, and a low-friction condition, obtained by covering the glass plate with RainOff. In both conditions, NF was kept constant at 5N for all trials. In the high-friction condition, we reproduced results from Experiment 1: subjects perceived fingertip slip during incipient slip (SR > 0). However, in the low-friction condition, most subjects reported that they did not perceive the plate slipping under their fingertip. Green traces in Fig. 3.3A show the answers from three subjects plotted against PD in the low-friction condition. In this condition, stick-to-slip transition was abrupt and SR reached zero for PD < 1mm (see control experiment). Therefore, the plate was fully slipping under the subjects' fingertip in most of the low-friction trials. In spite of this, subjects often failed to detect the plate slipping, e.g. S02 in Fig. 3.3A. This was confirmed by the subjects' responses in full-slip catch trials (Fig. 3.3B) wherein the large PD (14mm) always yielded a full slip between the fingertip and the plate. In full-slip catch trials performed on bare glass (high friction), subjects were able to detect slippage of the plate with more than 95% accuracy (Fig. 3.3B, purple). However, this ability was dramatically impaired and their detection accuracy dropped to 47% in the low-friction (RainOff) condition (Fig. 3.3B, green). Subject responses in full-slip catch trials differed significantly across the two conditions (paired t-test, $t(5) = 2.79$, $p < 0.05$). Catch trial responses are further described in the Supplemental Material.

3.2.3. Control experiment

A control experiment was carried out to compare finger pad mechanics across experimental conditions to investigate why subjects could detect slip in the high-friction condition but not in the low-friction one. We included an additional very-low NF bare glass condition (NF = 0.5N) to investigate the mechanical behavior of the finger pad in conditions similar to those employed by Srinivasan et al. (Srinivasan et al., 1990). For all trials, a large PD (9mm) was used, sufficient to cause full slip and to allow TF to plateau. We measured the evolution of TF and SR as a function of PD (Fig. 3.4A–B) and measured the dynamic coefficient of friction between the fingertip and the plate in the four experimental conditions (Fig. 3.4C). A significant effect of experimental condition on the coefficient of friction was observed (one-way repeated-measures analysis of variance (ANOVA), $F(3,15) = 109.27$, $p < 0.001$), with significant differences in friction being observed among all four conditions (Bonferroni-corrected pairwise comparisons, $p < 0.001$).

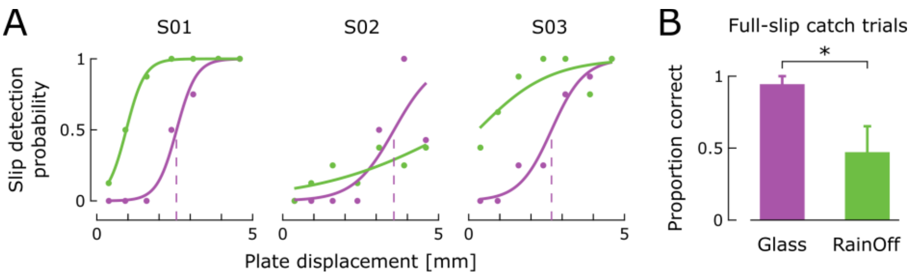

Fig. 3.3. Experiment 2: Impaired slip detection in the low-friction condition. (A) Answers from three typical subjects plotted against PD for the high- (purple) and low- (green) friction conditions. Subjects perceived fingertip slip consistently in the high-friction condition but not in the low-friction one. Purple and green dots correspond to the average of all trials sharing the same PD within the corresponding condition. They are displayed for illustrative purposes only; psychometric curves were fitted on data from individual trials. **(B)** Results from full-slip catch trials. Bar graphs summarize the ability of subjects to detect fingertip slip when the plate was fully slipping under their fingertip. Data are displayed as the mean proportion of correct answers ± standard error across subjects. In the high-friction condition (glass), subjects' performance was above 95%. In contrast, detection accuracy decreased to 47% in the low-friction condition (RainOff).

In the low-friction (RainOff) condition, TF plateaued earlier than in the high-friction (bare glass) conditions (Fig. 3.4A), indicating that fingertip shearing was reduced in this condition. In addition, the lower friction made SR reach zero, i.e. the fingertip was fully slipping, for PD < 1mm whereas the contact entered full slip for PD > 3mm in high-friction conditions (Fig. 3.4B). Besides, in the very-low NF condition (0.5N), TF and therefore fingertip shearing were lower than in the low-friction (RainOff) condition (Fig. 3.4A). However, the relationship between SR and PD was not dramatically affected by the reduction in NF and remained similar to that observed in other bare-glass conditions (Fig. 3.4B).

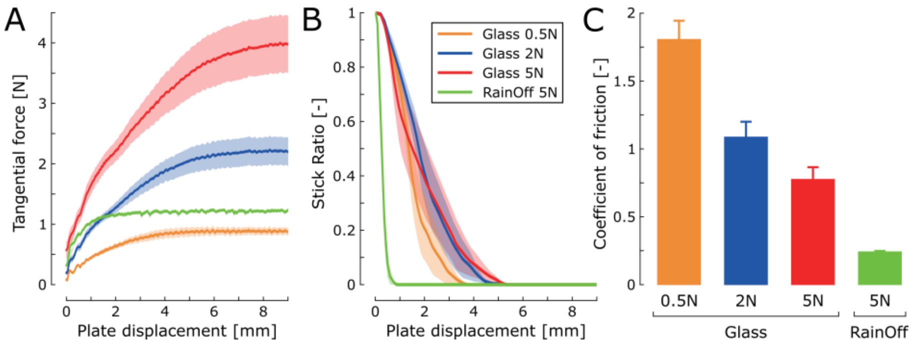

Fig. 3.4. Control experiment testing finger pad mechanics. (A) TF and **(B)** SR plotted against PD for the following conditions: bare glass with a NF of 0.5N (orange), 2N (blue), and 5N (red), and RainOff-covered glass with a NF of 5N (green). Data are displayed as mean ± standard error across subjects. **(C)** Mean dynamic coefficient of friction ± standard error across subjects. Friction differed among all conditions ($p < 0.001$).

3.3. Discussion

In this study, we investigated how humans perceive slippage of their fingertip under tangential loading. In two experiments, the index fingertip of subjects was stroked passively by a smooth glass plate, while the evolution of slip at the contact between the fingertip and the plate was imaged through the transparent glass. We measured the subjective threshold of slip detection as a function of several predictors: stick ratio (SR), plate displacement (PD), and tangential force (TF) applied to the plate by the fingertip. We found that subjects perceived slippage of a bare glass plate stroking their fingertip well before full slip, and that they could do so by relying either on the extent of partial slip under their fingertip, as measured with SR, or on PD, or on a combination of both. In addition, TF was found not to be a reliable predictor of slippage. Moreover, the subjects were unable to detect the plate slipping under low contact friction, even though NF was the same as with the bare glass plate. Finally, the reduction of contact friction also reduced the extent of fingertip deformation.

Previously, Srinivasan et al. reported that subjects did not detect slippage of a smooth glass plate pressed with a NF of 0.2N (Srinivasan et al., 1990), a force level that was an order of magnitude below those used in our study, therefore causing far less fingertip deformation, as demonstrated in our control experiment. Together, these results show that fingertip slip detection is impaired by either a low NF or a low contact friction. In addition, when subjects could not detect slippage of the smooth plate, fingertip deformation was lower than when they were able to detect it. Therefore, it seems that sufficient fingertip deformation is needed to detect slip on smooth surfaces.

In light of these observations, we propose that, in addition to the vibration-based mechanism allowing subjects to detect slippage of rough surfaces discussed by Srinivasan et al. (Srinivasan et al., 1990), there also exists a deformation-based mechanism enabling slip detection on smooth surfaces. Fingertip deformation is two-fold. On the one hand, the stroking plate causes fingertip shearing, i.e. volume deformations. As long as the finger is not slipping fully against the plate, these deformations are related to PD. On the other hand, fingertip skin in contact with the plate undergoes systematic surface deformations during fingertip shearing due to partial slips, as measured by SR (Delhaye et al., 2016). Therefore, we believe that PD and SR, which are respectively proxies of volume and surface deformations during incipient slip, both play a role in the hypothesized slip detection mechanism based on fingertip deformations. In addition, we hypothesize that the vibration- and deformation-based neural mechanisms are not mutually exclusive, but instead provide two complementary modes of detecting fingertip slips.

Besides, the fact that subjects perceived slip before full slip has functional implications for object manipulation. Indeed, this early slip detection may allow us to anticipate full slip and therefore to correct grip force before object dropping. It is therefore reasonable to hypothesize that a motor control mechanism could use partial slips to adjust grip force during object manipulation. Indeed, human manipulation abilities critically rely on tactile signals sent to the central nervous system by tactile afferents innervating the fingertips (Johansson and Flanagan, 2009). The lack of such feedback has a dramatic impact on manipulation performance and impedes our ability to adjust grip force in response to unexpected perturbations (Augurelle et al., 2003; Witney et al., 2004). Johansson and Westling reported automatic grip force adjustments in response to sudden accelerations attributed to brief slips between fingertips and an object (Johansson and Westling, 1984). In addition, they observed similar adjustments in the absence of an overall slip of the object. They hypothesized that these adjustments were triggered by partial slips, though they did not measure them directly (Johansson and Westling, 1987).

We intend to examine the partial-slip-based control mechanism with an instrumented manipulandum combining sensing of the forces applied by the fingers to the object and imaging of the fingertip contact, which would enable us to observe partial slips during dexterous manipulation and to determine how they may be involved in the adjustment of grip force. Interestingly, Ho and Hirai recently demonstrated the applicability of a partial-slip-based mechanism to control robotic grippers. They developed a robotic controller adjusting grip force based on the level of partial slip, and demonstrated with simulations that it was able to prevent full slip at the fingertip-object contact (Ho and Hirai, 2015). Their controller provides a robust and efficient grasping control by maintaining grip force just above the minimum level needed to avoid object dropping, similar to what is observed in human manipulation (Westling and Johansson, 1984).

To summarize, this study provides evidence that partial slips play a significant role in fingertip slip perception. In addition, it is reasonable and functionally relevant to hypothesize that the central nervous system could rely on partial slips to adjust grip force during object manipulation.

3.4. Methods

3.4.1. Participants

Ten healthy human subjects (age range 23–35 years; three women) participated in the first experiment. Six of them also participated in the second experiment and in the control experiment. All subjects provided written informed consent to undergo the procedure, which was approved by the ethics committee at the host institution (Institute of Neuroscience, Université catholique de Louvain, Brussels, Belgium). Participants were blindfolded during the procedure and there were no auditory cues that would allow them to perceive robot movements.

3.4.2. Apparatus and data collection

We used a robotic platform based on an industrial robot able to move plates in three orthogonal directions (Denso Robotics, Japan) to place a transparent glass plate in contact with the right index fingertip of subjects and to move it tangentially in the radial or ulnar direction (Fig. 3.1B). The surface of the glass plate was flat and smooth. The plate was cleaned manually with a microfiber cloth before every trial. For each trial, the glass plate was first loaded perpendicularly against the finger pad at a given NF, which was kept constant throughout the trial (Fig. 3.1A). Once NF stabilized, the plate moved tangentially over a given distance with a constant speed of 5mm/s. After a short pause, the plate was retracted from the finger pad. This robot was combined with a custom fingerprint imaging apparatus composed of a high-speed (50fps), high-resolution (1200dpi) camera and a coaxial light source. We used two force transducers mounted on each side of the glass plate to measure the forces applied to it by the subject's fingertip (ATI force sensors, ATI Industrial Automation, Apex, NC). The plate position and forces exerted on it were recorded at 1kHz. In addition, we imaged the fingerprints in contact with the transparent glass plate with the camera, which allowed us to compute the proportion of the contact slipping against the glass (Fig. 3.1C). The robotic platform and optical apparatus are described in greater detail elsewhere (Delhaye et al., 2014, 2016).

3.4.3. Experimental procedures

We conducted two psychophysical experiments with constant stimuli during which a glass plate was moved tangentially in the radial or ulnar direction under the right index fingertip of subjects in successive trials. At the end of each trial, subjects were asked to report whether they detected the plate slipping under their fingertip. The fact that subjects gave their answer after the end of the trial ensured that the results were not biased by reaction time. We tested seven PD levels, ranging linearly from 0.5mm to 5mm. The duration of the pause at the end of each trial was adjusted to ensure a constant period of 1.4s between the onset of the horizontal plate movement and plate unloading (Fig. 3.1E).

The first experiment consisted of two NF conditions (2N vs. 5N). Each stimulus was repeated eight times for a total of 112 trials per subject (2 NF levels x 7 PD levels x 8 repetitions). Trial presentation order was randomized. In addition to regular trials, catch trials were performed every eighth regular trial, for a total of 16 catch trials. These catch trials consisted of either no PD (4 trials), or 14-mm PD (12 trials), sufficiently large to ensure full slip between the fingertip and the plate. The total number of trials was thus 128 (112 regular trials + 16 catch trials). The duration of the full experiment was about 1.5 hour.

In the second experiment, two friction levels (high vs. low) were tested and NF was kept constant at 5N. In the high-friction condition, the same bare glass plate was used as in the first experiment. In the low-friction condition, the glass plate was covered with RainOff, a transparent hydrophobic coating that reduces the surface-skin friction strongly (Arexons, Italia). Without

RainOff, the dynamic coefficient of friction between the fingertip skin and the glass plate was close to 1, whereas with RainOff it decreased to 0.3. All trials from the high-friction (bare glass) condition preceded all trials from the low-friction (RainOff) condition because RainOff residue is difficult to remove from skin between trials. The number of trials was the same as in the first experiment (8 repetitions of 7 PD levels for 2 conditions = 112 regular trials, accompanied by 16 catch trials as described above, for a total of 128 trials).

3.4.4. Control experiment

The goal of this experiment was to characterize finger pad mechanics under the conditions tested in the two main experiments in order to investigate why subjects failed to detect fingertip slip in the low-friction condition of Experiment 2. The control experiment consisted of four mechanical conditions: bare glass with a NF of 0.5N, 2N, or 5N, and glass covered with RainOff with a NF of 5N. All other parameters were the same as in the main experiments, except for PD amplitude, which was increased to 9mm to allow TF to plateau in all conditions. Each condition was tested 5 times, totalizing 20 trials per subject. The results of this experiment depended only on finger pad biomechanics and were highly reproducible.

3.4.5. Data processing and statistical analyses

Position and force signals were low-pass filtered using a fourth-order, zero-phase-lag Butterworth filter with an 80Hz cut-off frequency. In the control experiment, we computed the friction coefficient as the TF:NF ratio during the TF plateau.

We tracked the position of fingerprint features in sequences of fingertip contact images and computed their displacement with respect to the glass surface. By spotting the features moving relative to the glass, we could measure the proportion of the fingertip-plate contact undergoing slippage and compute SR as the ratio of the no-slip area to the whole contact area between the fingertip and the plate. When slip occurs, SR falls progressively from 1 (no slip) to 0 (full slip) (André et al., 2011; Delhaye et al., 2014; Tada et al., 2006).

We modelled each subject’s responses using the psychometric function given in equation (3.1) (generalized linear model):

$$\Phi^{-1}[P(y_i = 1)] = \beta_0 + \beta_1 x_i \tag{3.1}$$

where Φ^{-1} is the probit link function, i.e. the inverse function of the cumulative Gaussian distribution, y_i is the binary response of the subject for the trial i (1 if slip perceived and 0 if not), $P(y_i = 1)$ is the slip detection probability, and x_i is the stimulus value at the end of the trial i. Three different predictors were considered: plate displacement (PD), stick ratio (SR) and tangential force (TF). Psychometric functions were fitted separately to the responses of each participant in each experimental condition and against the three predictors. From each model, we extracted the *slip detection threshold* as described in equation (3.2):

$$slip\ detection\ threshold = -\frac{\beta_0}{\beta_1} \tag{3.2}$$

This threshold represents the corresponding predictor value leading to a slip detection probability of 50%. This means that for predictor values larger than the threshold, subjects detected slip with a probability larger than chance.

Paired t-tests were carried out to detect differences in slip detection thresholds between pairs of experimental conditions. A one-way ANOVA with repeated measures was used to detect differences in friction between experimental conditions in the control experiment. Bonferroni-corrected paired t-tests were used to perform post-hoc multiple comparisons. The Kolmogorov-Smirnov test was used to test for an effect of stimulus direction on subject responses. P-values < 0.05 were considered significant. All data were processed and analyzed in MATLAB (The MathWorks Inc., Natick, MA) and R (R Project for Statistical Computing, https://www.R-project.org/).

3.5. Supplemental information

3.5.1. Catch trial responses

Full-slip catch trials consisted of a large plate displacement (14mm) guaranteeing full slip between the fingertip and the plate. Fig. 3.S1 presents responses of subjects to these catch trials. Subjects detected slipping in the two conditions of Experiment 1 and in the high-friction condition of Experiment 2, which were all performed on bare glass. However, in the low-friction (RainOff) condition of Experiment 2, performance was reduced dramatically and was close to 50%.

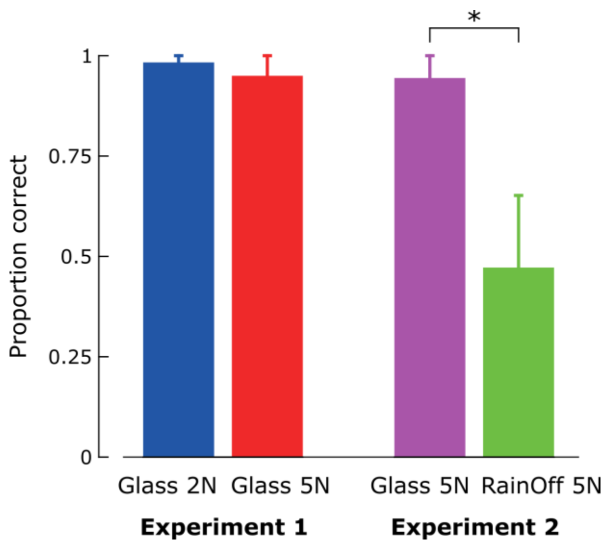

Fig. 3.S1. Full-slip catch trial responses. Proportions of correct answers are displayed as mean ± standard error for each condition. Subjects detected full slip between their fingertip and the plate in all conditions performed with the bare glass plate, but their performance was poor in the low-friction condition of Experiment 2, in which the plate was covered with RainOff. The asterisk denotes a significant reduction in the proportion of correct answers ($p < 0.05$).

3.5.2. Data from all subjects for Experiments 1 and 2

Slip detection data for all subjects are presented in Fig. 3.S2 for Experiment 1 and in Fig. 3.S3 for Experiment 2. These figures complement Fig. 3.2 and Fig. 3.3, respectively.

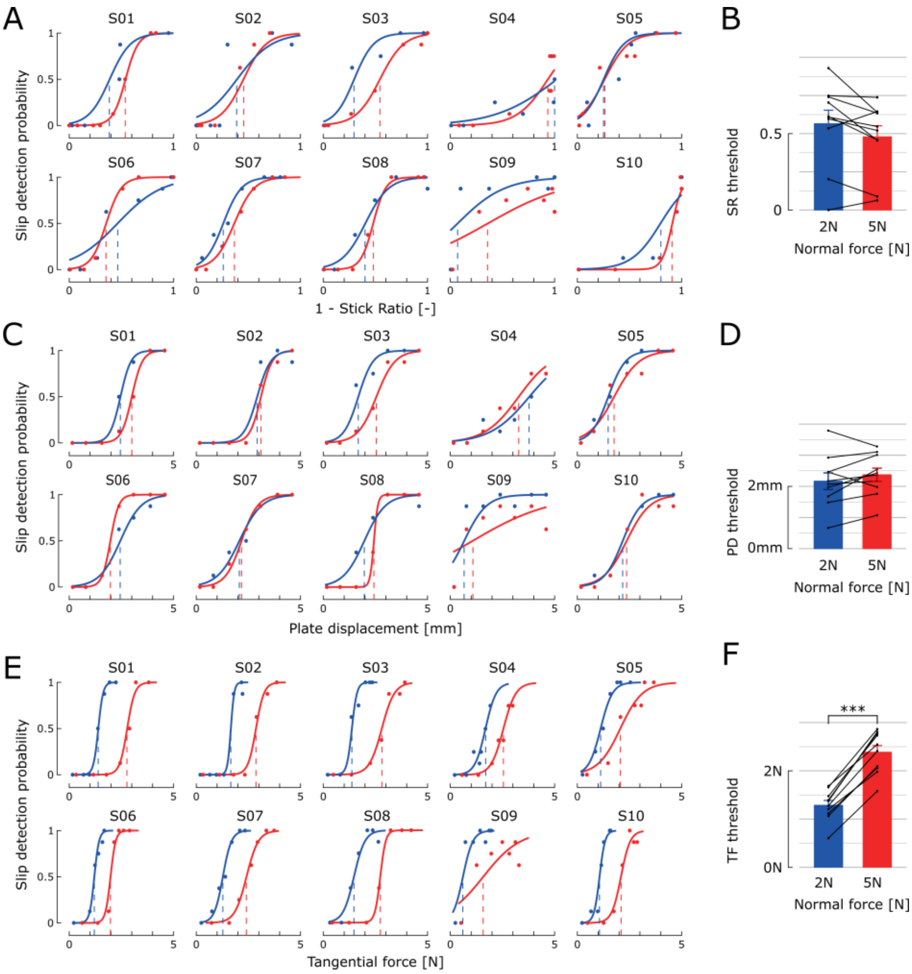

Fig. 3.S2. Data from all subjects for Experiment 1 (contrast in normal force). Please refer to the legend of Fig. 3.S2 for a detailed description of the presented data.

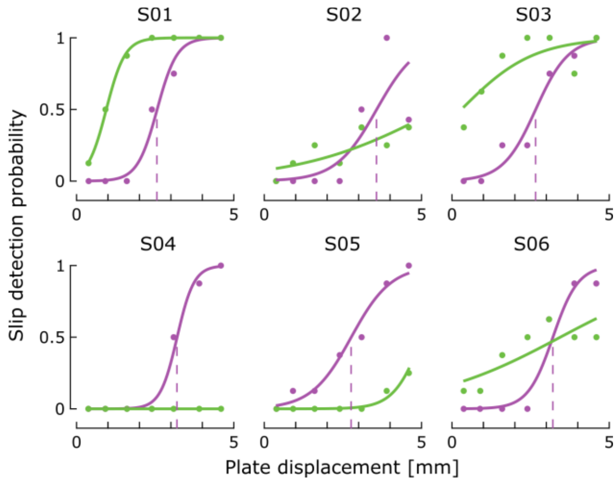

Fig. 3.S3. Data from all subjects for Experiment 2 (contrast in friction). Please refer to the legend of Fig. 3.S3 for a detailed description of the presented data.

3.5.3. Vibration analysis

We analyzed the vibrations produced during stimulation. We computed the Fourier transform of the unfiltered tangential force (TF) components recorded during the control experiment. We found differences across conditions in the frequency content of the force component aligned to the stimulus direction, i.e. the radial-ulnar direction, as presented in Fig. 3.S4.

This analysis shows that the amplitude of the vibrations was larger in conditions where TF was more important, i.e. for glass with NF = 2N and 5N. In these conditions, the fingertip also experienced more deformation, as testified by the results from the control experiment and especially Fig. 3.4.

In addition, for four of the six subjects (S01, S04, S05 and S06), a peak is observed around 250Hz, which corresponds to the peak sensitivity of the FA2 afferents, in glass conditions where NF = 0.5N and NF = 2N. Our results showed that subjects were able to detect slip in the latter condition (glass with NF = 2N). However, they were not likely to be able to detect slip in the former condition (glass with NF = 0.5N), as discussed in the main text. Moreover, the peak is absent in the condition where NF = 5N on glass, in which subjects were able to detect slip. Therefore, the role played by vibrations is not clear.

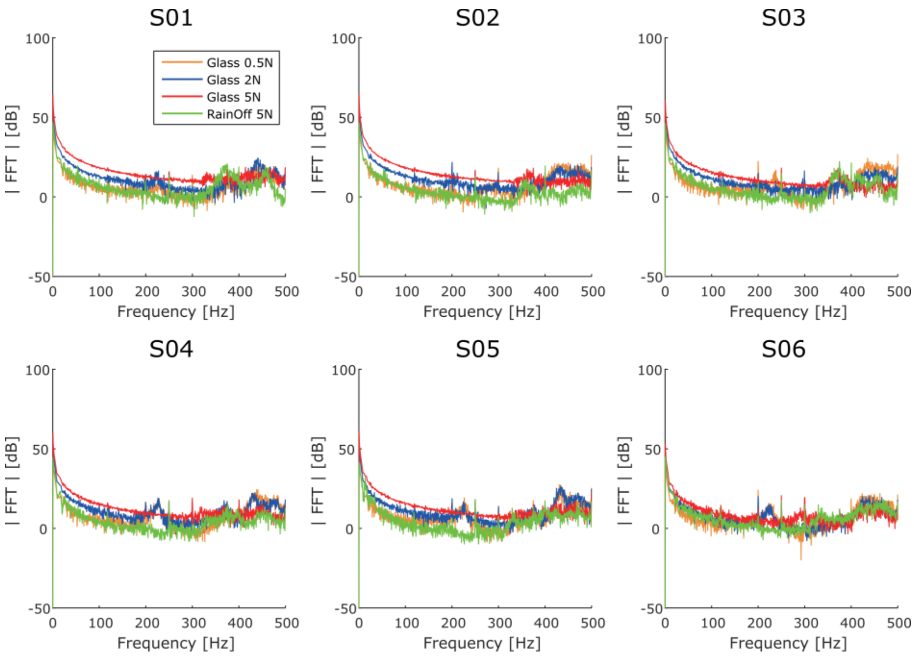

Fig. 3.S4. Stimulus vibration content during control experiment. Fast Fourier Transform (FFT) of the unfiltered tangential force in the direction of stimulation, i.e. along the radial-ulnar direction, for each of the six subjects in the control experiment and in the four tested conditions: glass with NF = 0.5N (orange), glass with NF = 2N (blue), glass with NF = 5N (red) and RainOff with NF = 5N (green). Data show average traces across the five repetitions in each condition.

In summary, this analysis does not bring a definitive answer to the question of the relative contribution of the vibrations vs. deformations to slip detection. We believe that deformations do play a role in slip detection and that deformations and vibrations are complementary for slip detection because they occur together during the transition from stick to slip. Further investigation is needed in order to gain a better understanding of the role of vibrations vs. deformations in slip detection.

CHAPTER 4

Finger pad mechanics during dexterous object manipulation

"Knowledge of what is possible is the beginning of happiness."

George Santayana

Humans are able to manipulate small objects with high dexterity. To achieve this, the central nervous system (CNS) critically relies on information coming from the numerous tactile afferents innervating the hand. Finger pad mechanics has been extensively studied in passive touch conditions, revealing that slips at the fingertip-object contact occur progressively, starting at the periphery of the contact and propagating towards its center until full slip. In Chapter 3, we showed that this partial slip phenomenon helped subjects anticipate full slip during tactile exploration. Given this observation and the importance of tactile feedback in object manipulation, it is reasonable to hypothesize that the CNS might rely on these partial slips to adjust the grip force exerted on the object. However, it is unclear how partial slips develop at the fingertip contact during manipulation. To examine this, we designed a manipulandum combining sensing of the forces applied by the fingers holding the object and imaging of the fingertip contact. This device will enable us to study the effect of fingertip contact dynamics on force control during manipulation. Here we describe the apparatus and present the results of a pilot study performed with it. Then, we discuss the research questions to be addressed with the device and its potential technical improvements.

4.1. Introduction

Humans are able to skillfully manipulate objects with their fingers by optimally adjusting their grip force to the object load (Flanagan and Wing, 1997; Westling and Johansson, 1984) and to the fingertip-object contact friction (Cadoret and Smith, 1996). Deformations and vibrations produced in the skin during object manipulation are faithfully captured by the numerous tactile afferents innervating the hand (Goodwin and Wheat, 2004), which in turn provide the central nervous system (CNS) with rich and behaviorally relevant information content. This allows the CNS to adjust the grip force exerted on a manipulated object to the grip conditions (Johansson and Flanagan, 2009). Without tactile feedback, the CNS fails to react to unexpected perturbations in object load (Nowak et al., 2001) and to maintain a stable grip force to load force ratio (Augurelle et al., 2003), hence highlighting the critical role played by tactile feedback during object manipulation (Witney et al., 2004).

In vivo biomechanics of the finger pad has been extensively studied in passive conditions, highlighting the systematic occurrence of partial slips at the periphery of the fingertip-object contact under tangential loading of the finger pad (André et al., 2011; Delhaye et al., 2014, 2016; Tada and Kanade, 2004; Tada et al., 2006). Besides, we demonstrated in Chapter 3 that human subjects are able to anticipate full slip of the fingertip contact. This has functional implications for object manipulation because this early slip detection would allow subjects to correct their grip force before the object falls off the hand. Therefore, it is reasonable to hypothesize that the CNS might rely on partial slips to adjust the grip during object manipulation.

It remains unclear, however, how much partial slip is present during object manipulation and how this will be affected by the grip conditions, including the biomechanical properties of the fingertips. Indeed, for a given object load, the amount of partial slip depends on how much grip force is exerted on the object and also on the frictional properties of the fingertip-object contact (André et al., 2011). To investigate this, we designed an instrumented object equipped with fingertip force sensing and fingertip contact imaging capabilities.

Here, we first describe the device and present the procedure used to measure partial slips at the fingertip contact from fingerprint images. Then, we present the results of a pilot study aiming at quantifying the amount of partial slips taking place at the fingertip contact during vertical rhythmic movements performed at several frequencies. Finally, we discuss the research questions to be investigated with the device and its potential technical improvements.

4.2. Apparatus

4.2.1. General description

Fig. 4.1 presents an overview of the manipulandum and its components. The object was designed to be manipulated in precision grip, i.e. pinched between the thumb and the index finger. Forces and torques are measured under each fingertip using two six-axis force and torque sensors (ATI Mini27 Ti, ATI-IA, Apex, NC, USA, resolution of 3/100N for forces and 3/8000Nm for torques). Following the convention introduced by Johansson & Westling (Johansson and Westling, 1984), the interaction force between each fingertip and the object was decomposed into two components acting normally and tangentially to the contact surface. The grip force (GF) was then defined as the mean normal force acting on both sensors. The load force (LF) was defined as the resultant force acting tangentially to both contact surfaces. Force definitions are illustrated in Fig. 4.1C. In addition to forces, the device is able to record accelerations up to ±6g along the three axes using a MEMS-based accelerometer placed on top of the device (LIS344ALH, STMicroelectronics, resolution of 1/1000G). Finally, the total mass of the manipulandum is 440g.

Fig. 4.2 illustrates how subjects hold the manipulandum in precision grip during experiments. They place their thumb and index finger on two transparent plates. The plates are quickly changed, allowing the experimenter to test materials exhibiting different friction properties during the same experiment.

In addition to fingertip force sensing, the manipulandum is also equipped with an optical system able to image the fingertip-plate contact. Several approaches based on the principle of frustrated total internal reflection (FTIR) exist to image finger contacts (Bochereau et al., 2017). On the one hand, systems using direct illumination produce high contrast images of the contact and allow a clear detection of the contact border. On the other hand, systems using an indirect illumination through the thickness of the transparent plate are more compact but produce less contrasted images with blurry contour of the contact. Because the contact border must be accurately detected when processing fingerprint images, we chose to use a system based on direct illumination. In addition, to keep a relatively small grip aperture and due to the size of the optical system based on direct illumination, we chose to image only one fingertip.

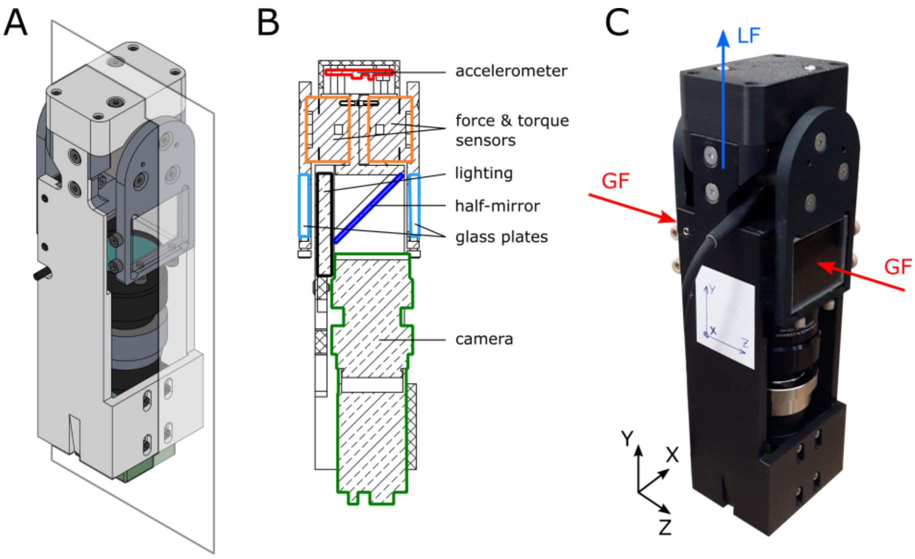

Fig. 4.1. Description of the ActiveTouch manipulandum. (A) CAD model. Dimensions of the device are 180x50x52mm with a grip aperture of 50mm. (B) Cut along the plane in panel A, revealing the key elements and sensors in the manipulandum. (C) Photograph of the actual manipulandum with definition of the reference frame and the grip and load force (GF and LF).

Fig. 4.2. Subject holding the manipulandum in precision grip during experiment. A transparent plate and a custom optical system allows imaging of the fingertip contact for one of the two fingers pressed against the object.

4.2.2. Fingertip contact imaging

Fig. 4.3 presents our custom optical system to image the fingerprints in contact with the transparent plate for one of the two fingers. The system is based on the principle of FTIR with direct illumination using a coaxial light source and camera. Images are recorded at a speed of 50 frames per second (fps). Image size is 1696 x 1248 pixels (px) with a resolution of 64px/mm, which corresponds to a region of 26.5 x 19.5mm.

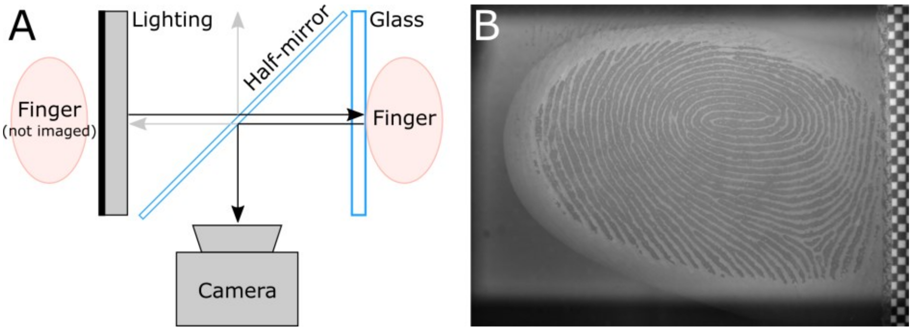

Fig. 4.3. Custom optical system to image fingerprints. (A) A half-mirror is used to align the light source and the axis of the camera. Arrows show the trajectory of light reflected at optical interfaces. Skin in contact with the glass diffracts the light, preventing it from reaching the camera. Fingerprints therefore appear darker on the images. (B) Example of fingertip contact imaged with the system. The pattern composed of small squares on the right of the image is used to measure the relative motion between the plate and the camera.

4.3. Image processing to measure partial slip and surface strains

Fingerprint images are processed to detect partial slips and measure surface strains in the finger contact. In this section, we describe the different stages of the analysis and illustrate them with data from vertical rhythmic movements performed during 4s with images acquired at 50fps. The level of partial slip in this illustrative dataset has voluntarily been exaggerated with respect to partial slip occurring during actual object manipulation that will be presented in the next section ("Pilot study"). Software tools developed to perform the analyses are briefly described in Appendix C.

4.3.1. Measuring partial slip

Fig. 4.4 summarizes the image processing workflow to compute partial slips from a sequence of fingerprint images. First, the contour of the contact area is detected automatically on all images. A dedicated image segmentation algorithm was developed for this task. This algorithm is described in Appendix C. After determination of the contact border, feature points are sampled within the contact in the initial frame of the sequence (Shi and Tomasi, 1994) and their position is tracked from frame to frame using optical flow (Bouguet, 2001; Lucas and Kanade, 1981). This process is described in further details in (Delhaye et al., 2014, 2016). Due to the rolling of the fingertip, some regions of the finger pad lose contact with the plate during manipulation, causing feature points to leave the contact. This is why it is important to detect the contour of the contact accurately before tracking feature points, in order to identify points leaving the contact and not consider them for further computations. Similarly, some regions of the finger pad come into contact with the plate during manipulation. To be able to track points in these regions as well, feature points are sampled in the last frame of the sequence and their position is tracked from frame to frame backwards in time. Then, both sets of feature points are merged together to build a complete picture of the local displacement of the fingerprints in contact with the plate.

In the same time, feature points are sampled and tracked on the reference pattern composed of black and white squares and attached to the plate (Fig. 4.3B). The trajectory of these reference feature points is used to measure the relative motion between the camera and the transparent plate. Indeed, we observed a small but significant displacement of the plate relative to the camera, predominantly in the vertical direction, i.e. in the direction of the rhythmic movements. The relative motion of the plate is computed as the median displacement of the reference feature points (Fig. 4.5A). This displacement is subtracted from the position of the feature points sampled in the contact area to compensate for plate motion.

The peak-to-peak amplitude of the plate displacement on the test data was at most 12 pixels, i.e. 0.19mm (Fig. 4.5A). The displacement followed the same pattern as the vertical component of the load force (LFv), but it was not correlated to the grip force (GF) (Fig. 4.5B). This indicates that the observed plate displacement corresponds to an actual vertical displacement of the plate, caused by LFv, and is not due to the bending of the plate, which would have been caused by GF. In addition, some jerky component was observed both in the plate displacement and in LFv. The Fast Fourier Transform (FFT) of LFv revealed two peaks (Fig. 4.5C): one sharp peak at low frequency due to the rhythmic movement and one peak at higher frequencies (around 20Hz) due to the mechanical noise generated by the pulleys in the weight compensation system (see Section 4 "Pilot study"). The jerky component observed in the plate displacement signal is therefore due to mechanical noise and not to noise in the tracking of the feature points, which was confirmed by direct observation of the images.

Next, the displacement field is computed from the trajectory of the feature points within the contact. This displacement field allows the contact regions slipping against the plate to be computed. Points whose displacement between two consecutive frames exceeds 1px, i.e. 0.016mm, are considered slipping relative to the plate and the others are considered stuck to the plate.

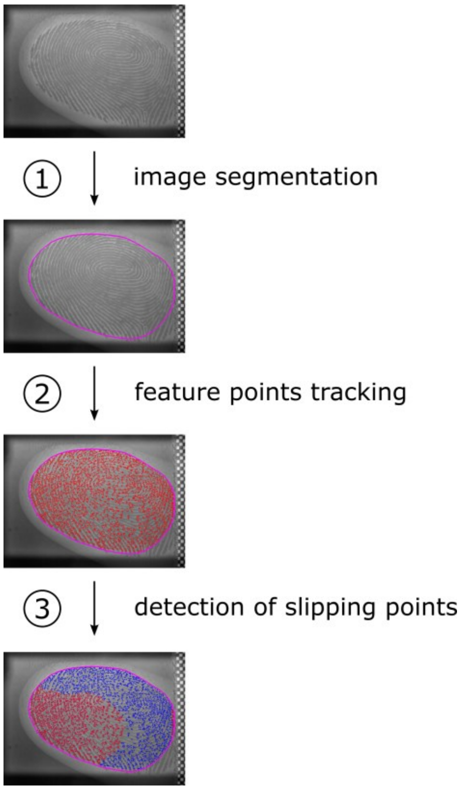

Fig. 4.4. Image processing workflow. The analysis workflow to measure partial slip between fingertip and object is composed of three major steps. First, the contour of the fingertip contact is segmented automatically. Then, feature points are sampled within the contact and tracked from frame to frame. Finally, contact regions slipping against the plate are computed from the local displacement of feature points. Contact contour is represented with the magenta line. Feature points are in red. Feature points slipping against the glass are in blue.

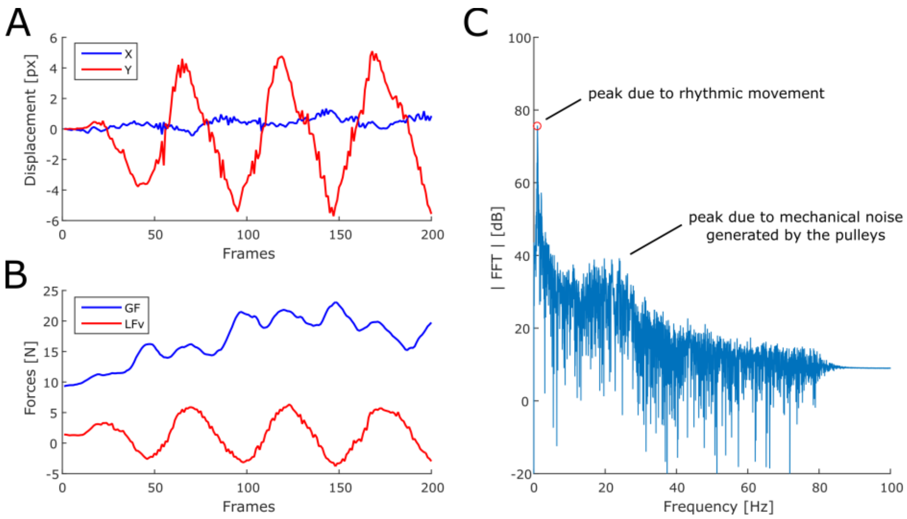

Fig. 4.5. Plate motion relative to the camera during manipulation. (A) Plate displacement relative to initial frame along the x-axis (blue) and y-axis (red), i.e. tangentially to the plate. Displacement was larger along the y-axis, which corresponds to the vertical direction. One pixel corresponds to 1/64mm, i.e. 0.016mm. Images were acquired at 50fps, thus 50 frames correspond to one second. **(B)** Grip force (GF, blue), exerted normally to the plate, and vertical load force (LFv, red), acting tangentially to the plate in the vertical direction. LFv is very similar to the plate displacement in the vertical direction in panel A. **(C)** Fast Fourier Transform (FFT) of LFv, highlighting the mechanical noise caused by the pulleys in the weight compensation system. A first sharp peak (red circle) is observed at low frequency and is due to the rhythmic movement. A second peak is observed at higher frequencies (around 20Hz) and is due to the pulleys.

To quantify the amount of partial slip taking place between the fingertip and the plate, the stick ratio (SR) has been proposed in previous work (André et al., 2011; Tada et al., 2006). SR is defined as the ratio of the no-slip area over the whole area of the fingertip contact. Here, SR is computed as the ratio of the number of non-slipping feature points between two consecutive frames versus the total number of feature points within the contact. This is a good estimation of the true value of SR given that feature points are sampled homogeneously within the contact. Fig. 4.6 presents SR computed on the test data with and without compensation for plate motion. When plate motion is not compensated for, many feature points are incorrectly considered slipping, therefore disrupting SR computation. Fig. 4.7 presents the slipping and non-slipping feature points within the contact for a sample of 20 frames from the test data. It can be observed that the no-slip area forms a single connected region. In a first phase, partial slips develops from the periphery towards the center of the contact, as observed in passive conditions (André et al., 2011; Delhaye et al., 2014; Tada et al., 2006). Then, in a second phase, the contact progressively goes back to a fully non-slipping state.

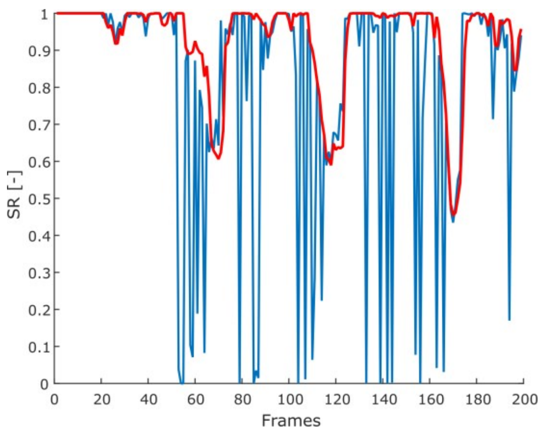

Fig. 4.6. Effect of plate motion on partial slip computation. Partial slip is measured with the stick ratio (SR), which is computed as the ratio of the non-slipping vs. total number of feature points within the contact. The blue line represents SR computed without compensating for plate motion. The movements of the plate cause an incorrect detection of the slipping points and therefore need to be compensated for. The red line represents SR computed after compensation for plate motion, which allows a more faithful detection of slipping points. Images were acquired at 50fps, thus 50 frames correspond to one second.

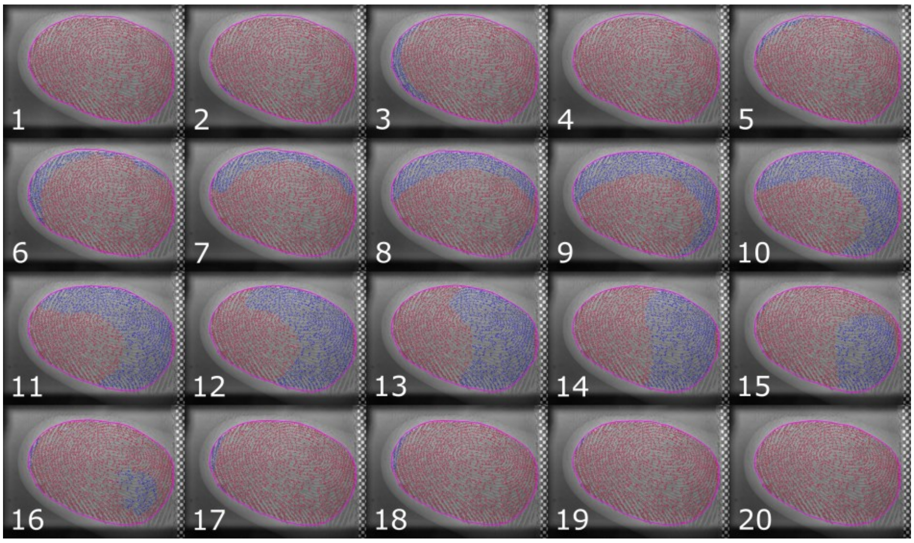

Fig. 4.7. Partial slip at the fingertip contact. Points slipping (blue) and not slipping (red) relative to the glass in a sequence of 20 images sampled every 20ms, corresponding to frames 160 to 179 of Fig. 4.6. In a first phase (images 1-10), the periphery of the contact starts slipping and partial slips propagates towards the center of the contact. In a second phase (images 11-20), the contact progressively goes back to fully non-slipping state.

4.3.2. Measuring surface strains[3]

Strains at the surface of the skin in contact with the plate are computed from the displacement field of the feature points. Because of the large deformations undergone by the skin, strains are computed based on the Green-Lagrange formulation. Figure 4.8 illustrates the computation. In practice, a Delaunay triangulation is computed on the feature points sampled in the first frame. For each triangle, the gradient of the displacement field is estimated from the displacement of its vertices. Then, strains are computed according to equation (4.1), where ε_{xx} and ε_{yy} are the axial strains aligned to the x and y axes, respectively, ε_{xy} is the shear strain, and u and v represent the displacement along the x and y axes, respectively. These strains are attributed to the center of each triangle (x_c,y_c). Strains represent a relative deformation. Axial strains are positive for dilation and negative for compression. Shearing strain is positive when the deformation causes the angle between the positive x and y axes to decrease and negative when the deformation causes this angle to increase.

$$\varepsilon_{xx} = \frac{\partial u}{\partial x} + \frac{1}{2}\left[\left(\frac{\partial u}{\partial x}\right)^2 + \left(\frac{\partial v}{\partial x}\right)^2\right] \tag{4.1a}$$

$$\varepsilon_{yy} = \frac{\partial v}{\partial y} + \frac{1}{2}\left[\left(\frac{\partial u}{\partial y}\right)^2 + \left(\frac{\partial v}{\partial y}\right)^2\right] \tag{4.1b}$$

$$\varepsilon_{xy} = \frac{1}{2}\left(\frac{\partial u}{\partial y} + \frac{\partial v}{\partial x}\right) + \frac{1}{2}\left(\frac{\partial u}{\partial x}\frac{\partial u}{\partial y} + \frac{\partial v}{\partial x}\frac{\partial v}{\partial y}\right) \tag{4.1c}$$

Strains computed following the procedure described above are actually strain *rates* because they result from the displacement between pairs of consecutive frames in the image sequence and not from the displacement relative to the initial frame. The total strains, representing the actual deformation of the finger pad relative to its initial state, are obtained by integrating the strain rates, i.e. summing their contributions over time.

Fig. 4.9 illustrates the strain rate along the vertical direction (i.e. ε_{yy}) computed in the same image sequence as in Fig. 4.7. The partial slip illustrated in Fig. 4.7 results in a wave of strain propagating from the periphery to the center of the contact in a first phase, then vanishing as the contact progressively sticks again to the plate in a second phase.

---

[3] Section adapted from Delhaye et al. (2016).

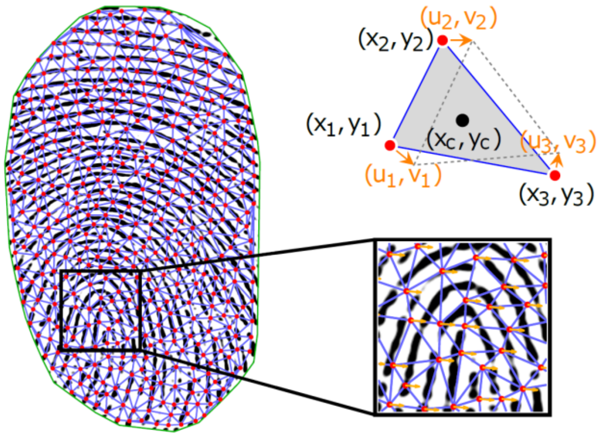

Fig. 4.8. Strains computation. Surface deformation of the fingertip skin is computed from local displacement of feature points. The green curve denotes the contour of the contact. Red dots are the feature points sampled within the contact. Orange arrows in the higher-resolution inset represent the displacement of the points computed via optical flow between two consecutive images. A Delaunay triangulation of the feature points is computed and represented by the blue segments. Strains are computed in each triangle from the gradient of the displacement of the vertices of the triangle. Strains computed in a given triangle are then attributed to the center of this triangle. Adapted from Delhaye et al. (2016).

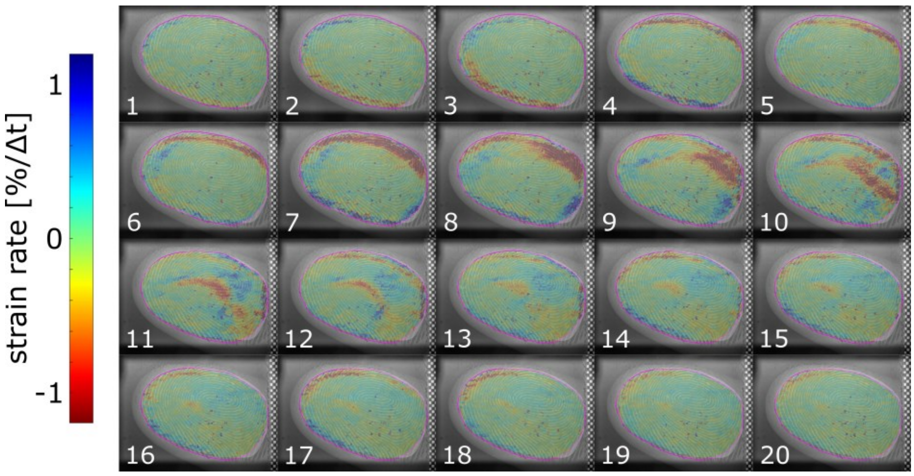

Fig. 4.9. Strains at the fingertip contact. Strains along the vertical direction were computed from local displacement of feature points on the same image sequence as in Fig. 4.7. This sequence illustrates the strain rate, i.e. the relative deformation between successive frames. The strain wave propagates from the periphery to the center of the contact and then vanishes as the contact sticks again to the plate. Local compression of the skin is displayed in red and local dilation in blue.

4.4. Pilot study

4.4.1. Protocol

A pilot study was conducted with one subject to investigate the presence of partial slips during object manipulation. The subject pinched the manipulandum between the thumb and index finger of his right hand and performed vertical rhythmic arm movements. Both fingers were in contact with identical smooth glass plates. The subject was instructed to move the manipulandum in continuous cyclic movements following the rhythm imposed by a metronome. The subject was free to select the movement amplitude that seemed the most natural to him in order to follow the rhythm of the metronome. Observed movement amplitudes ranged between 30cm and 40cm.

Six metronome frequencies were tested, starting at 60 beats per minute (bpm) until 135bpm with constant steps of 15bpm. The subject performed one complete cycle every two pulses of the metronome. Therefore, movements were performed at half the frequency imposed by the metronome. Three trials of 10s each were collected for each reference frequency, leading to a total of 18 trials.

The weight of the manipulandum was partially compensated with a counterweight because the manipulandum alone was too heavy (440g) to be manipulated easily at all the tested movement frequencies. The counterweight was attached to the manipulandum with a rope guided by pulleys so that both the manipulandum and the counterweight were moving along the vertical axis. The mass of the counterweight was 360g. The system formed by the device and the counterweight was thus equivalent to a mass of 800g in terms of inertia but with a weight of only 80g.

Forces and torques exerted by each fingertip on the device and the overall acceleration of the device were sampled at 200Hz. Images of the fingerprints of the right index finger in contact with the glass were acquired at 50fps. The glass was manually cleaned with a microfiber cloth before each trial.

4.4.2. Results

The subject was able to follow the rhythm imposed by the metronome with high accuracy. No significant deviation from the imposed frequency was observed (t-test on deviation from reference frequency for all trials, $t(17)$ =

1.23, p = 0.23). The mean deviation from the imposed frequency was 0.01Hz, with a standard deviation of 0.02Hz.

Fig. 4.10 presents typical traces from two trials performed with reference frequencies of 90bpm and 135bpm. Data were segmented at each extremum of the load force (LF). Images in each segment were processed separately. This way, it was possible to track feature points in the whole contact area despite the large rolling of the fingertip against the plate, which caused large regions of the finger pad to come into or lose contact with the plate during manipulation. Partial slip was summarized with the stick ratio (SR) and fingertip rolling was estimated from the trajectory of the center of pressure (COP), which is the location of the resultant force on the plate.

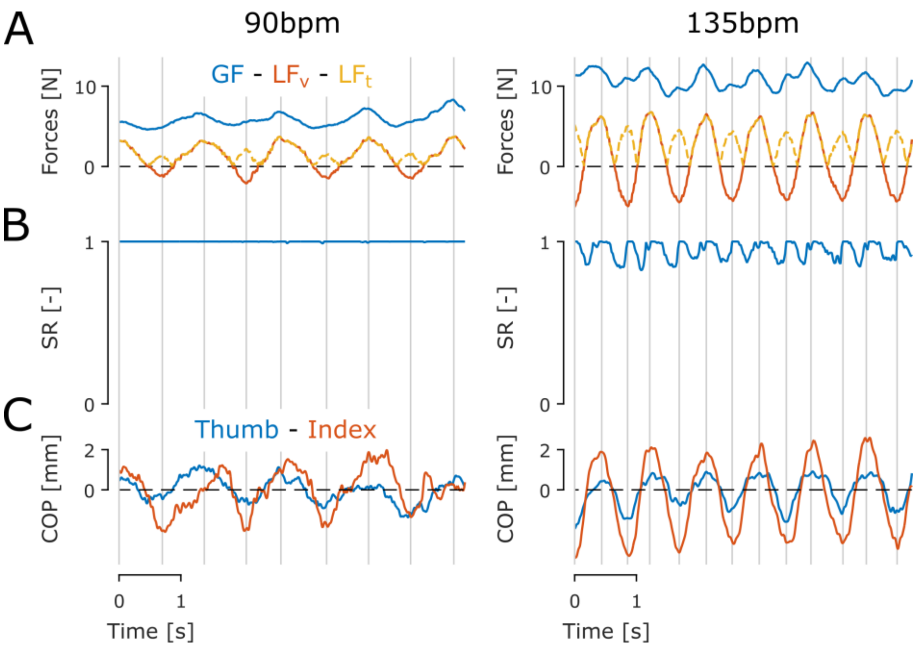

Fig. 4.10. Typical traces. Vertical rhythmic movements performed with reference frequencies of 90bpm (left) and 135bpm (right). (A) Forces measured during the trial. The solid blue line represents the grip force (GF). The solid red line is the vertical component of the load force (LFv) and the dashed yellow line is the norm of the total load force (LFt). The vertical gray lines determine the segments used during image analysis and are defined at extrema of the vertical load force. (B) Stick ratio (SR) measured during each trial, which is an image of partial slips taking place at the fingertip contact. (C) Vertical component of the center of pressure (COP) for the thumb (blue) and the index finger (red), which is a proxy to the rolling of the fingertip against the glass plate.

The amplitude of both the grip force (GF) and the vertical component of the load force (LFv) increased with movement frequency (Fig. 4.11A). Regression lines were fitted to the data using a least-squares procedure. Positive and negative values of LFv were considered separately for the regressions. The slopes were all significant ($p < 0.05$), indicating that GF was modulated with LFv. The offsets of the regressions but not the slope increased with movement frequency.

Partial slip within the index fingertip contact is illustrated in Fig. 4.11B–D, where colored traces correspond to the moments when SR was smaller than 0.99, 0.95, or 0.90, respectively, i.e. for increasing levels of partial slip within the contact. This shows that partial slip was higher for large absolute values of LFv and that it was present at small values of LFv for higher movement frequencies.

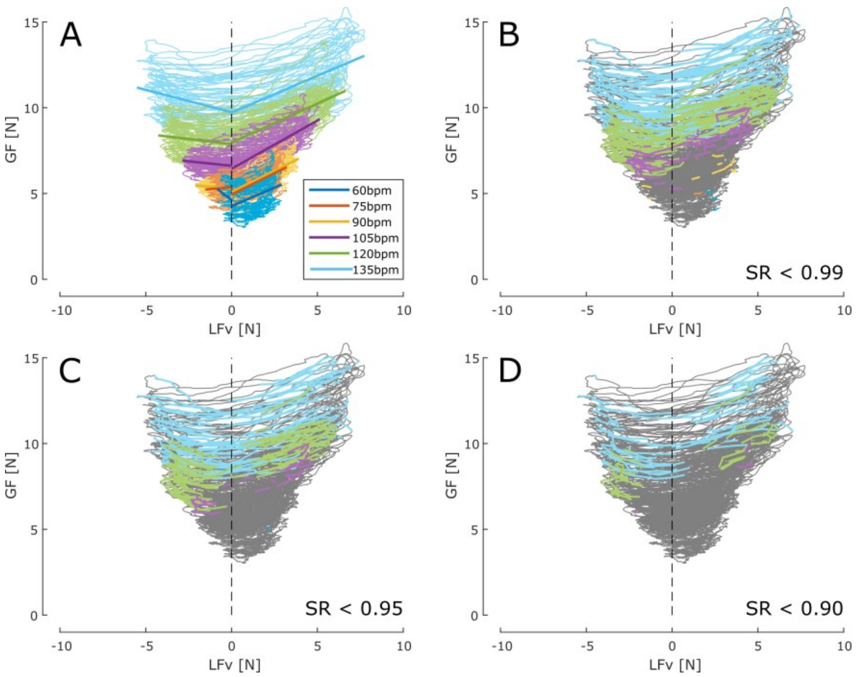

Fig. 4.11. Phase diagram. (A) Plot of grip force (GF) versus vertical component of load force (LFv). Data from all trials from the six conditions are represented in thin solid lines. Thick solid lines represent linear regressions performed on data for each condition, considering positive and negative values of LFv separately. (B–D) Phase diagram from panel A (in gray) with slipping highlighted in color (same colors as in panel A). Colored curves are plotted when SR was smaller than 0.99 (B), 0.95 (C), or 0.90 (D), i.e. when more than 1%, 5%, or 10% of the index fingertip contact was slipping against the plate.

Movement frequency had a significant effect on the amount of partial slip in the fingertip contact (Fig. 4.12). The minimum value of the stick ratio (SR) was computed for each segment of data as a way to measure the amount of partial slip during single movements. This quantity was compared across all six conditions using an ANOVA test. The test showed a significant effect of the movement frequency on the amount of partial slip ($F(5,266) = 252.62$, $p < 0.001$). Post-hoc pairwise comparisons revealed that partial slip started to increase between 90bpm and 105bpm and increased further for higher frequencies ($p < 0.005$). This means that no significant amount of partial slip was detected at 90bpm or below.

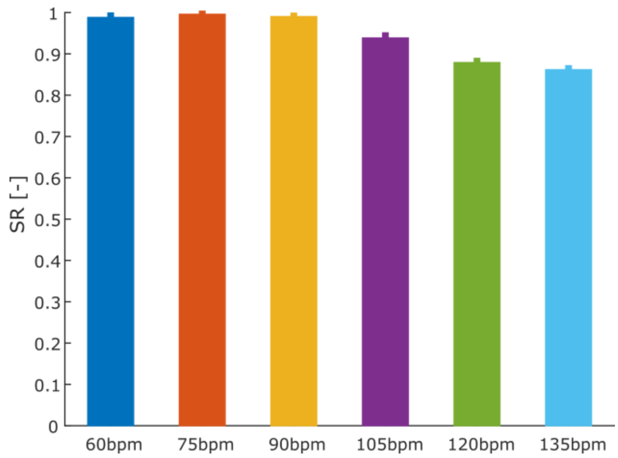

Fig. 4.12. Effect of movement frequency on the amount of partial slips. The minimum value of the stick ratio (SR), a proxy to measure partial slips, was computed for each segment. It is summarized as the mean ± SEM for the six movement frequencies. Partials slips increased significantly between 90bpm and 105bpm and increased further for higher frequencies ($p < 0.005$).

Movement frequency had also a significant effect on the amplitude of fingertip rolling for both the thumb and the index finger (Fig. 4.13). The variation of the vertical position of the COP was computed for each segment of data for the two fingers as a way to estimate the amplitude of fingertip rolling during single movements. A two-way ANOVA test was run to compare fingertip rolling across all six conditions and across the two fingers. The test showed a significant main effect of both the movement frequency ($F(5,532) = 262.63$, $p < 0.001$) and the finger ($F(1,532) = 1485.46$, $p < 0.001$), and a significant interaction between the two factors ($F(5,532) = 127.85$, $p < 0.001$). This means that fingertip rolling increased with movement frequency for the two fingers and that rolling amplitude was larger and increased faster with movement frequency for the index finger. This might be related to the morphology of the fingertips, with the thumb being larger and flatter, and thus less prone to rolling than the index finger.

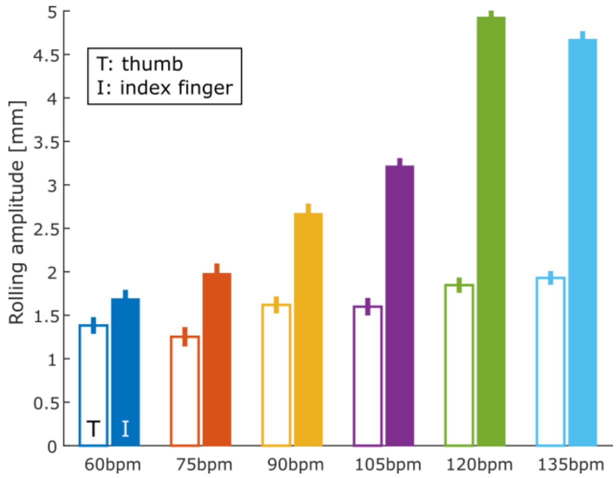

Fig. 4.13. Effect of movement frequency on the amplitude of fingertip rolling. The variation of the vertical position of the center of pressure (COP) was computed for each segment of data for the two fingers. COP variation, representing the amplitude of fingertip rolling, is summarized as the mean ± SEM for all tested frequencies and both fingers. Open bars correspond to the thumb (T) and solid bars to the index finger (I). Rolling amplitude was compared across fingers and across movement frequencies. It increased with movement frequency for both fingers ($p < 0.001$). Rolling amplitude was larger and increased faster with movement frequency for the index finger ($p < 0.001$).

The vertical position of the COP of the index finger varied significantly with the corresponding LF for all six movement frequencies ($p < 0.001$). This means that the fingertip rolling was dependent on the level of LF (Fig. 4.14).

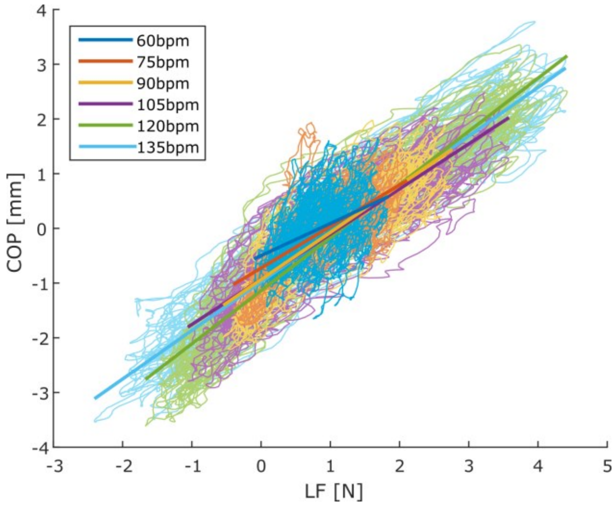

Fig. 4.14. Correlation between load force and rolling. The vertical position of the center of pressure (COP) of the index finger is plotted against the corresponding load force (LF) for all six frequencies. The overall correlation between COP, representing rolling of the fingertip, and LF was 0.9. A significant correlation was found between the variables for each condition separately ($p < 0.001$).

4.5. Discussion

4.5.1. Summary of results

The pilot study presented in the previous section demonstrated the presence of a significant amount of partial slips at the fingertip contact during object manipulation for movement frequencies of 105bpm and above. The amount of partial slip increased with movement frequency. Visual inspection of the images indicated that partial slips developed from the periphery of the contact. Overall, the relative portion of partial slip within the contact remained rather low, with a maximum of 15% of the contact slipping against the plate. Finally, the amplitude of partial slip did not evolve with time within conditions.

Results also showed that both fingertips were rolling against the plates during manipulation. Fingertip rolling increased with movement frequency. In addition, rolling was larger and increased faster with movement frequency for the index finger. Finally, rolling varied with the load force, whose amplitude increased with movement frequency. This explains why the amplitude of fingertip rolling also increased with movement frequency.

In Chapter 2, we showed that the friction coefficient at the fingertip contact was similar for both fingers. Therefore, imaging one finger can already provide a lot of information, and leaves room to have other sensors on the non-imaged finger, like a fingertip moisture sensor in order to monitor the fingertip skin hydration during manipulation. This would be desirable because it is known to influence significantly the friction properties of the contact (André et al., 2009).

Finally, the task performed here might not be the most appropriate one to highlight the influence of tactile feedback on grip force control. Indeed, it was a rhythmic task, which is known to be controlled mostly in anticipation (Flanagan and Wing, 1995). Therefore, it is likely that tactile feedback had only a minor influence on grip force in this context. In contrast, force coordination during a discrete task consisting of lift-and-hold or point-to-point movements is more likely to be modulated by tactile feedback. Therefore future experiments run with the developed device should focus primarily on discrete tasks.

4.5.2. Future directions

Johansson and Westling hypothesized that continuous tactile feedback arises from partial slips occurring at the periphery of the fingertip contact, and that this feedback could play a role in force coordination during object manipulation (Johansson and Westling, 1987). However, they could not measure partial slips directly and therefore they could not investigate this hypothesis further. Our observation of the systematic occurrence of partial slips at the periphery of the fingertip contact during manipulation is encouraging and opens the way for several research questions discussed in this section.

First, the nature of the tactile feedback provided by partial slips (in particular) and strain patterns at the surface of the skin (in general) is not clear. This will be investigated in the next Chapter, where we will examine tactile afferent responses elicited by strain patterns produced in the skin under tangential loading of the fingertip in conditions compatible with object manipulation.

Then, with the reasonable assumption that partial slips and surface strains generate behaviorally relevant feedback signals, it is not clear how the central nervous system (CNS) would use these signals during manipulation. There is a large body of evidence from the neurophysiology literature demonstrating the importance of tactile afferent signals from the fingertips in object manipulation and showing their capacity to trigger corrective motor responses. Some important results are summarized here. First, previous studies used digital anesthesia to demonstrate that the lack of tactile feedback negatively affects force coordination during manipulation and impedes our ability to adjust the grip force in response to unexpected perturbations (Augurelle et al., 2003; Nowak et al., 2002). Second, perturbations applied during restraint of an object with the precision grip evoke tactile afferent signals able to influence the grip response (Macefield et al., 1996). Third, tactile information can be processed fast enough in the somatosensory pathways to account for the use of tactile signals in natural manipulation (Johansson and Birznieks, 2004). Finally, tactile afferents can encode physical properties of objects relevant for manipulation, such as surface curvature (Jenmalm et al., 2003) and the magnitude and direction of the forces and tangential torques applied to the digits (Birznieks et al., 2001, 2009, 2010; Khamis et al., 2015). Therefore, it is worth investigating how partial slips and surface strains could help the CNS to coordinate forces applied on object during manipulation and to react to unforeseen external perturbations.

However, this investigation must take into account the relatively long time delays in the sensorimotor control loops engaged in corrective actions, i.e. approx. 100ms (Miall et al., 1993). In addition, proprioceptive afferents are also stimulated by perturbations applied during restraint of an object (Macefield and Johansson, 1996). These afferents are known to be involved in short-latency (< 60ms) sensorimotor feedback loops (Crevecoeur et al., 2017; Macefield and Johansson, 2003). Therefore, their contribution should also be taken into account when investigating grip force corrections. In this regard, digital anesthesia is an interesting technique to disentangle the effects of tactile and proprioceptive feedback on force coordination during manipulation. However, one should keep in mind that it is difficult to silence one of these two types of feedback without affecting the other. Indeed, digital anesthesia can suppress tactile signals arising from the finger pad, but it cannot prevent vibrations generated at the fingertip contact from propagating through the hand and arm and be captured by remote tactile afferents, especially of the FA2 type, which are highly sensitive to vibrations (Delhaye et al., 2012; Manfredi et al., 2012; Shao et al., 2016). Reciprocally, silencing proprioceptive feedback while keeping the tactile feedback intact is virtually impossible because proprioceptive feedback arises from receptors distributed everywhere in the upper limb, i.e. in joints, tendons, muscles and even skin through SA2 afferents (Edin, 1992; Edin and Johansson, 1995).

Besides, another research avenue is to examine the influence of partial slips and strain patterns on the adaptation of the predictive mechanisms, or internal models, in the CNS during manipulation. Indeed, tactile afferents are required for setting and maintaining the background level of the grip force during manipulation (Augurelle et al., 2003). Moreover, successful manipulation requires the CNS both to predict the motor commands required to grasp, lift and move objects (via inverse internal models), but also to predict the sensory events that arise as a consequence of these commands (via forward internal models) (Flanagan et al., 2006; Wolpert and Flanagan, 2001). Therefore, it is reasonable to hypothesize that partial slips might play a role in the online adaptation of forward internal models in the CNS by helping it to compare the expected sensory consequences of the motor commands with the actual sensory signals.

In this context, partial slips and strain patterns at the surface of the skin could help the CNS estimate the friction at the fingertip contact to adapt the grip force in consequence. The question of the encoding of fingertip friction by the tactile system is complex and has not been elucidated yet, even though it is clear that the friction between fingertips and object is encoded by tactile afferents quickly after the initial contact (Johansson and Westling, 1984; Khamis et al., 2014a). The mechanism by which the CNS estimates fingertip friction at initial contact but also continuously during manipulation could involve partial slips and strain patterns in the fingertip contact.

Finally, finger pad deformations are composed of both volume deformations and surface deformations that occur together under tangential loading of the fingertip (Delhaye et al., 2016). Due to the folded structure of the superficial layers of fingertip skin, i.e. fingerprint ridges, surface deformations of the skin do not cause large deformations in deeper tissue. This is why we separate surface deformations from volume deformations. Here, the significant amplitude of fingertip rolling against the plate measured in the pilot study suggests that volume deformations are far from negligible during manipulation. Therefore, volume deformations of the finger pad must be considered together with surface deformations caused by partial slips and strains when examining the effect of tactile feedback on force coordination and manipulation performance.

4.5.3. Technical improvements

The pilot study reported here was intended as a commissioning of the manipulandum. The device is functional but it could be improved in many aspects. Here is non-exhaustive list of the primary improvements.

First, the weight compensation is not optimal because the ball bearings of the pulleys guiding the rope linking the counterweight to the device generate a lot of mechanical noise, as observed on the FFT of the load force signal. The weight compensation system must therefore be improved and in particular the pulleys.

Then, the position of the manipulandum should be measured with millimeter precision to have a precise view of its trajectory. This could help to detect small slips during manipulation. Reconstructing the trajectory of the device from the measured acceleration is not feasible due to the drift of the accelerometer signals. One interesting solution would be to use an external 3D motion capture system to track the position and orientation of the manipulandum in real time.

Next, in order to investigate the research questions described in the previous section, the experimenter must have the capacity to modify the physical properties of the object to perturb the subjects and examine their reaction. The perturbations could involve changing the mass of the manipulandum, the type of load (have a viscous load instead of an inertial one, e.g.), apply unexpected pulling and pushing loads on the object, and change the friction at the fingertip contacts. These perturbations should be applicable between trials and, whenever possible, during trials as well.

In addition, to precisely measure the motor response following perturbations, the EMG signal of arm and hand muscles active during manipulation should be recorded. The EMG signal as well as force and acceleration data should be acquired at a much higher frequency than 200Hz. An acquisition frequency equal to or higher than 1kHz would be desirable to have recordings with millisecond resolution.

Finally, from a data processing point of view, I recommend using the *slip ratio* rather than the stick ratio to summarize partial slips at the fingertip contact. The slip ratio would be defined as the proportion of slippage in the contact whereas the stick ratio is defined as the proportion of the contact not slipping relative to the surface. Both variables are complementary and their sum is always equal to one. However, in my opinion, the slip ratio is a much more natural way of representing slippage. Historically, the stick ratio was introduced by Tada et al. (Tada et al., 2006) when they investigated incipient slip occurring at the fingertip contact. Given that the contact transitioned from full stick to full slip, the stick ratio was chosen to measure of the evolution of slip. This has then been used by André et al. (André et al., 2011), Delhaye et al. (Delhaye et al., 2014), and here. However, it is counter-intuitive to measure incipient slip with a variable transitioning from 1 to 0 when slip increases. Instead, the slip ratio transitions from 0 to 1 when slip increases and thus offers a measure that is proportional to the physical quantity being measured, which is more intuitive.

CHAPTER 5

Human tactile afferent responses to skin strain patterns caused by fingertip shearing

"You just keep on trying till you run out of cake."

GlaDOS (Portal)

The content of this Chapter is based on the material presented at the 46th Annual Meeting of the Society for Neuroscience: A. Barrea*, E. Jarocka*, P. Lefèvre, J.-L. Thonnard, B.B. Edin, B.P. Delhaye. Human tactile afferent responses to skin strain patterns caused by fingertip shearing. Program No. 151.02. 2016 Neuroscience Meeting Planner. San Diego, CA: Society for Neuroscience, 2016. Online. (*) equal contribution.

Data presented in this Chapter were acquired and analyzed with the help of Ewa Jarocka and Prof. Benoni B. Edin, Department of Integrative Medical Biology, Umeå University, Umeå, Sweden. This work is based on a protocol presented in the Ph.D. dissertation of B.P. Delhaye, who also participated in the data analysis.

5.1. Introduction

Strain patterns are produced in the skin when a fingertip is pressed against a surface and then loaded tangentially. These strain patterns evolve during increasing loading and are specific to the loading direction (Delhaye et al., 2016). Strains at the surface of the fingertip skin can be precisely measured through direct imaging of the fingertip contact as described in Chapter 4. Previous studies examined the response of tactile afferents to strain patterns produced in the skin (Johansson and Vallbo, 1983; Sripati et al., 2006). Edin found that tactile afferents in the hairy skin encode nearby joint configuration with the same precision as proprioceptive afferents (Edin, 1992, 2004). However, no study to date related tactile afferent responses to the specific skin strain patterns produced at the fingertip-object contact during tactile interactions.

To fill this gap, we have combined strain imaging with single-unit recordings in awake human subjects, a technique also known as microneurography. Responses were recorded from 39 afferents terminating in the human hand, 19 of which had receptive fields at least partially within the fingertip contact. Strain patterns were induced in the contact by tangential fingertip loadings similar to those experienced during dexterous manipulation. Four frictional conditions and four stimulation directions were tested. The simultaneous recording of strains and tactile afferent responses elicited by tangential loading of the fingertip allowed the link between these strains and the responses of the afferents to be investigated. Most afferents showed a strong response to the onset of the loading, and some displayed continuous discharges during the whole transition from sticking to sliding of the fingertip contact. Both the frictional condition and the stimulation direction strongly influenced the afferent responses.

5.2. Methods[4]

5.2.1. Participants

Sixteen healthy human subjects participated in the experiment (9 males; ages 19–24). Each subject provided written informed consent to the procedures, which were approved by the ethics committee at the host institution (Institute of Neuroscience, Université catholique de Louvain, Brussels, Belgium). Subjects were seated comfortably in a reclining chair with their forearm rested comfortably on a horizontal support. Their hand, with

[4] The protocol used in this study is based on the one described in Delhaye (2014).

the volar side facing the ground, was fixed to a custom-made support (Fig. 5.1A and Fig. 5.1C). A flat aluminum bar was glued to the nail of the index and middle fingers and then clamped to the support. The support ensured that the finger did not move during stimulation, even though deformations of the fingertip were still possible due to the compliance of the finger pad.

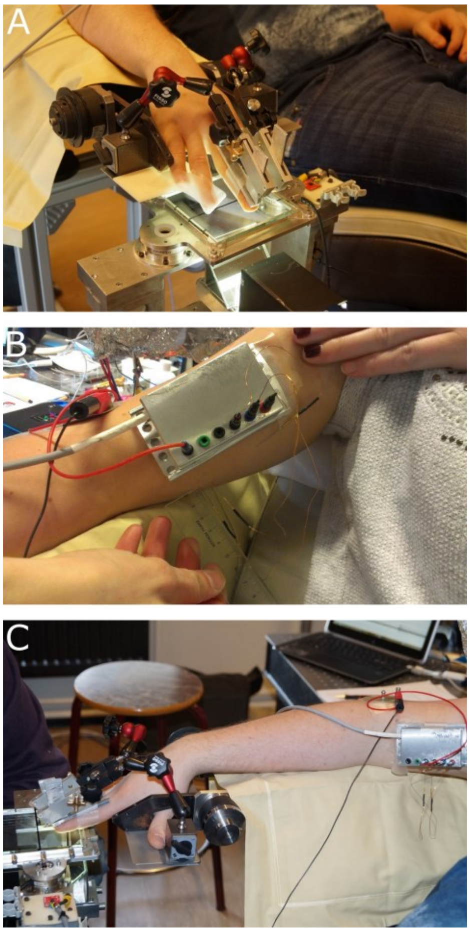

Fig. 5.1. Experimental setup. (A) Subject's hand fixed in the finger support. A flat metal bar is glued on the fingernail of the index and middle finger and then clamped in the support. The support allows a precise positioning of the fingertip prior to the experiment and ensures that fingertips do not move during trials. **(B)** Illustration of the nerve-recording apparatus. Tungsten electrodes are inserted percutaneously in the arm of the subjects, 10cm proximal to the elbow and then in the median nerve. Neural signals are amplified close to the recording site before being sampled on a dedicated computer. **(C)** View of the right upper limb of a subject, with the hand support and the electrodes. The arm was rested comfortably on a horizontal support.

5.2.2. Apparatus

The same robotic platform was used as in Chapter 3. This robotic platform was based on an industrial robot able to move a flat plate in three orthogonal directions (Denso Robotics, Japan). Two force transducers mounted on each side of the plate measured the forces applied to it by the subject's fingertip (ATI force sensors, ATI Industrial Automation, Apex, NC). Two different plates were used to stimulate the fingertip, each one consisting of two materials. On the one hand, a transparent plate consisted of smooth glass and smooth glass covered with RainOff, a hydrophobic coating strongly reducing the friction at the fingertip contact (Arexons, Italia). On the other hand, a non-transparent plate consisted of silk and sandpaper. All four materials, called the stimuli, exhibited different frictional properties. More details about the frictional properties of the stimuli are presented in Appendix A.

The robot was combined with a custom-made fingerprint imaging apparatus composed of a high-speed (50fps) and high-resolution (1200dpi) camera (Mikrotron MC1362, 1280x1024 pixels, Mikrotron GmbH, Germany) and a coaxial light source (White LED Backlight, Phlox, France). This optical apparatus enabled imaging of fingerprints in contact with the transparent stimuli in order to compute strains in the fingertip contact as described in Chapter 4.

5.2.3. Neural recordings

Impulses from tactile afferents innervating the right index or middle finger of the subjects ("units") were recorded from the median nerve. Insulated tungsten microelectrodes were inserted percutaneously in the arm of the subjects, approximately 10cm proximal to the elbow (Fig. 5.1B) and then into the nerve following procedures fully described in (Vallbo and Hagbarth, 1968) and summarized here. The skin of the fingertips was continuously palpated by one experimenter while another one manipulated the electrode. Palpation helped locate the receptive field of the unit in contact with the electrode by stimulating afferents in the whole fingers. Once a single unit was isolated, calibrated von Frey hairs were used to locate precisely the center of its receptive field and determine its mechanical threshold. The center of the receptive field was marked on the skin with a fine-pointed ink pen.

The afferents were classified as slow adapting type I (SA1), slow adapting type 2 (SA2), fast adapting type 1 (FA1) or fast adapting type 2 (FA2) according to their response to sustained indentation and the structure of their receptive field (Johansson and Vallbo, 1983; Vallbo and Johansson, 1984). First, afferents responding only to the onset and offset of skin indentation were classified as fast adapting whereas those responding continuously to sustained indentation were classified as slow adapting. In addition, the regularity of the discharge rate, the extent of the receptive field and the mechanical threshold of the afferent helped further classify the afferents as type 1 or type 2. The search was voluntarily biased towards type 1 afferents because of their relatively small receptive field, which makes them more likely to respond precisely to the local strain patterns recorded within the fingertip contact.

5.2.4. Experimental procedures

While recording impulses from single tactile afferents innervating the right index or middle finger of subjects, the stimulus was moved perpendicularly towards the finger pad in single trials, made contact and reached a preset normal force (NF) that was kept constant during the trial. After a short delay, the surface was moved horizontally with a constant speed (5.5mm/s) first in one direction (ulnar, radial, distal or proximal) for 8mm ("forward movement") and then in the opposite direction for 12mm ("backward movement"). The movement amplitudes were thus large enough to ensure eventually full sliding between the fingertip and the surface in both directions. The trial ended when the surface was retracted from the finger. The total duration of each trial was 6s.

Four different frictional conditions were tested in two similar protocols. On the one hand, the "transparent" protocol was performed using the transparent plate (glass + RainOff). On the other hand, the "non-transparent" protocol was performed with the non-transparent plate (silk + sandpaper). Therefore, four frictional conditions, corresponding to the four materials, were tested in total. Each protocol consisted of five repetitions of the four stimulation directions for each one of the two materials, totalizing 40 trials (2 materials x 4 directions x 5 repetitions). Importantly, the two protocols were not tested on all units because of the limited recording time available before losing the unit. Table 5.1 summarizes the number of protocols run for each afferent class.

Different levels of NF were used depending on the materials and the subjects. For both transparent materials, NF was always controlled at 4N. For sandpaper, lower NF levels of 1N or 1.5N were used in order not to harm the subject's fingertip. For silk, NF levels ranged between 1.5N and 6N, and it was fixed at a level maximizing the occurrence of stick-and-slip at the finger contact. Despite these variations across materials, the same NF level was applied for all trials with a given material and a given subject. The chosen NF levels were compatible with force levels used during manipulation.

5.2.5. Data acquisition and data processing

Force and position signals

Position of the plate and forces exerted on the finger were recorded at 1kHz during the trials. For the transparent protocol, fingerprint deformations were monitored through the transparent plate during horizontal movement of the platform, allowing derivation of surface strains in the fingertip contact.

Neural signal

The neural signals were sampled at 12.8kHz after amplification close to the recording site. Identification of single action potentials was performed semi-automatically under visual control (Edin et al., 1988). WINSC/WINZOOM software (University of Umeå, Sweden) was used for recording and analysis of neural data. The instantaneous discharge rate was defined as the inverse of the time interval between two consecutive spikes. This discharge rate signal was re-sampled at 1kHz in order to match the acquisition frequency of the force and position signals and have convenient time series for data analysis.

Image processing to compute fingertip contact mechanics

Images of the fingerprints in contact with the transparent stimuli were processed as described in Chapter 4 to compute local surface deformation and rotation. Briefly, the contour of the fingertip contact was segmented automatically. Then, feature points were sampled within the contact and tracked from frame to frame in order to measure the displacement field in the contact. Next, the gradient of this displacement field was estimated from the local displacement of the feature points. Finally, Green-Lagrange strains were computed locally according to equation (5.1), where ε_{xx} and ε_{yy} are the axial strains aligned to the x and y axes, respectively, ε_{xy} is the shear strain, and u and v are the displacement along the x and y axes, respectively. The x and y axes are tangential to the plate and are the same as the global reference frame defined for this study (Fig. 5.2A).

$$\varepsilon_{xx} = \frac{\partial u}{\partial x} + \frac{1}{2}\left[\left(\frac{\partial u}{\partial x}\right)^2 + \left(\frac{\partial v}{\partial x}\right)^2\right] \quad (5.1a)$$

$$\varepsilon_{yy} = \frac{\partial v}{\partial y} + \frac{1}{2}\left[\left(\frac{\partial u}{\partial y}\right)^2 + \left(\frac{\partial v}{\partial y}\right)^2\right] \quad (5.1b)$$

$$\varepsilon_{xy} = \frac{1}{2}\left(\frac{\partial u}{\partial y} + \frac{\partial v}{\partial x}\right) + \frac{1}{2}\left(\frac{\partial u}{\partial x}\frac{\partial u}{\partial y} + \frac{\partial v}{\partial x}\frac{\partial v}{\partial y}\right) \quad (5.1c)$$

The principal strain components, denoted e_1 and e_2, were computed by eigenvalue decomposition of the local strain tensor according to equation (5.2), where $\boldsymbol{\varepsilon}$ is the local strain tensor, which is symmetric by definition, and $\boldsymbol{v_1} = (v_{1x}, v_{1y})$ and $\boldsymbol{v_2} = (v_{2x}, v_{2y})$ represent the orthogonal eigenvectors.

$$\boldsymbol{\varepsilon} = \begin{bmatrix} \varepsilon_{xx} & \varepsilon_{xy} \\ \varepsilon_{xy} & \varepsilon_{yy} \end{bmatrix} = \begin{bmatrix} v_{1x} & v_{2x} \\ v_{1y} & v_{2y} \end{bmatrix} \cdot \begin{bmatrix} e_1 & 0 \\ 0 & e_2 \end{bmatrix} \cdot \begin{bmatrix} v_{1x} & v_{2x} \\ v_{1y} & v_{2y} \end{bmatrix}^{-1} \quad (5.2)$$

The principal strains e_1 and e_2 correspond to the maximum tensile and compressive strains at the location where the strain tensor is measured. The eigenvalue decomposition is equivalent to a rotation of the reference frame so that the shear strain is cancelled and only axial strains remain, which thus correspond to the maximum dilation and/or compression. Therefore, the principal strains do not necessarily act along the axes of the x-y reference frame defined above and act along directions potentially different for each local strain tensor.

We make the hypothesis that strains in the direction normal to the surface are negligible compared to surface strains because of the folded structure of the superficial layers of the fingertip skin, i.e. fingerprint ridges, which makes it possible to have large surface deformations with relatively low volume deformations. Therefore, the matrix components of the local strain tensor $\boldsymbol{\varepsilon}$ are solely given by the axial and shear strains along the x-y plane (ε_{xx}, ε_{yy} and ε_{xy}). In addition, given the high stiffness of the outer layer of the skin (Wang and Hayward, 2007), it is reasonable to assume that the area of local patches of skin is conserved after deformation. Under this hypothesis, it can be shown that $e_1 \geq 0 \Leftrightarrow e_2 \leq 0$ and vice-versa. This means that if one of the principal strain is dilative, the other one is compressive and vice-versa. An intuitive demonstration of this idea is presented in the Supplemental material section. Moreover, we follow the customary habit to sort the eigenvalues by descending order. Therefore, e_1 will always be larger than e_2. Under the hypothesis of area conservation, this implies that e_1 will be positive and thus tensile whereas e_2 will be negative and thus compressive. This hypothesis has been verified in practice on the data (Fig. 5.8).

Besides, the local rotation of the skin was computed from the gradient of the displacement field according to equation (5.3).

$$\omega = \frac{1}{2}\left(\frac{\partial u}{\partial y} - \frac{\partial v}{\partial x}\right) \tag{5.3}$$

Finally, as described in Chapter 4, strains and rotation were first computed as strains and rotation *rates*, i.e. the relative deformation between pairs of consecutive frames, and then integrated over time to compute the total strains and rotation, i.e. the deformation of the contact relative to the initial frame.

5.3. Results

Responses were recorded from 39 afferents terminating in the human hand, 19 of which had receptive fields at least partially within the fingertip contact, allowing relating their response to the mechanical deformations that arise within the contact during tangential loading. Fig. 5.2B presents the location of the centers of the receptive fields for the type 1 afferents. Receptive fields of the type 2 afferents are not reported because of their large and poorly defined nature. Table 5.1 summarizes the number of afferents from each class recorded in this study.

Fig. 5.3 illustrates a typical trial performed on glass in the ulnar direction. The robot pressed the stimulus against the finger pad in the vertical direction and waited for the normal force (NF) to stabilize at 4N. Then, it moved horizontally with a constant speed of 5.5mm/s first in the ulnar direction ("forward movement"). Then, after a short pause, it moved in the opposite, i.e. radial, direction ("backward movement"). The unit was of class FA1 and responded vigorously to the onset and offset of the normal loading of the plate, with a discharge rate reaching 200Hz. In addition, it also responded to the onset of the two horizontal movements. Strains recorded during the first horizontal movement showed that the leading edge of the contact experienced compression while the trailing edge was dilated, as observed in a previous study (Delhaye et al., 2016).

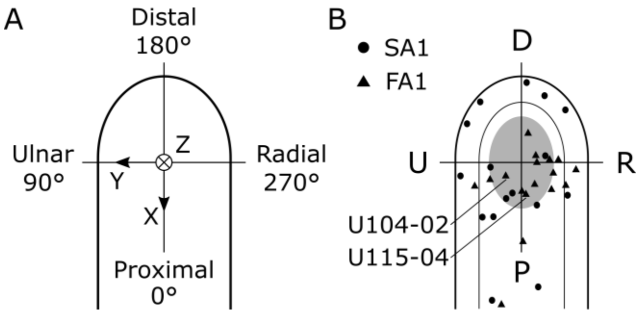

Fig. 5.2. Reference frame, stimulation directions and centers of the receptive fields (RF) of the recorded units. (A) Schematic representation of a fingertip. Stimulation directions were defined on an anatomical basis, with the radial direction pointing towards the thumb of the subject and the proximal direction towards the wrist. A right-handed reference frame was defined for forces, position and strains, with the positive x axis pointing in the proximal direction and the positive y axis pointing in the ulnar direction. **(B)** Location of RF centers of the recorded type 1 afferents (SA1, circles, and FA1, triangles). The gray ellipse represents the initial fingertip contact surface. The receptive field of 19 afferents out of the 39 recorded lay at least partially within the initial contact or entered the contact during loading due to fingertip rolling.

Table 5.1. Number of units from each class recorded in the transparent and non-transparent protocols. For the transparent protocol, the number of units from each class with their receptive field (RF) at least partially within the fingertip contact is also reported. Because of the limited recording time available with a given unit, the two protocols were not run on all units. The "total" row summarizes the number of units on which either one of the two protocols, or both of them, was performed.

Units count	SA1	SA2	FA1	FA2	Total
Non-transparent protocol	14	2	13	2	31
Transparent protocols	6	4	16	1	27
Transparent (RF within contact surface)	5	2	12	0	19
Total	16	4	17	2	39

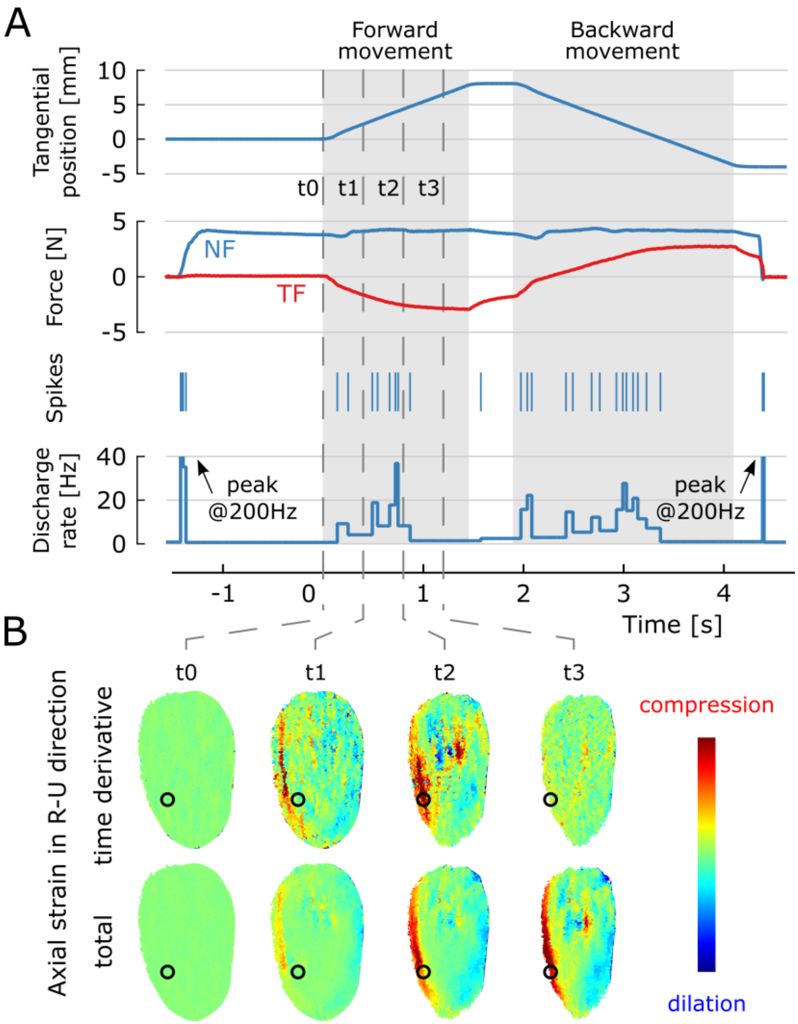

Fig. 5.3. Typical trial on glass in the ulnar direction for unit U104-02 (FA1). (A) Forward and backward movements of the robot (gray areas). The forward movement is in the ulnar direction and the backward movement is in the radial direction. The normal force (NF, blue) was controlled at 4N. The tangential force (TF, red) started to increase at the onset of the horizontal movement. The unit responded vigorously to the onset and offset of the normal loading of the plate and also to the onset of both horizontal movements. **(B)** Axial strain along the radial-ulnar direction recorded at the surface of the fingertip skin in contact with the glass. Strain rate (i.e. time derivative, top row) and total strain (bottom row) are displayed for four different times separated by 400ms and sampled during the forward movement (t0 to t3). The ulnar side is on the left of the images, according to the directions defined in Fig. 5.2A. The leading edge of the contact is in compression (red) and the trailing edge in dilation (blue). Black circles indicate the location of the center of the afferent's receptive field.

The dynamic coefficient of friction (CF) was computed for the forward and backward movements on glass and glass covered with RainOff. This coefficient was computed as the ratio of the tangential to the normal force during plateau of the tangential force at the end of horizontal movements. These measurements confirmed that the RainOff dramatically decreased the dynamic CF for all subjects (Fig. 5.4A). However, no effect of the movement direction (forward or backward) was observed on the dynamic CF (Fig. 5.4B). CF was also computed for trials performed with silk and sandpaper. Due to the varying NF between materials and between subjects, it is not straightforward to summarize these measurements, especially because the coefficient of friction is known to vary dramatically with NF (André et al., 2009). Nevertheless, dynamic CF measured for the four materials in individual subjects is presented in Fig. 5.6. These measurements confirm that the friction was also significantly different between the two non-transparent materials for all subjects.

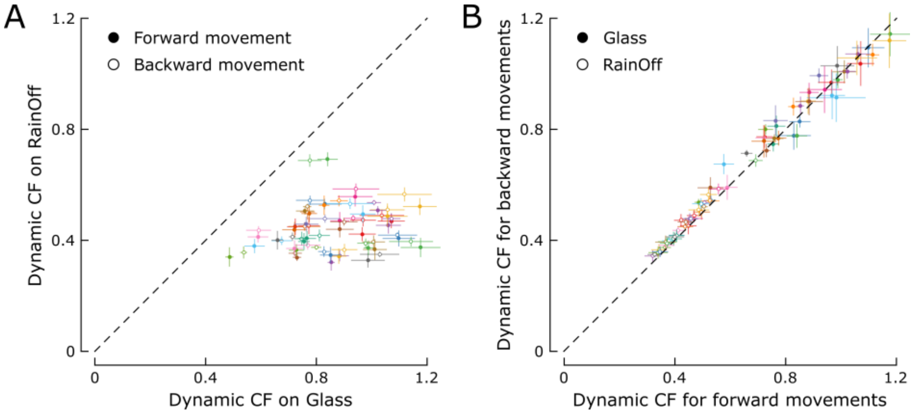

Fig. 5.4. Friction measured on glass and glass + RainOff for the forward and backward movements. (A) Dynamic coefficient of friction (CF) measured for all subjects (one color per subject) for RainOff vs. bare glass. Dynamic CF was measured for the forward movement (solid dots) and the backward movement (open dots) of each trial. Error bars show 95% confidence intervals. The dynamic CF was significantly lower with RainOff than with bare glass. **(B)** Same data as in panel A represented for the backward vs. forward movements. Solid dots correspond to trials on glass and open dots to trials on RainOff. Overall, the dynamic CF was similar across the forward vs. backward movement for all subjects.

Most units exhibited a marked directional preference (Fig. 5.5). This directional preference was consistent across frictional conditions. The sensitivity of the units in each of the four stimulation directions (ulnar, distal, radial and proximal) was established by counting the number of spikes elicited during a period of 400ms at the onset of the forward movement. Several units responded preferentially for two opposite directions, e.g. radial-ulnar, or distal-proximal, while others responded only to stimulations in one direction.

In contrast, most units responded with the same intensity to the onset of horizontal movements in the different frictional conditions. Fig. 5.6 presents the number of spikes elicited during a period of 400ms at the onset of the forward movements for each material, with responses averaged across stimulation directions. These responses were plotted against the measured dynamic coefficient of friction. No marked difference was observed between the responses to the different materials, indicating that the dynamic coefficient of friction was not encoded at the onset of the horizontal movements, i.e. before slip onset. These similar responses across frictional conditions might be explained by the fact that spikes were averaged during a short amount of time (400ms) and, importantly, before slip onset. During this short time interval, the load force exhibits a similar profile for the two non-transparent conditions as reported in previous work (Johansson and Westling, 1984). In addition, even though the total number of spikes is similar across frictional conditions, their timing might be different, as illustrated on Fig. 5.7 later in the text.

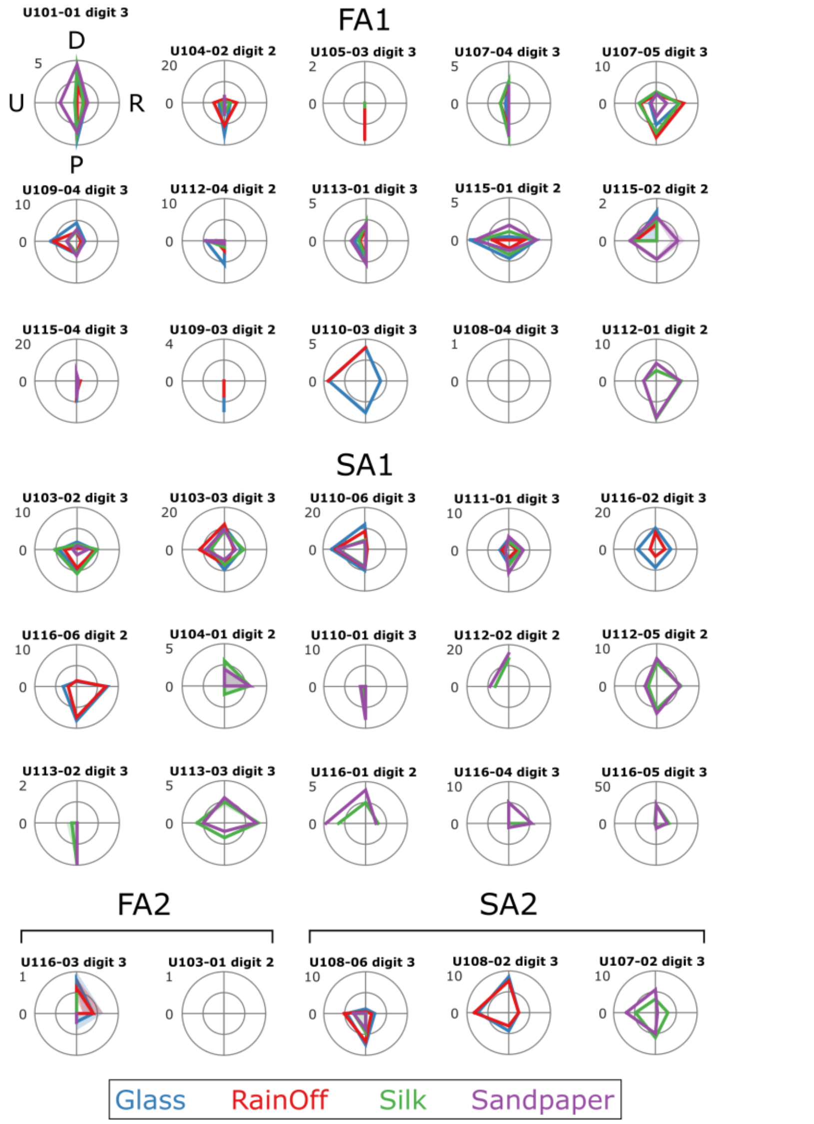

Fig. 5.5. Directional sensitivity of units across frictional conditions. Polar diagrams show the number of spikes elicited during a period of 400ms at the onset of the forward movements. The four stimulation directions are represented on the top-left diagram: ulnar (U), distal (D), radial (R) and proximal (P). Most units exhibited a directional preference, either in one or in two opposite directions. This directional preference was consistent across frictional conditions: glass (blue), glass covered with rainoff (red), silk (green) and sandpaper (purple). Data are represented as the mean ± SEM across all repetitions for a given direction and material. The number on the top-left corner of each diagram indicates the scale of the outer circle in spike count. Units that were lost shortly after the beginning of the protocol and on which less than two conditions were tested are not represented.

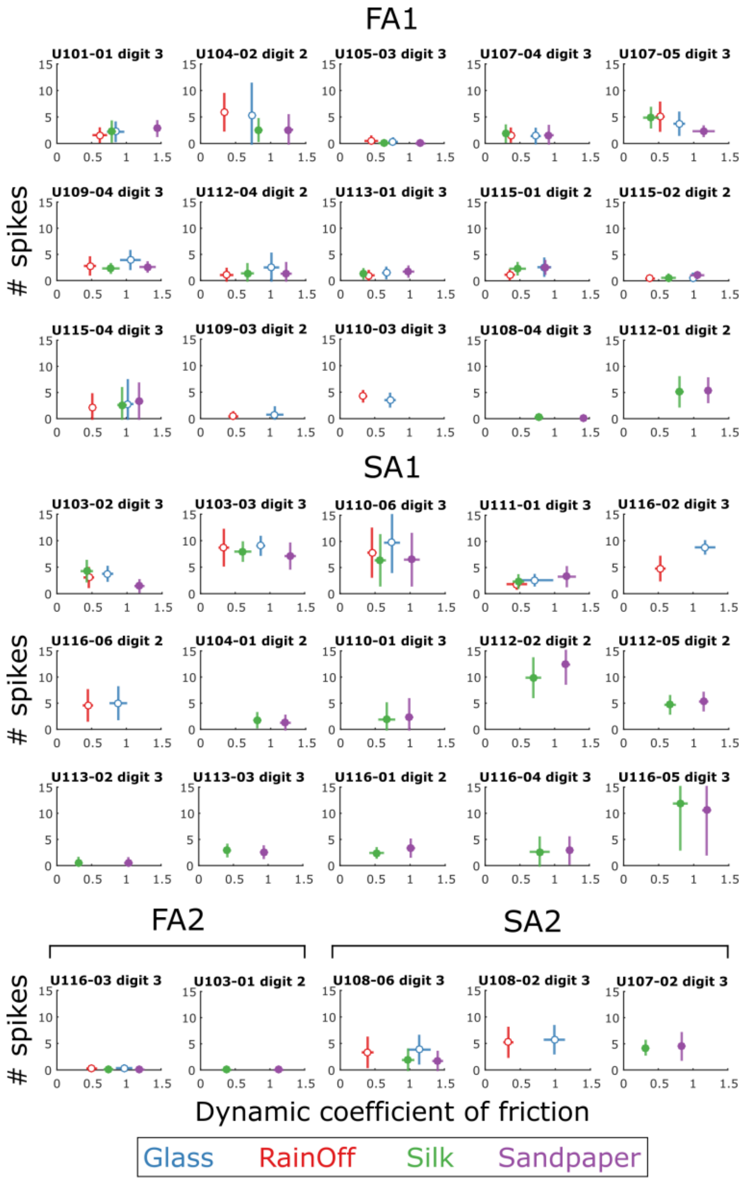

Fig. 5.6. Responses of units to materials of different friction. The number of spikes elicited during a period of 400ms at the onset of the forward movements is plotted for each material against the dynamic coefficient of friction of this material. Units are the same as in Fig. 5.5. Open dots represent the transparent materials: glass (blue) and glass covered with RainOff (red). Solid dots represent the non-transparent materials: silk (green) and sandpaper (purple). Data are represented as the mean ± standard deviation across all trials performed with a given material.

Due to the short time period available to run the protocol before losing the unit being recorded, the transparent plate was not cleaned between trials. As a result, fingerprints from previous trials were left on the glass, creating artifacts that disrupted the automatic detection of the contour of the fingertip contact and therefore impeded the analysis of the images and the computation of the surface strains. As a consequence, image data from only two units are presented here: U104-02 and U115-04.

These two units are of class FA1 units and both have their receptive fields (RF) within the contact. The location of the center of their RF is indicated in Fig. 5.2B. Unit U104-02 responded preferentially in the proximal direction and U115-04 in the distal and proximal directions (Fig. 5.5). Results from the transparent protocols run with these units are presented. Fig. 5.7 displays the temporal evolution of the forces, strains and discharge rate measured during horizontal movements in the proximal direction, for which both units had a strong response. Strains were measured within the estimated RF, i.e. in a small circle around their RF centers as illustrated in Fig. 5.3B. For both units, similar patterns were observed between the response of the unit and the strain rates, and especially the rate of the maximum compressive strain, for both forward and backward movements. Because of the lower friction in the RainOff condition, strains developed earlier within the contact than in the bare glass condition and with a somewhat lower amplitude. This lower, earlier peak on RainOff compared to bare glass was also observed on the discharge rate of the units. This suggests a strong link between strains in the RF and the response of the afferents. In addition, the responses were elicited at the onset of the horizontal movement, i.e. during incipient slip, before the tangential force reached its plateau.

Fig. 5.7. Temporal evolution of the forces, strains and response of two FA1 afferents with their receptive fields within the fingertip contact for movements in the proximal direction. (A) U104-02 (page 118) and **(B)** U115-04 (page 119). Signals and their time derivatives are plotted vs. time for all movements in the proximal direction performed on bare glass (blue) and glass covered with RainOff (red). Data are displayed as the mean ± SEM across all repetitions. Data for backward movements come from trials whose first horizontal movement was in the distal direction and thus the second horizontal movement was in the proximal direction.

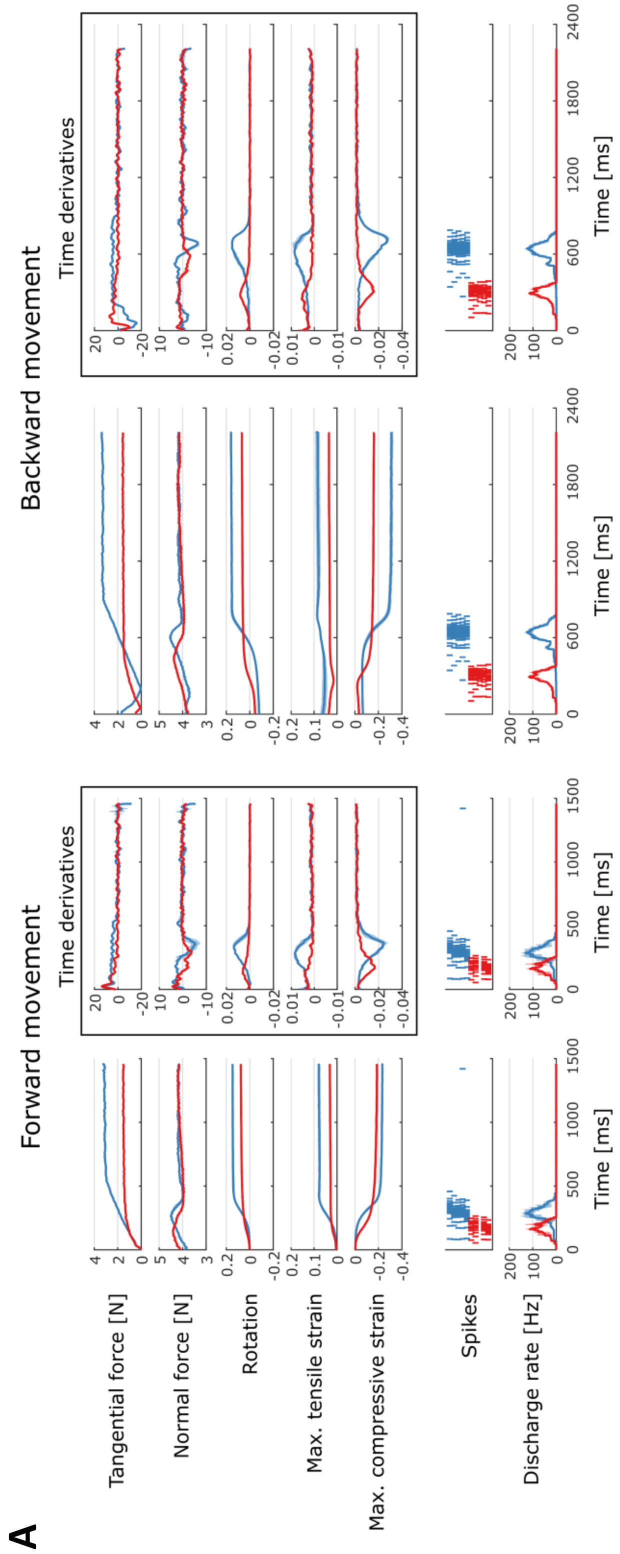
A
Forward movement
Backward movement
Time derivatives
Time derivatives
Tangential force [N]
Normal force [N]
Rotation
Max. tensile strain
Max. compressive strain
Spikes
Discharge rate [Hz]
Time [ms]
Time [ms]
Time [ms]
Time [ms]

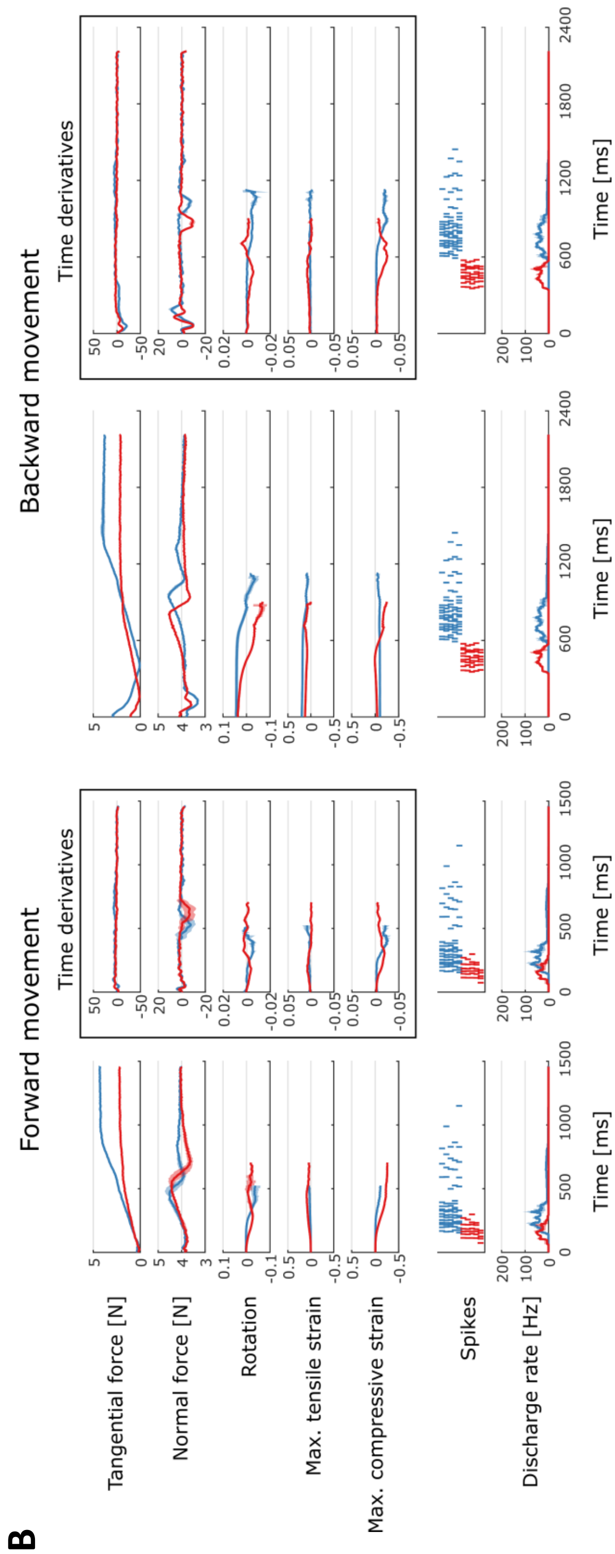

B
Forward movement
Backward movement
Time derivatives
Tangential force [N]
Normal force [N]
Rotation
Max. tensile strain
Max. compressive strain
Spikes
Discharge rate [Hz]
Time [ms]

Fig. 5.8 presents the discharge rate of the two units plotted against rates of strain components for movements performed in the four stimulation directions during transparent protocols. The measured strain components seem to correlate with tactile afferent discharges but not in all conditions. In addition, units sometimes responded in the absence of strains. Together, these observations indicate other causes of the discharge than surface strains.

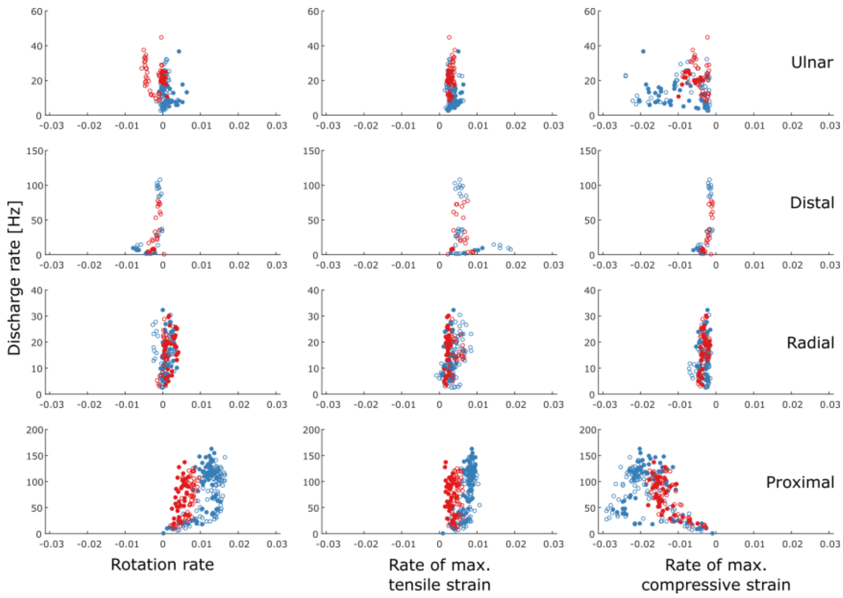

Fig. 5.8A. Relationship between discharge rate and strain components for U104-02. Discharge rate of the units plotted vs. rates of strain components for horizontal movements performed on bare glass (blue) and glass covered with RainOff (red). Strain components and discharge rates were sampled at midpoint between consecutive spikes. Data are grouped by movements performed in the same stimulation direction (ulnar, distal, radial or proximal), either during the forward movement (solid dots) or during the backward movement (open dots). Units responded more vigorously to movements performed in the proximal direction, which is their preferred stimulation direction.

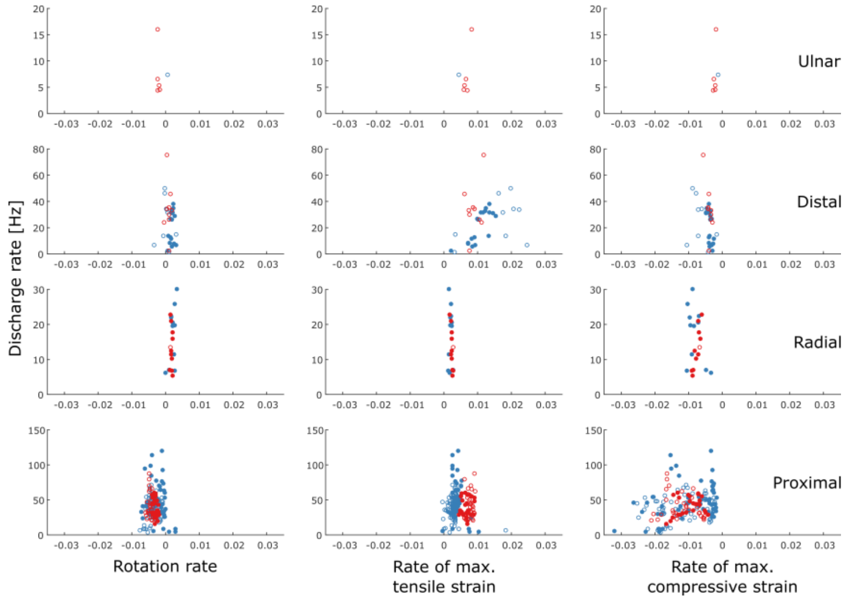

Fig. 5.8B. Relationship between discharge rate and strain components for U115-04. Discharge rate of the units plotted vs. rates of strain components for horizontal movements performed on bare glass (blue) and glass covered with RainOff (red). Strain components and discharge rates were sampled at midpoint between consecutive spikes. Data are grouped by movements performed in the same stimulation direction (ulnar, distal, radial or proximal), either during the forward movement (solid dots) or during the backward movement (open dots). Units responded more vigorously to movements performed in the proximal direction, which is their preferred stimulation direction.

5.4. Discussion

This study combined strain imaging at the fingertip contact with microneurography recordings of tactile afferents innervating the tips of the right index and middle fingers of human subjects. The simultaneous recording of strains and tactile afferent responses elicited by tangential loading of the fingertip allowed us to investigate the link between strains and afferent responses. Four stimulation directions and four materials exhibiting different friction properties were tested.

We found that most afferents responded preferentially to stimulations acting in one or two opposite directions. This directional preference was consistent across frictional conditions. Besides, the dynamic coefficient of friction of the materials did not seem to be encoded during the onset of tangential loading.

The relationship between strains in the fingertip contact and afferent discharge were investigated for two afferents of class FA1 whose receptive field was within the contact. We found similarities between the response of the afferents and patterns of strain rates, especially with the rate of maximum compressive strains. Both units responded at the onset of the tangential loading, i.e. during the incipient slip phase and before the tangential force reached its plateau. These similarities between discharge and strain rates were observed only for the preferred stimulation direction of the two afferents. However, units responded also to stimulations in other directions, even if with a lower amplitude, despite the absence of strains in these conditions. Together, these results indicate that surface strains contributed to tactile afferent discharge but were not the sole cause of the discharge.

As exposed in the previous Chapter, the deformation of the finger pad under tangential loading is two-fold. Both forces, related to volume deformation, and surface strains, i.e. surface deformation, can create volume stress in the fingertip, which are known to be encoded by tactile afferents (Fig. 5.9). In short, both external forces and strains need to be taken into account to explain the discharge of the tactile afferents.

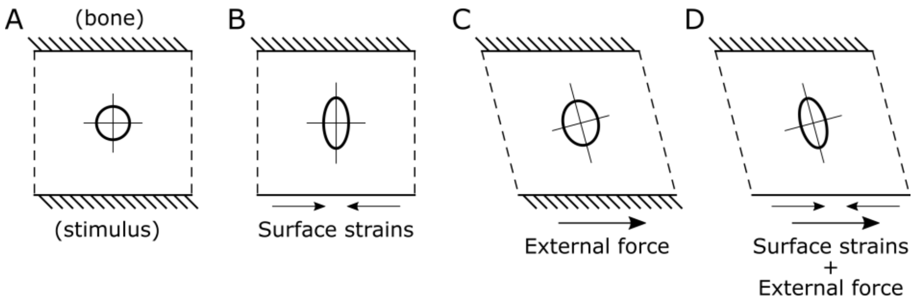

Fig. 5.9. Conceptual illustration of the potential causes of volume stress in the finger pad. (A) Finger pad section at rest. **(B–D)** Surface strains (B), external force (C) or a combination of both (D) can cause volume stress in the finger pad.

Due to the poor quality of recorded images, strain data from only two units have been presented here. To expand these results, it is critical to analyze data from more units with a better image segmentation algorithm. Therefore, we intend to apply the new algorithm described in Appendix C on the images from this study in order to improve the processing of fingerprint images.

5.5. Supplemental material

Mohr's circle is used in Fig. 5.10 to illustrate the relationship between axial and shearing strains in the case of plane strains, i.e. when out-of-surface strains are negligible. Principal strains e_1 and e_2 correspond to the value of the axial strains when the shearing strain is cancelled. Now, three possibilities remain as of the signs of the principal strains: (1) both are negative, i.e. a local patch of skin is compressed along both directions (Fig. 5.10A); (2) one is positive and the other is negative, i.e. skin is dilated along one direction and compressed along the other (Fig. 5.10B); (3) both are positive, i.e. skin is dilated along both directions (Fig. 5.10C).

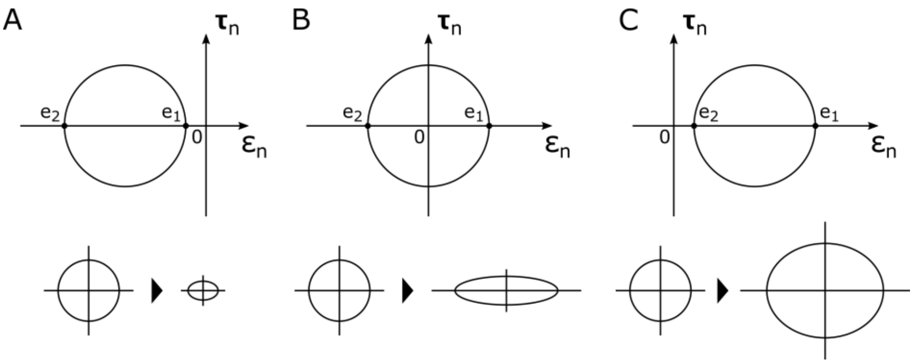

Fig. 5.10. Mohr's circles (shearing vs. axial strains) illustrating possible signs of principal strain components e_1 and e_2. (A) Both are negative, leading to a compression along the two orthogonal directions. **(B)** One is positive, the other is negative, leading to dilation along one axis and compression along the other. **(C)** Both are positive, leading to dilation along the two orthogonal directions. Each case is illustrated with the deformation of a circle.

Due to the high local stiffness of the outer layers of the fingertip skin (Wang and Hayward, 2007), it is reasonable to assume that the area of a local patch of skin is conserved after deformation. This implies that if one principal strain component is compressive, the other must be dilative. A simple demonstration comparing the area of a circle before and after deformation is presented below.

Let A_1 be the area of a circle of radius a: $A_1 = \pi a^2$. Let A_2 be the area of this circle after deformation acting along two orthogonal directions, transforming the circle into an ellipse. Let b and c be the radii of the ellipse, i.e. the length of its semi-major and semi-minor axes. We have $A_2 = \pi bc$.

Now, let us express b and c as a function is the radius of the circle before deformation: $b = a + \Delta x$ and $c = a + \Delta y$, with Δx and Δy not necessarily equal.

Finally, let us assume that the area of the circle and the ellipse are the same, so that the area is conserved after deformation. This implies that if $\Delta x > 0$, then $\Delta y < 0$ and vice-versa as shown below in equation (5.4).

$$\pi a^2 = A_1 = A_2 = \pi bc = \pi(a + \Delta x)(a + \Delta y) \qquad (5.4a)$$

$$\pi a^2 = \pi(a^2 + a\Delta x + a\Delta y + \Delta x \Delta y) \qquad (5.4b)$$

$$a\Delta x + a\Delta y + \Delta x \Delta y = 0 \qquad (5.4c)$$

$$a > 0 \; and \; \Delta x > 0 \; \Rightarrow \Delta y(a + \Delta x) < 0 \; \Rightarrow \Delta y < 0 \qquad (5.4d)$$

■

Principal strains being the relative deformation along two orthogonal axes, if one is positive, the other must be negative in order to conserve the area of the local patch of skin under deformation.

CHAPTER 6

General discussion and future directions

"Life is tough and then you graduate."

Jorge Cham (PHD Comics)

Finger pad mechanics plays a critical role in tactile exploration and dexterous manipulation by shaping the tactile feedback sent to the central nervous system by peripheral tactile afferents. This thesis addressed research questions related to the measurement of fingertip friction and to the role of partial slips in tactile perception and dexterous manipulation. This Chapter summarizes the main contributions, identifies future research questions arising from the contributions and their limitations, and discusses potential applications.

6.1. Summary of contributions

The minimum grip force needed to avoid object drop during manipulation is driven by the friction between fingertips and object. Due to the mechanical properties of the fingertip skin and the finger pad, the static coefficient of friction at the fingertip contact varies dramatically with grip force. Although fingertip friction has been shown to be encoded by the central nervous system (CNS) during manipulation and to be one of the key factors influencing the force control during precision grip, no method was available that allowed the static coefficient of friction to be measured quickly and reproducibly while capturing its dependence on the applied grip force. In Chapter 2, we proposed such a method and showed how it allows fingertip friction and therefore the safety margin to be estimated easily during manipulation. A Matlab implementation of this method accompanied by a graphical user interface is described in Appendix B. This method was designed to be applicable in a variety of environments, including in micro-gravity. It is currently used to measure fingertip friction in the GRIP experiment onboard the International Space Station. Additionally, it is used to teach biomedical engineering students about the motor control of object manipulation.

The coefficient of friction summarizes the mechanical interactions at the fingertip contact with a scalar quantity and therefore offers a global view of slippage. However, complex mechanical interactions arise at the fingertip-object contact under tangential loading of the fingertip. A very important phenomenon is the presence of localized slippage in the contact, also called *partial slip*. This phenomenon is due to the compliant nature of the finger pad and to the non-uniform pressure distribution within the contact. Under fingertip shearing, the periphery of the contact, where the pressure is lower than in its center, slips first. This slipping area grows towards the center of the contact with increasing tangential loading. As a result, local deformations, or strains, arise in the fingertip contact in a very reproducible pattern dependent on loading direction. These strain patterns at the surface of the skin are potentially captured by the numerous tactile afferents innervating the fingertips.

In view of the partial slip phenomenon, we conducted a study examining the perception of fingertip slip during the stick-to-slip transition on smooth surfaces, which was described in Chapter 3. We found that subjects perceived fingertip slip before full slip and we hypothesized that they relied on the smooth fingertip deformations to do so, as opposed to the vibration-based mechanism driving slip detection on rough surfaces proposed previously. This early slip detection may allow subjects to anticipate full slip between fingertips and object and thus it is relevant for object manipulation.

Therefore, in Chapter 4 we were interested in examining the dynamics of the fingertip contact during manipulation. To this end, we developed a novel manipulandum combining sensing of the forces applied to the object by the fingers and imaging of the fingertip contact. A preliminary study performed with the manipulandum was described, which highlighted the presence of a significant amount of partial slip at the fingertip contact during manipulation. This result opens the way for several research questions discussed in the next section.

Finally, in Chapter 5 we conducted a neurophysiological experiment to investigate how strain patterns caused by partial slips in the fingertip contact were encoded in the peripheral somatosensory system. In this experiment, we recorded *in vivo* the response of individual tactile afferents innervating the finger pad under fingertip shearing in conditions compatible with object manipulation. Due to the short time window available during recordings, transparent plates stimulating the fingertips could not be cleaned between trials, affecting image quality. Consequently, only a limited portion of the dataset was analyzed. In the future, we intend to test a new image processing algorithm developed within this thesis and described in Appendix C to overcome the problems related to image quality and therefore analyze more data from this study.

6.2. Future directions

In this section, we discuss new research questions raised by the results described in the previous section but also by their limitations. Research questions and future directions already discussed within the previous chapters are not restated here.

How to measure dynamic friction easily and how is it related to static friction?

The friction measurement method described in Chapter 2 allows experimenters to measure the static coefficient of friction between fingertips and object. This method is therefore only applicable when the static coefficient of friction is properly defined, i.e. when the tangential force drops at slip onset. As shown by measurements reported in Appendix A, this is not always the case. For instance, on smooth glass the tangential force increases smoothly and monotonically until reaching a plateau and it does not drop suddenly at slip onset. In these conditions, the static coefficient of friction is not properly defined and the only reproducible measure of friction between trials is the dynamic coefficient of friction, defined as the ratio of the tangential to the normal force during steady-state slippage. Therefore, several questions arise. First, is it possible to modify our method to measure friction on materials like smooth glass? Then, how is the dynamic coefficient of friction related to the static one? In particular, is dynamic friction also affected by normal force, as is static friction? A first answer to this question is provided by results reported in Appendix A, where we showed that the dynamic coefficient of friction varied with the normal force in the same way as the static one, i.e. following a negative power law. However, having a reliable measure of friction on materials like smooth glass requires the fingertip contact to be in steady-state slipping. Therefore, our friction measurement method based on short-range movements should be fundamentally revised and adapted to measure friction in these conditions. More work is therefore needed to develop a reliable method to measure dynamic friction easily and reproducibly with short-range movements.

What are the relative contributions to slip perception of volume vs. surface deformation of the fingertip?

In Chapter 3, we showed that subjects could rely either on surface deformations caused by partial slip, as measured with SR, or on volume deformations, related to the plate displacement during incipient slip, to detect fingertip slips. This result raises the question of the relative contributions of volume vs. surface deformation of the fingertip to the deformation-based slip detection mechanism. Addressing this question requires to assess separately the effect of volume and surface deformation on slip detection. To some extent, decoupling surface and volume deformation is possible with materials exhibiting different frictional properties. Indeed, the coefficient of friction impacts the relationship between SR and plate displacement. For a given displacement level, SR will fall faster with plate displacement, and therefore surface deformations will be lower, on a low-friction material than on a high-friction one. However, in practice it is difficult to find two materials with frictional properties similar to those of smooth glass but with different intrinsic friction levels. In Chapter 3, we tried to modify the friction of the glass plate by covering it with RainOff, but the reduction of friction was too strong so that it disrupted slip perception.

Another way to tune fingertip friction is to take advantage of its dependence on normal force and skin moisture (André et al., 2009). Namely, increasing the normal force will decrease the coefficient of friction. However one should be cautious because increasing the normal force will also increase the stiffness of the finger pad in a non-linear way, therefore potentially affecting mechanotransduction and thus the way stimuli are perceived. Another possibility is to modify the level of skin hydration. However, this is hard to control in practice because simply adding water to the fingertip contact does not have the same effect on friction as a natural increase of skin hydration induced by sweat.

Finally, to ease the measurements of slip detection thresholds, an adaptive psychophysical procedure could be used instead of the method of constant stimuli used in Chapter 3. The adaptive method rapidly converges to stimulus levels close to the subject's detection threshold and therefore it requires much less trials than the method of constant stimuli. However, it does not allow the experimenter to measure the sensitivity of the subject to the stimulus (Jones and Tan, 2013).

How does fingertip skin hydration influence slip perception?

Because fingertip skin hydration affects the friction at the fingertip contact (André et al., 2009), it also affects the relationship between SR and plate displacement, i.e. between surface and volume deformation of the fingertip as exposed above. Further analysis of data from Chapter 3 showed that fingertip skin hydration significantly influenced the mechanical behavior of the fingertip contact. Namely, an increase of fingertip moisture increased friction and thus the values of plate displacement and tangential force for which the contact entered full slip. However, the impact of moisture on slip detection thresholds was not clear. We believe that a dedicated study is needed to address the question of the impact of skin hydration on the perception of fingertip slip.

What are the relative contributions of skin vibration vs. fingertip deformation to slip perception during exploration of rough and smooth surfaces?

In Chapter 3, we discussed the existence of two complementary slip detection mechanisms: one based on vibrations generated in the skin by protrusions and texture of the stroking surface, which dominates slip perception on rough surfaces (Srinivasan et al., 1990), and another one based on finger pad deformations and allowing subjects to detect slip on smooth surfaces. We believe that these two mechanisms are not mutually exclusive because deformations of the fingertip also occur during exploration of rough surfaces and reciprocally, vibrations are also produced in the skin when exploring smooth surfaces. However, the relative contribution of vibrations vs. deformations to slip detection on rough and smooth surfaces is not clear. Therefore, it would be interesting to measure precisely the vibrations generated by a fingertip stroking a smooth plate, examine its frequency content, and investigate how this relates to surface deformations of the fingertip skin, i.e. partial slips, and how this affects slip perception. A previous study examining the tangential force during tactile exploration of two smooth materials (glass and PMMA) with different molecular structures but similar geometry found that the frequency content of the force differed during the incipient slip phase, which explained the capacity of subjects to discriminate between the two materials (Gueorguiev et al., 2016). This suggests that the frequency spectrum of the forces generated during exploration of smooth materials shapes tactile perception and thus potentially affects slip perception. Reciprocally, it would also be interesting to examine fingertip contact dynamics during exploration of rough surfaces and how this affects slip perception. However, it is more difficult to image the fingertip contact during exploration of non-smooth and non-transparent surfaces. Nevertheless, a recently developed device able to accurately record *in vivo* the interfacial forces produced when a finger interacts with an arbitrary surface could help address this question (Bochereau et al., 2017).

Are partial slips a generalization of the concept of safety margin during manipulation?

During object manipulation, grip force applied by the fingers on the objects is always kept above the minimum grip force preventing object drop. The *safety margin* is a measure of the difference between the applied and minimum grip force (Westling and Johansson, 1984). Tactile afferents have been shown to encode the safety margin for different frictional conditions (Johansson and Westling, 1984; Khamis et al., 2014b), but the underlying neural mechanisms are not clear. Partial slip of the fingertip contact, as measured with the stick ratio (SR), is a functionally relevant measure of the grip safety because preventing the object from falling is equivalent to avoiding slippage at the fingertip-object contact, i.e. maintaining SR > 0. In addition, SR is independent of the level of fingertip friction, and therefore it is not affected by the variation of friction with the applied grip force. Therefore, it would be interesting to examine to which extent the grip force modulation could be explained by the level of partial slip at the fingertip-object contact. This could shed light on the neural encoding of grip safety during manipulation.

What are the relative contributions of forces and torques at the fingertip contact to force coordination during manipulation and to fingertip contact dynamics?

Tactile afferents have the capacity to encode the magnitude and direction of tangential torques applied to the finger pad (Birznieks et al., 2010; Khamis et al., 2015). Additionally, inertial torque influences force coordination during manipulation and significantly reduces the grip force adaptation across lifting trials (Crevecoeur et al., 2011; Giard et al., 2015). Therefore, torques should be taken into account when investigating force coordination and adaptation during manipulation. Indeed, tangential torques applied by fingertips to counteract the torque caused by the mass distribution of an object contribute to grip safety in the same way as the grip force. A recent study proposed a generalization of the safety margin based on a contact model considering both forces and torques applied by the fingers to the object, and showed that this generalized safety margin offered a more faithful image of grip safety than the conventional safety margin based only on grip force (Singh and Ambike, 2017). In view of the potential role of partial slips as an index of grip safety, it would be interesting to examine the impact of tangential torque on fingertip contact dynamics.

What is the impact of skin vibrations and finger pad deformations on grip control?

Vibrations generated in the skin by sudden slips between fingertips and object have been shown to trigger grip force corrections during manipulation of a textured object (Johansson and Westling, 1987; Wiertlewski et al., 2013). This observation resonates with the importance for slip detection of vibrations produced in the skin during exploration of rough surfaces, therefore suggesting that the mechanisms of slip detection during tactile exploration discussed above are also relevant for the study of force coordination during manipulation. Therefore, it is worth investigating how skin vibrations and finger pad deformations contribute to force control during manipulation.

Why is the grip force modulated with the object load?

In anticipatory control of manipulation, grip force is modulated in phase with the object load (Flanagan and Wing, 1997; Wolpert and Flanagan, 2001).

If the only goal of the manipulation controller was to avoid dropping the object, grip force could be maintained at a high level regardless of the object load, thus guaranteeing a large safety margin. Therefore, the grip force modulation observed during manipulation reflects other control processes that are worth elucidating. For instance, the goal of the modulation could be to maintain a given level of partial slip at the fingertip contact in order to facilitate knowledge of object dynamics and therefore enhance skilled manipulation (Witney et al., 2004). In the same idea, it is also possible that grip force modulation is performed to improve the sensitivity of the skin. Indeed, the skin is less sensitive when compressed because a given force variation at a high force level will create less deformation and thus potentially less modulation in the response of tactile afferents than at a low force level.

How is friction encoded by the tactile system?

Mechanically speaking, friction is at the heart of tactile interactions. Indeed, it is influenced by the normal force and skin moisture (André et al., 2009), and in turn it drives the relationship between partial slip at the fingertip contact and tangential force, and also the relationship between partial slip and fingertip displacement (André et al., 2011). There is evidence that fingertip friction is encoded by the tactile system quickly after initial contact with an object (Johansson and Westling, 1984; Khamis et al., 2014a). However, the mechanisms by which the CNS estimates fingertip friction at initial contact, but also continuously during object manipulation or tactile exploration, are not clear. Given their dependence on local frictional properties of the fingertip contact, partial slips and surface strains in the contact may play a significant role in friction encoding. The question of friction encoding by the CNS is inherently complex and involves finger pad mechanics as well as control of movement during tactile exploration. It shapes tactile perception of explored surfaces and plays an important role during object manipulation. In short, it is related to all topics addressed in the present thesis.

Recently, techniques have been developed that offer the possibility to quickly modulate the friction of a surface without affecting its other properties such as texture (see next section). A very exciting experiment would be to perturb friction during manipulation using these friction modulation techniques and check for a motor response in the muscles involved in grip control. This would allow researchers to causally test whether friction is taken into account in the modulation of the grip force and shed new light on how friction is encoded by the tactile system.

6.3. Applications

Despite being fundamental in nature, this work is not without several potential applications, which are summarized here.

Design of somatosensory neuroprostheses

Tactile feedback is essential for fine motor control and, more generally, shapes our fundamental perception of the world. Therefore, a hand loss is a highly disabling event that markedly affects the quality of life. Despite increasingly sophisticated mechatronics, prosthetic devices often do not directly convey sensation back to their wearers. Recent studies developed somatosensory feedback systems through peripheral (Graczyk et al., 2016; Raspopovic et al., 2014; Tan et al., 2014) or central neurostimulation (Flesher et al., 2016) and combined them with conventional hand prostheses, therefore restoring tactile sensation during object manipulation to amputees. Studying how a given mechanical stimulation gives rise to neural responses in tactile afferents helps researchers to develop electrical stimulation patterns that are close to the ones elicited naturally during tactile interactions.

Design of rich tactile displays

A new generation of tactile interfaces offers the possibility to modulate the friction between the fingertip and the surface dynamically. Friction can be increased through electrovibration (Shultz et al., 2017; Vardar et al., 2017) or decreased through ultrasonic vibration (Wiertlewski et al., 2016), and these two technologies can be combined into a single tactile display (Vezzoli et al., 2015). Both technologies have in common that the friction modulation is perceived only when the fingertip is moved across the surface. Therefore, a better understanding of the dynamics of the finger pad under tangential loading, and of the physical factors shaping fingertip slip perception is relevant to better characterize tactile interactions on these friction-modulation surfaces.

Design of haptic feedback systems for virtual reality and robotic teleoperation

Tactile sensation plays an important role in haptic feedback. A broad area of research is concerned with the design of intuitive and efficient haptic feedback systems, namely for virtual reality and teleoperation applications.

However, due to the complexity of measuring and reproducing tactile interactions, tactile stimulations are often lacking in those systems (Pacchierotti et al., 2016; Webster et al., 2005). By providing a better understanding of tactile interactions through the study of slip perception, the results of this thesis are applicable to design better haptic feedback systems.

Design of robotic hands

Identifying the critical parameters relevant for tactile perception and dexterous manipulation is needed to design efficient robotic manipulators that will be able to sense and make sense of their environment with a higher degree of accuracy. Taking inspiration from the impressive human manipulation abilities will help roboticists to develop new robotic hands that are more robust and flexible. For example, the complex and specific strain patterns at the surface of the fingertip skin in contact with an object inspired the design of a new generation of soft robotic fingers (Ho and Hirai, 2014).

APPENDIX A

Characterizing friction of a selection of smooth transparent materials

A.1. Motivations

This Appendix presents the results of friction measurements between human fingertips and a selection of smooth transparent materials with the aim of helping researchers to select the appropriate materials for experiments involving fingertip-surface interactions.

A.2. Methods

A.2.1. Tested materials

The selected materials were hard, smooth, i.e. they did not feel rough during tactile exploration, and transparent, so that the fingertip contact can be imaged through them. We also added two non-transparent and non-smooth materials, namely silk and suede, which were used in the seminal study from Johansson and Westling (Johansson and Westling, 1984) and very often since then in order to compare the friction measurements with standard materials from the literature. Below is the list of the nine tested materials:

- **Bulk materials**
    - Glass
    - Acrylic
- **Coatings**
    - Varnish
    - Screen cover

  - PP
  - PET
  - RainOff
- **Non-transparent materials**
  - Silk
  - Suede

The coatings were applied on glass plates and the non-transparent materials were put on wooden plates, therefore always having hard surfaces in contact with the fingertips. The varnish is a protective coating to be sprayed on objects and designed for hobbyists. The screen cover is a commercially-available scratch-resistant protection for the screens of tablets and smartphones. PP and PET are commercially-available auto-adhesive and transparent protective coatings. RainOff is a hydrophobic coating produced by Arexons, a division of Petronas Lubricants, Villastellone TO, Italy. It is designed to repel water on car windshields. Interestingly, it allows reducing the fingertip contact friction while being highly transparent and therefore not altering the quality of the fingerprint images recorded through the glass.

A.2.2. Apparatus and data collection

We used the robotic platform described in Chapter 3 to perform the measurements. The robot was controlled to keep a constant force in the direction normal to the contact and a constant speed tangentially to the contact. Given the influence of normal force (NF) on fingertip contact friction (Adams et al., 2013; André et al., 2009) (also demonstrated in Chapter 2), we tested three normal forces relevant for tactile exploration and object manipulation, namely 2N, 5N and 10N.

Four subjects participated in the experiment. They exhibited different skin hydration levels ranging from dry to very wet. For each trial, the robot loaded the tested material normally to the right index fingertip of the subject until reaching the prescribed normal force. Then, keeping the normal force constant, the plate was moved tangentially to the contact in the radial direction, i.e. towards the thumb of the subject, at a constant speed of 5mm/s on a distance of 50mm. Finally, the plate was moved away from the fingertip. Each condition was repeated five times, totalizing 135 trials per subject (5 repetitions x 3 NF levels x 9 materials). Force exerted by the fingertip on the plate and position of the plate were recorded at 1kHz during the trials.

A.2.3. Data processing

The dynamic coefficient of friction was computed for each trial as the ratio of the tangential to the normal force (TF/NF) during plateau of the tangential force. More precisely, we computed the average TF/NF ratio during the time period ranging from 5s to 8s after the onset of the tangential movement of the plate, which corresponded to a plate displacement ranging from 25mm to 40mm. Data were processed using Matlab.

A.3. Results

Figures A.1 to A.3 present the friction measured for NF = 2N, 5N, and 10N, respectively. Figure A.4 regroup all measurements and shows that the dynamic friction coefficient decreases with increasing NF, as is the case with the static coefficient of friction.

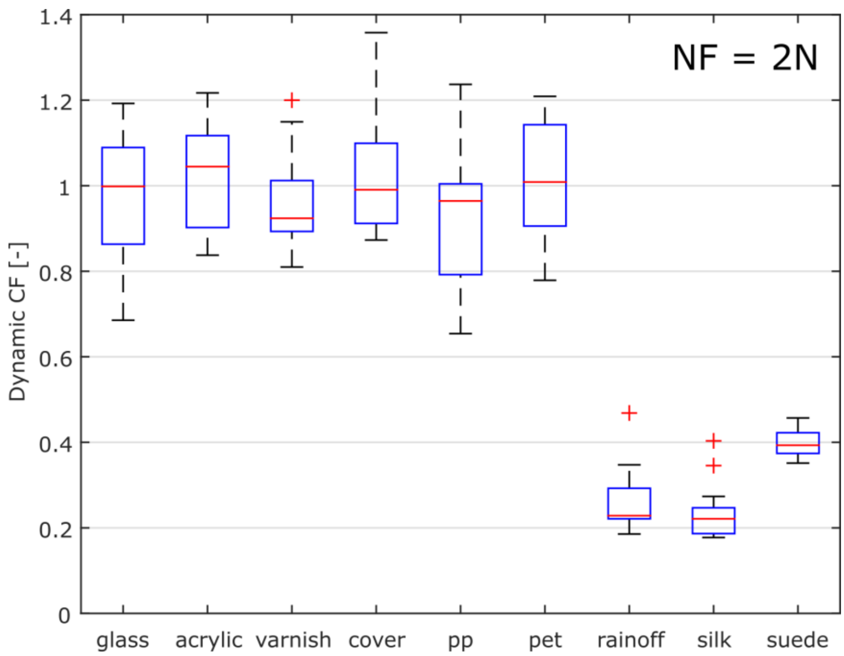

Fig. A.1. Dynamic coefficient of friction between fingertip and the nine tested materials with NF = 2N.

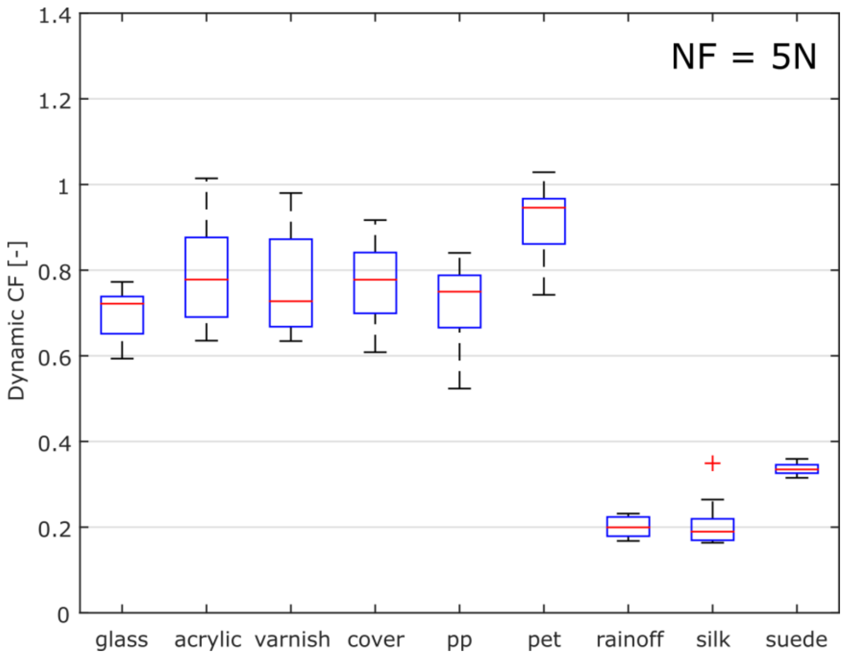

Fig. A.2. Dynamic coefficient of friction between fingertip and the nine tested materials with NF = 5N.

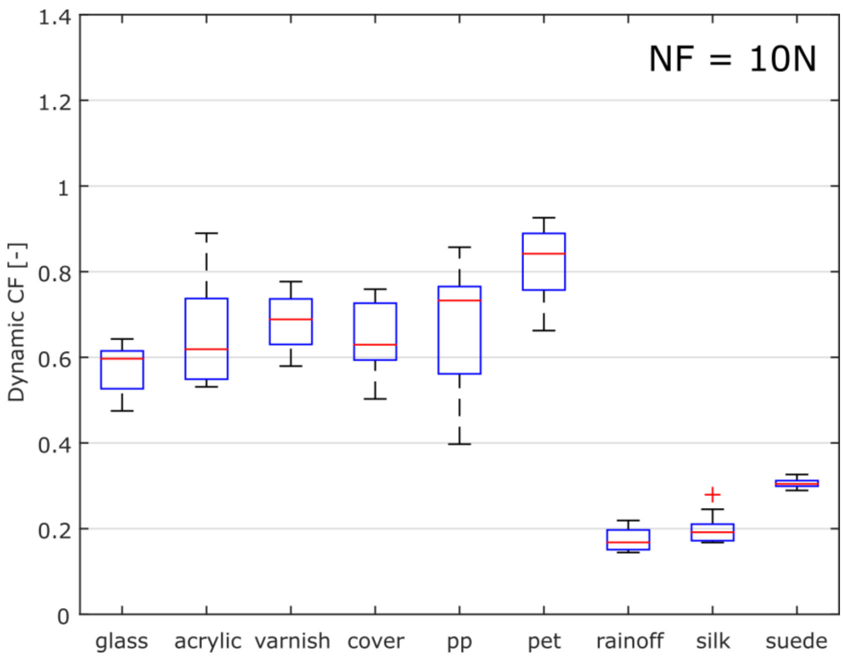

Fig. A.3. Dynamic coefficient of friction between fingertip and the nine tested materials with NF = 10N.

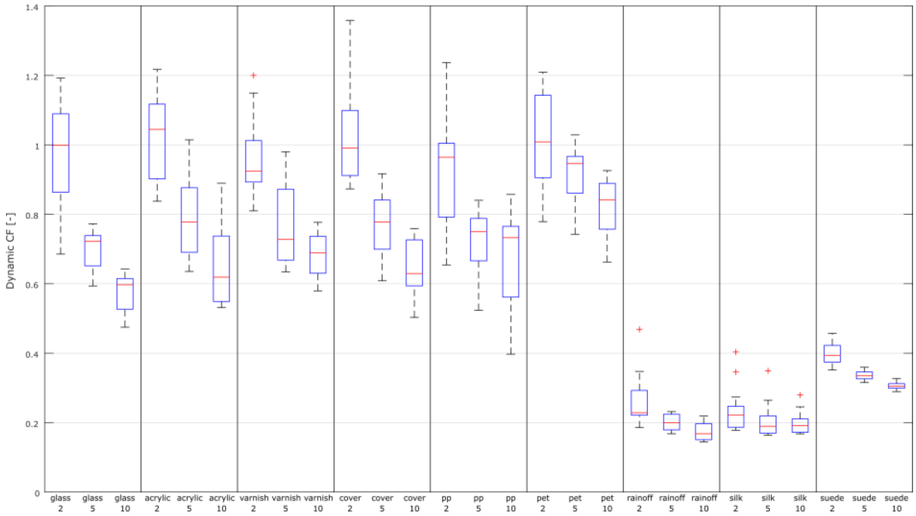

Fig. A.4. Summary of all measurements for the nine materials and the three levels of NF: 2N, 5N, and 10N.

A.4. Comments and recommendations

The static coefficient of friction is defined as the ratio of the tangential to the normal force (TF/NF) at slip onset (Chapter 2). On rough materials, slip onset is accompanied by a sudden decrease of the tangential force (TF). However, we often observed here that TF increased smoothly with plate displacement until reaching a plateau, with no sudden drop of TF nor of the TF/NF ratio. The Supplemental Data section below displays the time evolution of TF/NF for individual subjects. Overall, this means that the static coefficient of friction is not properly defined for most of the smooth materials tested here. However, for the two non-transparent materials, TF dropped shortly after the onset of the tangential displacement of the plate, therefore allowing a proper definition of the static coefficient of friction.

Besides, on some trials, the finger exhibited a stick-and-slip behavior when stroked by the plate, i.e. short and jerky motions caused by alternate sticking from friction and sliding when the friction is overcome by the tangential force applied by the stroking plate. This stick-and-slip phenomenon was observed on varnish and, to a lesser extent, on PP, PET, and acrylic. Detailed inspection of the data and previous testing not reported here reveal that the stick-and-slip phenomenon is influenced both by skin hydration and by NF. It seems to occur preferentially for dry skin and large

NF. However, the influence of NF actually depends on the material used. In general, stick-and-slip is a complex phenomenon that depends on many factors including roughness and relative velocity of the two surfaces in contact (Bengisu and Akay, 1999; Liu, 2012). A detailed study of the parameters influencing stick-and-slip at the fingertip contact would be valuable to better understand the fundamental mechanics of tactile interactions but is beyond the scope of this text. Here, we simply report whether or not stick-and-slip occurred with the different tested materials. Our observations are summarized in Table A.1.

Table A.1. Summary of observations made on the different materials. The presence of a static coefficient of friction (CF) means that a decrease of the TF/NF ratio was observed shortly after the onset of the tangential movement of the plate, indicating slip onset. In addition, the presence of stick-and-slip in the time evolution of the forces is reported.

Material	Static CF?	Stick-and-slip?	Comments
Glass	No	No	-
Acrylic	No	Sometimes	Frictional behavior similar to glass.
Varnish	**Yes**	**Yes**	Stick-and-slip occurs almost systematically.
Cover	No	No	Frictional behavior similar to glass.
PP	**Yes**	**Yes**	-
PET	No	Sometimes	Similar to screen cover, but with more stick-and-slip.
RainOff	No	No	Low friction, highly reproducible stimuli.
Silk	**Yes**	No	Low friction, highly reproducible stimuli, very clear static CF.
Suede	**Yes**	No	Low friction, highly reproducible stimuli, very clear static CF.

We observed that dynamic friction systematically decreased with increasing normal force, and sometimes dramatically, as is the case with static friction (Chapter 2). This dependence must be taken into account when selecting materials for a given experiment and researchers must determine carefully what normal force will be applied at the fingertip contact during experiments. In addition, the exerted normal force should be controlled and kept constant during the trials in order to ensure reproducible stimuli across trials.

The materials exhibited either a low friction (for RainOff, silk, and suede) or a high friction (for the rest of them), with no tested material exhibiting an intermediate friction level. The low-friction materials were the ones with the highest reproducibility across trials. Besides, the influence of NF on the dynamic coefficient of friction was more dramatic for the high-friction materials than for the low-friction ones.

The dynamic coefficient of friction of acrylic was very similar to the one of glass, as already observed in a previous study (Gueorguiev et al. 2016). The friction behavior of the screen cover was also very similar to the one of glass, with no static friction, no stick-and-slip, and approximately the same friction values at the different levels of NF (Fig. A.4). Screen cover offers the following benefits: (1) scratch resistant and highly transparent; (2) designed to prevent deposition of sweat and grease from the fingertip. Together, these features ensure a good quality of fingerprint images by limiting the parasitic elements such as tiny scratches or fingerprint artifacts left on the surface after previous strokes. In addition, reducing sweat and grease deposition also limits the variation of the moisture content at the surface of the skin during strokes, therefore improving reproducibility of stimuli.

A.5. Supplemental data

Figures A.5 to A.8 show the time evolution of the TF/NF ratio for the four subjects individually.

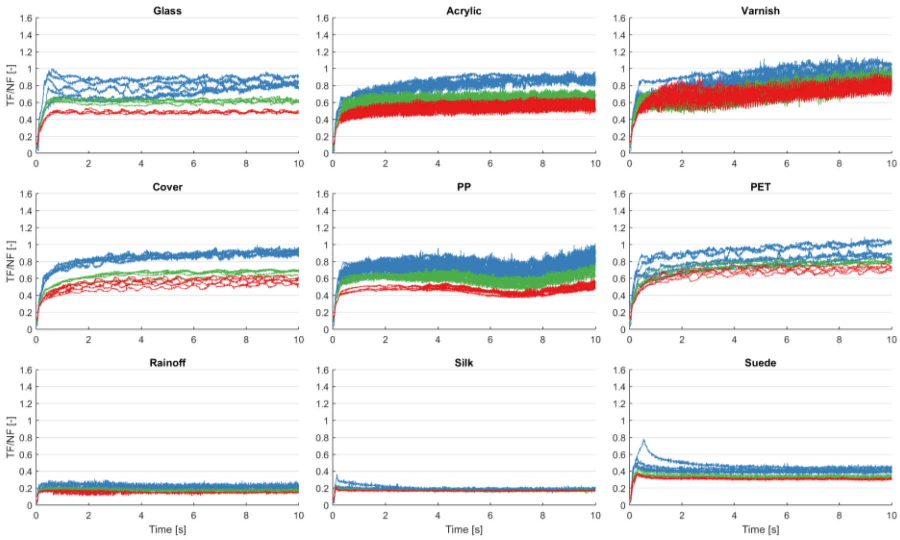

Fig. A.5. Time evolution of TF/NF for subject AB, for NF = 2N (blue), NF = 5N (green) and NF = 10N (red). The subject had a rater dry fingertip skin.

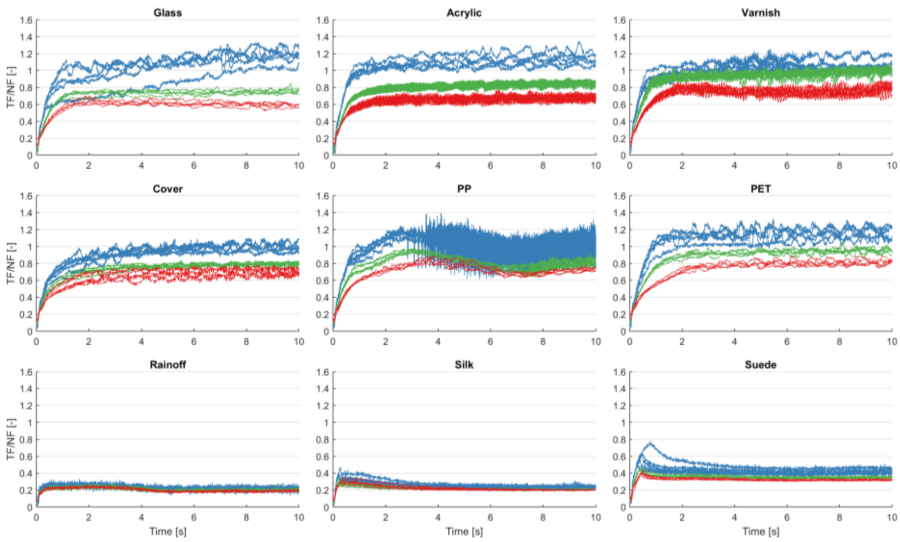

Fig. A.6. Time evolution of TF/NF for subject OC, for NF = 2N (blue), NF = 5N (green) and NF = 10N (red). The subject exhibited an average level of skin hydration.

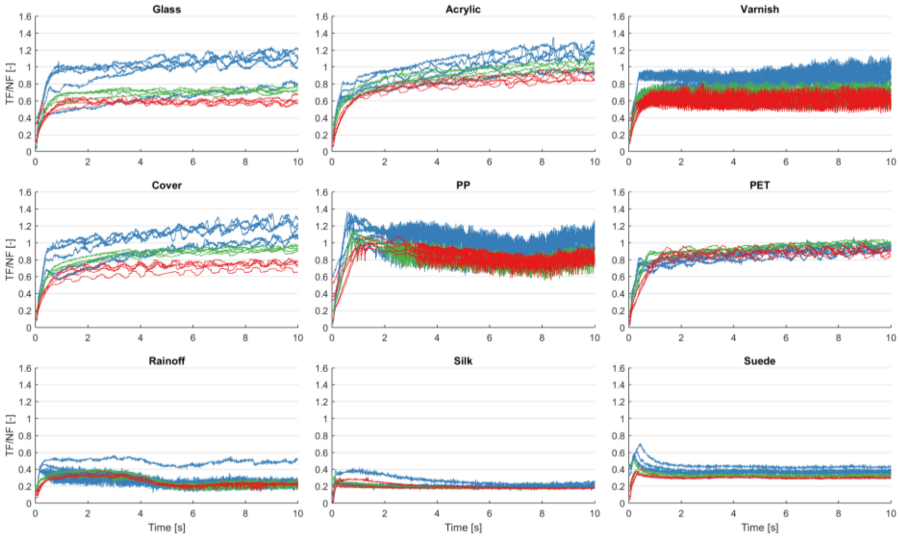

Fig. A.7. Time evolution of TF/NF for subject LO, for NF = 2N (blue), NF = 5N (green) and NF = 10N (red). The subject had a rather wet fingertip skin.

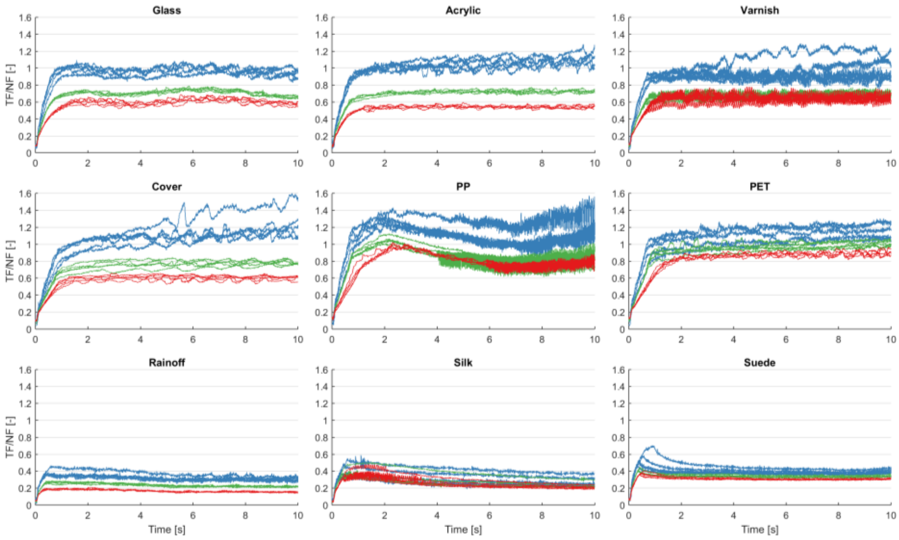

Fig. A.8. Time evolution of TF/NF for subject FS, for NF = 2N (blue), NF = 5N (green) and NF = 10N (red). The subject had a naturally very damp skin.

APPENDIX B

ASMC User's Guide

Published as Supplemental Material of: A. Barrea*, D. Cordova Bulens*, P. Lefèvre and J.-L. Thonnard, "Simple and Reliable Method to Estimate the Fingertip Static Coefficient of Friction in Precision Grip," in IEEE Transactions on Haptics, vol. 9, no. 4, pp. 492-498, Oct.-Dec. 2016. (*) equal contribution.

B.1. Introduction

ASMC (A Simple Measure of the Coefficient of friction) is an algorithm designed to compute the static coefficient of friction at the fingertip-object contact from the forces and torques measured by a six-axis force/torque sensor. This user's guide provides step-by-step explanations to prepare data, analyze it and visualize and export the results. This user's guide is intended as a complement to the paper describing the method. Please read the paper before reading this guide. The algorithm has been tested with Matlab R2013a and Matlab R2015a running on Windows 7.

B.1.1. Abbreviations used in this guide and in the code

Abbreviation	Meaning
TF	Tangential force
NF	Normal force
µ (sometimes noted "mu")	**Static** coefficient of friction, defined as TF/NF at slip onset

B.1.2. Inputs

ASMC needs the following data in order to carry out the analysis:

- The normal force (NF) exerted by the finger on the force sensor;
- The tangential force (TF) exerted by the finger on the force sensor;
- The center of pressure (COP) position of the finger on the sensor (cf. formula in appendix);
- The size of the sensor;
- The minimum accepted values of TF and NF (see explanations below);
- The position of the thresholds on the sensor (thresholds are defined below).

B.2. Before using the ASMC algorithm

ASMC runs on a project folder that must contain all data files that will be analyzed. Each data file must be named using the following convention: "*<subject>*_*<condition>*.csv". The data files must only contain five columns of data corresponding to F_x, F_y, F_z, COP_x and COP_y, respectively. F_x, F_y and F_z correspond to the forces measured by the force sensor along the x-, y- and z-axis, respectively. COP_x and COP_y are the COP position along the x- and y-axis respectively. See appendix to know how to compute COP from force and torque data. Each row of a data file corresponds to a single time step. The accepted file extensions for the data files are "*.lvm*", "*.csv*", "*.txt*" and "*.tsv*".

B.3. Using ASMC

To start, run "asmc.m". This opens the main window (see Fig. B.1). From this window, the user can **import** new data, **process** previously imported data or **plot** analyzed data, with the corresponding buttons.

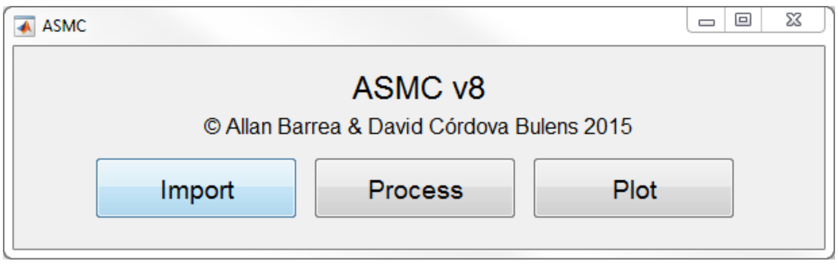

Fig. B.1. ASMC main window.

B.3.1. Import window

Clicking on the "Import" button of the main window opens the **Import window** (see Fig. B.2). The project folder that contains the data to be imported can be selected using the "Browse" button on the top right corner of this window. Once the project folder has been selected, its full path appears on the text box at the top of the window. Clicking on the "Import data from…" button starts data import. Once the data import is over, a message indicating whether the import was successful or not is displayed in the lower text box (see Fig. B.3).

The import process outputs a file called "*<project_folder_name>_data.mat*" into the project folder. This file contains a structure organized as presented in Fig. B.4.

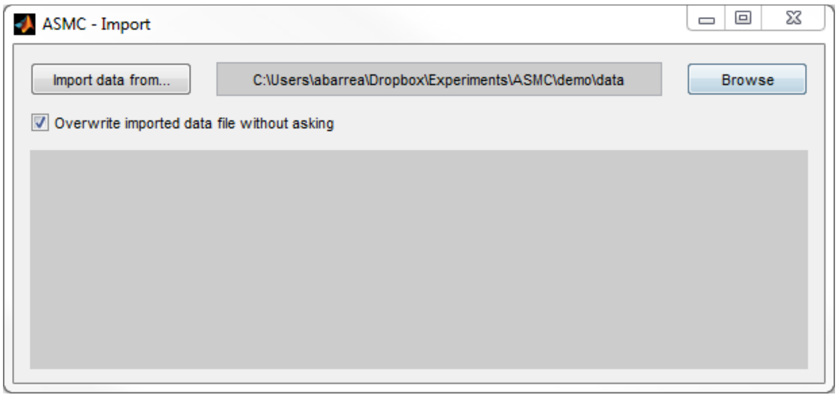

Fig. B.2. Import window.

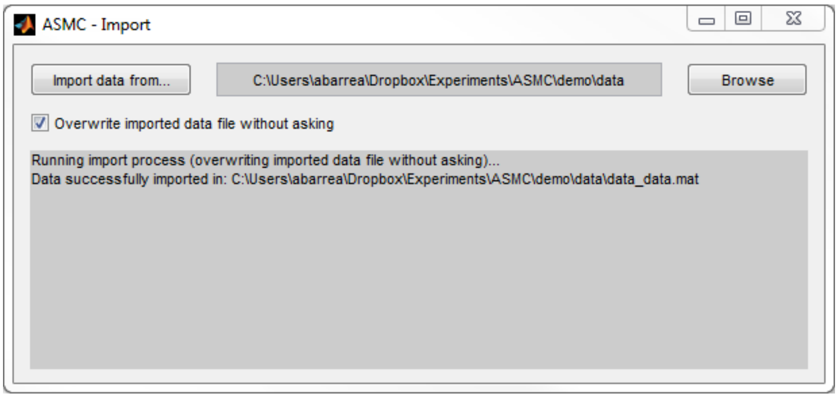

Fig. B.3. Import window after data import. Once data is imported, a message is displayed in the lower part of the window.

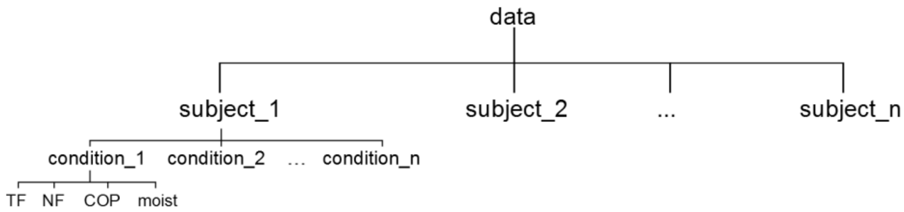

Fig. B.4. Imported data file structure. The imported data file is a structure that contains a field for each subject. In turn, each subject has fields with structures containing data for each condition.

B.3.2. Process window

The **Process window** (see Fig. B.5) allows the user to configure and run the analysis. As for the import, the project folder must be selected using the "Browse" button before running the analysis.

The analysis can be configured using the textboxes presented in the "Configuration parameters" box. Here, the user can define the sensor limits and the movement direction. Clicking on the "Advanced settings" button opens the **Advanced settings window** (see Fig. B.6) that allows for further configuration of the analysis. The following parameters can be adjusted in this window:

- Position of the thresholds as a percentage of the sensor size;
- Use of extrema in TF or in TF/NF to search for slip onsets;
- Type of movements performed during the experiment (full or half sensor range);
- Number of standard deviations allowed before considering a data point as an outlier;
- Maximum deviation allowed from the straight movement. If the movement amplitude in the direction orthogonal to movement direction exceeds this value, the individual movement will be considered tilted and will not be included in the results;
- Minimum NF needed to consider contact between the sensor and subject's finger;
- Minimum TF needed to consider contact between the sensor and subject's finger.

Once all the settings in the Advanced settings window are set, click the "OK" button to save these settings. Back in the Process window, the "General parameters" box allows the user to select whether or not to automatically overwrite any already existing results file in the project folder. You can also select whether to display the processing report or not. The processing report will be explained further in this document.

After configuring the analysis, the user can save the configuration in the project folder. To do so, the user must write a name in the "Config file name" text box and click on the "Save configuration file" button. The outputted file has the "*.asmc*" extension. If a configuration file already exists in the project folder it can be loaded by typing its name in the text box and clicking the "Load" button.

Clicking on the "Process" button launches the data analysis. At the end of the analysis a results file is saved in the project folder. This file is named "*<project_folder_name>_results.mat*". It contains a structure named "*results*" and is organized as presented in Fig. B.7.

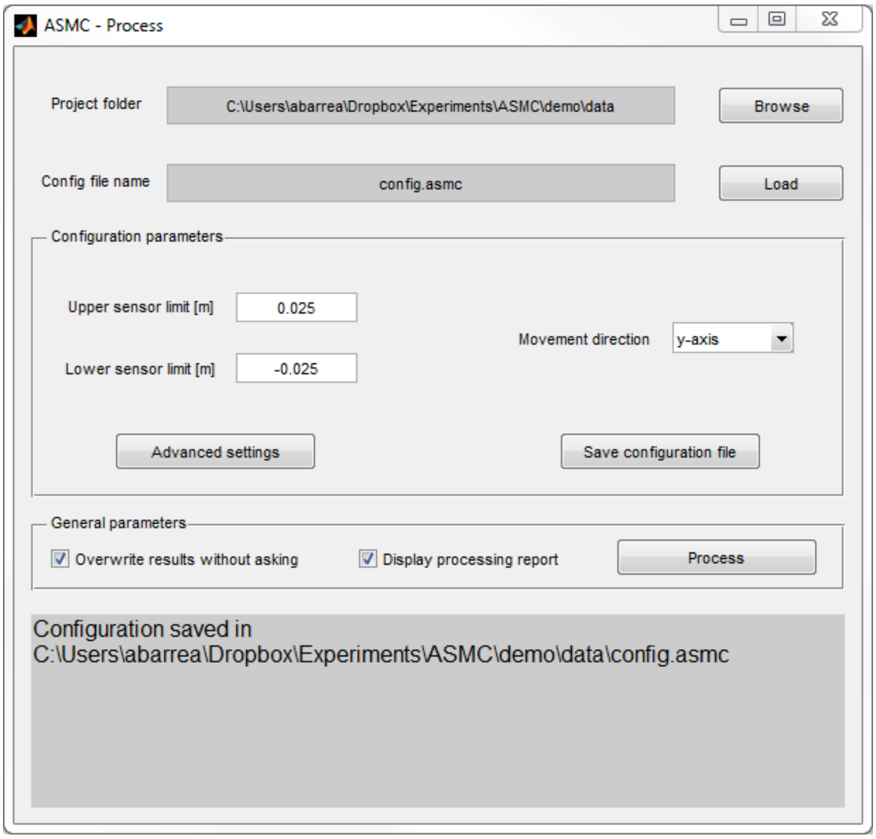

Fig. B.5. Process window.

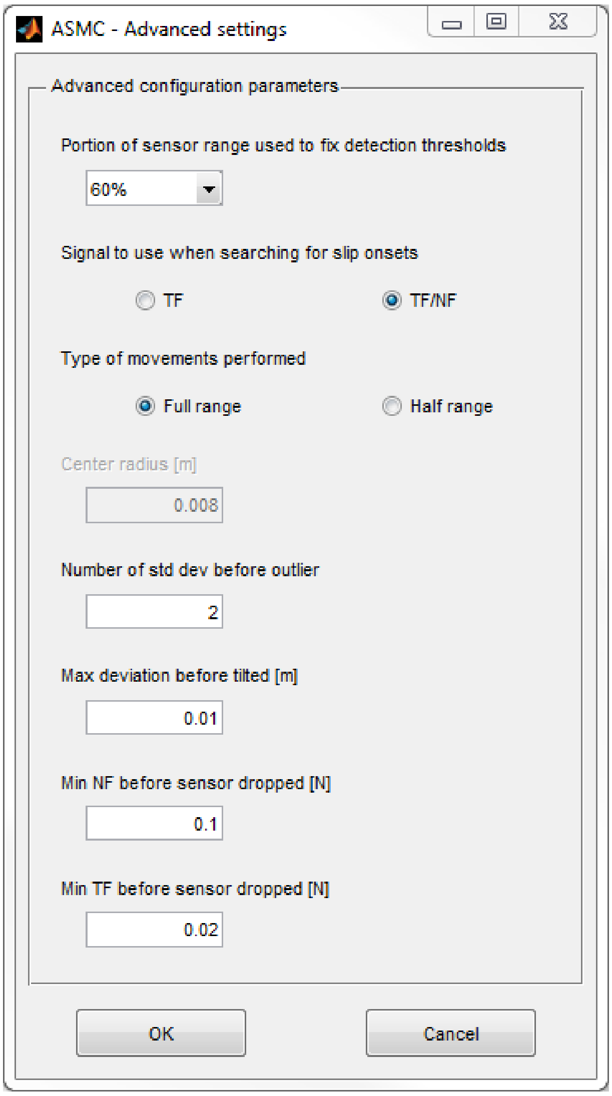

Fig. B.6. Advanced settings window.

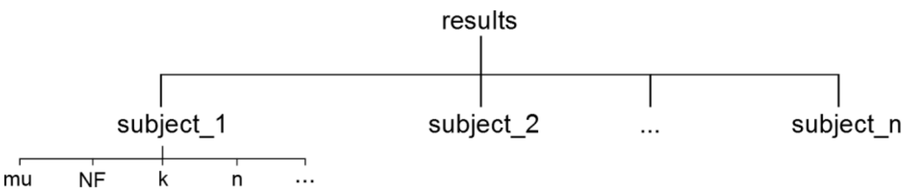

Fig. B.7. Structure obtained at the end of ASMC process. The results file is a structure that contains a field for each subject. In turn, each subject has fields with computed data.

B.3.3. Report window

The **Report window** (see Fig. B.8) automatically pops up if you checked the "Display processing report" checkbox in the process GUI. It allows the user to check data analyzed by the ASMC algorithm. In this window, the user can select the subject(s) and the condition(s) he or she wishes to visualize, once the subject(s) and condition(s) are selected, click the "Print" button to visualize the data process.

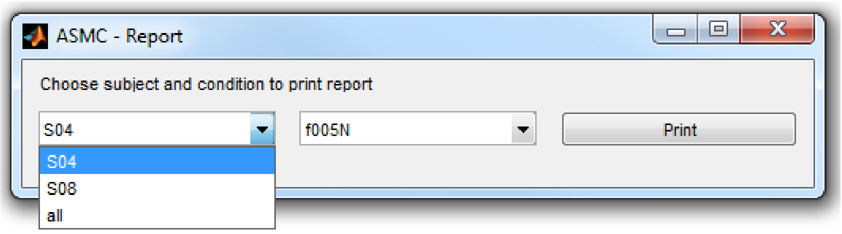

Fig. B.8. Report window.

When the "Print" button is pressed, two windows open up for each selected subject and condition. The first one, presented in Fig. B.9, shows the COP trajectory. The left panel shows the COP trajectory on the sensor. In the right panel, this trajectory is decomposed into the component selected as the movement direction (here COP_y, i.e. along the y-axis) and the component in the orthogonal direction (here COP_x, i.e. along the x-axis). Furthermore, each plot displays raw data (dark gray lines), filtered data (blue or green lines), useful zones (in white) and rejected zones (in light gray). Some useful zones are sometimes rejected; in that case they are either displayed in **red** (indicating an outlier value of µ) or in **orange** (indicating a tilted movement). Each of these elements can be set visible or invisible using the checkboxes at the bottom of the window. In addition, red lines indicate the sensor limits and the dotted horizontal black lines indicate the detection threshold in the movement direction (here COP_y) and the tilt threshold in the orthogonal direction (here COP_x).

The second window (see Fig. B.10) displays information about NF, TF and µ. We recall that µ is defined as TF/NF at slip onsets, indicated by the red dots. Again, raw COP trajectory is displayed with dark gray lines and filtered COP trajectory in the movement direction with blue lines. Useful and rejected zones are displayed using the same color code as described above.

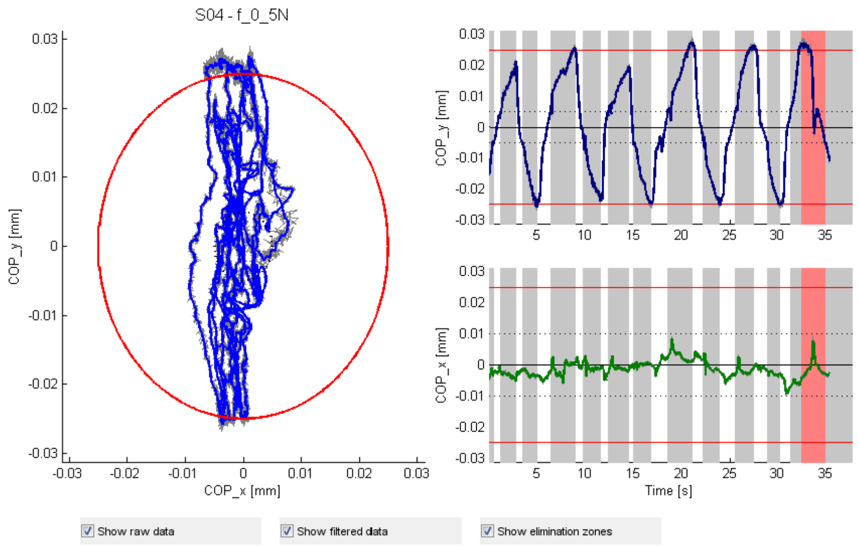

Fig. B.9. COP visualization window.

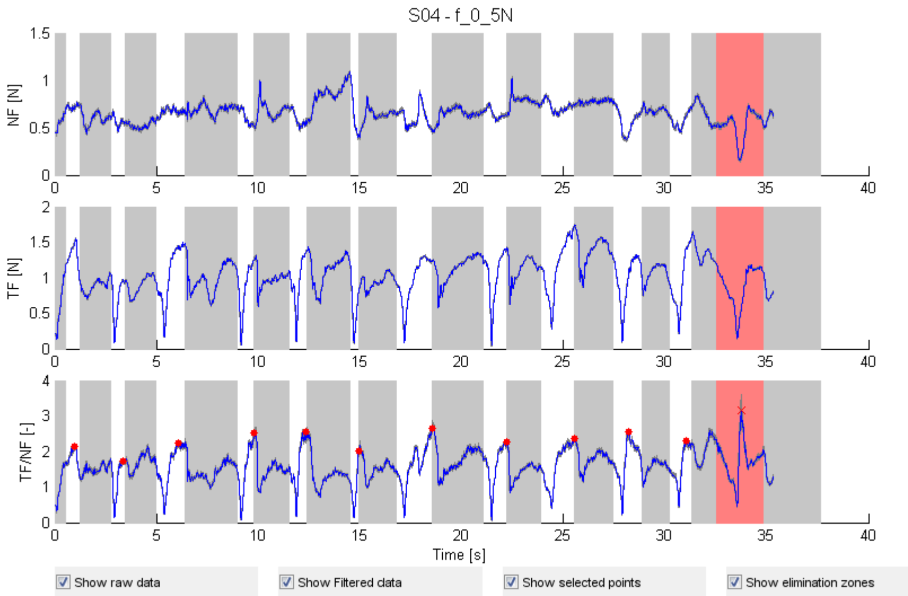

Fig. B.10. Forces visualization window. The zone in red is rejected because it contains an outlier value of μ, which is therefore denoted by a red cross instead of a red dot.

B.3.4. Plot window

The **Plot window** (see Fig. B.11) allows the user to plot the results of the ASMC analysis. First, the user must select the results file he or she wishes to visualize using the "Browse" button. When a results file is selected, data for the various subjects contained in this file are shown in the "Select results to plot" box. The user can choose which data to plot by selecting it in the "Select results to plot" box and clicking on the ">>" button. Only subjects that are moved to the "Results to plot" box will be plotted. Subjects can be moved back from the "Results to plot" box by clicking on the "<<" button. Clicking on the "Print" button displays the selected plots.

Various checkboxes allow the user to further parametrize the plots. By default, data from all subjects are plotted into a single figure but in different subplots. If several results files containing identical subject names are loaded, the user can plot all the data of a single subject in the same subplot by checking the "Plot subjects together" checkbox. The "Plot all data together" checkbox allows the user to plot all data in a single plot. The "Plot each graph in a separate figure" checkbox allows plotting each subject's data on a different figure. If the "Save figures" check box is checked, all figures are saved into the folder specified in the "Directory to save figures" textbox. This folder can be changed by the user.

A plot example is presented in Fig. B.12. In this figure, the dots represent the measured μ values and the solid line represents the model fitted to the data.

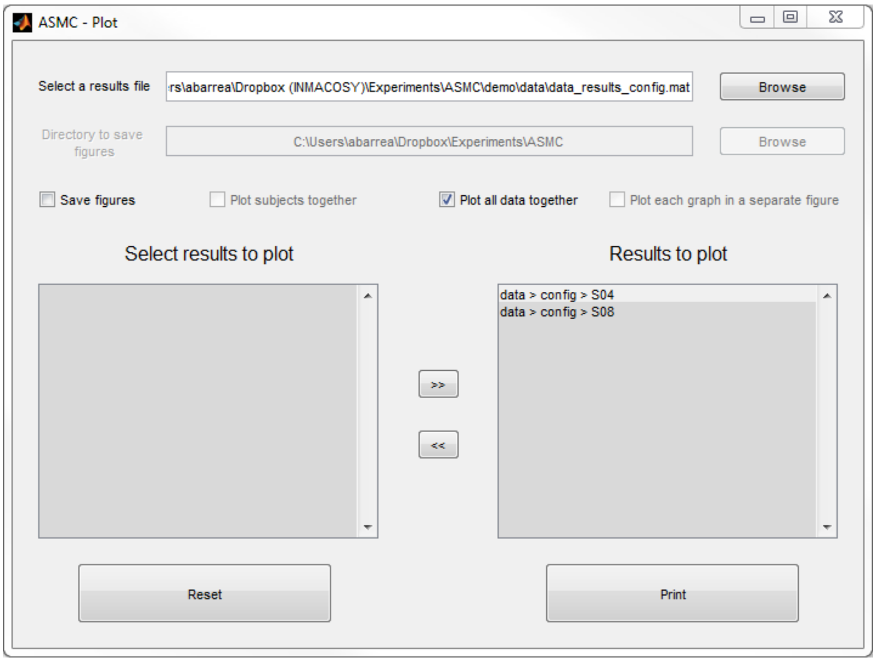

Fig. B.11. Plot window.

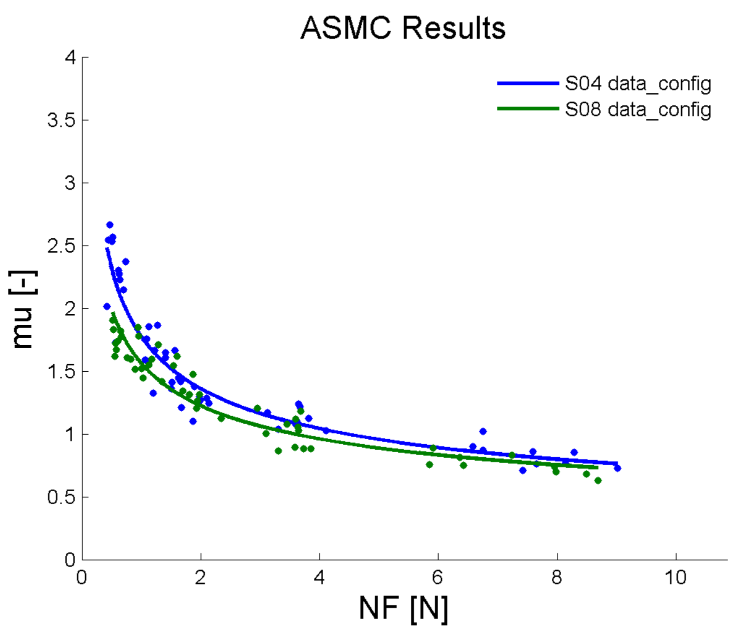

Fig. B.12. Relationship between μ and NF. The dots represent the measured μ values. The lines represent the fitted model $\mu = k \cdot (NF)^{n-1}$ (see paper for further explanations of this model).

B.4. Computing COP location from force and torque data

The calculated Center of Pressure (COP) coordinates (x,y) of a point force applied to a force/torque sensor are as follows:

$$COP_x = \frac{M_y + F_x z_0}{F_z} \qquad\qquad COP_y = -\frac{M_x - F_y z_0}{F_z}$$

COP_x, COP_y	x- and y-coordinates of the center of pressure
z_0	Distance from sensor's surface to ref. frame's origin
F_x, F_y, F_z	Force along the x-, y- and z-axis
M_x, M_y	Torque about the x- and y-axis

Proof

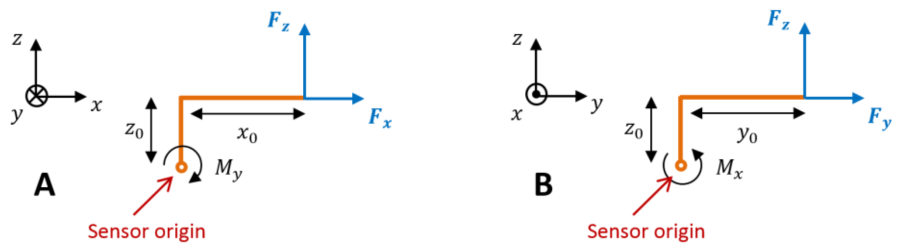

Computing COP_x (case A)

$$\Sigma\, Torques\ about\ y = 0 \;\Rightarrow M_y - F_z x_0 + F_x z_0 = 0 \;\Rightarrow x_0 = \frac{M_y + F_x z_0}{F_z}$$

Computing COP_y (case B)

$$\Sigma\, Torques\ about\ x = 0 \;\Rightarrow M_x + F_z y_0 - F_y z_0 = 0 \;\Rightarrow y_0 = -\frac{M_x - F_y z_0}{F_z}$$

Conclusion

If $z_0 \neq 0$, then tangential forces (F_x, F_y) influence COP measure:

$$COP_x = x_0 = \frac{M_y + F_x z_0}{F_z} \qquad COP_y = y_0 = -\frac{M_x - F_y z_0}{F_z} \qquad COP_z = z_0$$

If $z_0 = 0$, then the above expressions simplify:

$$COP_x = \frac{M_y}{F_z} \qquad COP_y = \frac{-M_x}{F_z} \qquad COP_z = 0$$

APPENDIX C

Software tools for fingerprint image analysis

Software tools have been developed in Matlab to analyze the images of the fingertip contact. They are acquired as high-resolution gray-level images, where fingerprints contacting the countersurface are enhanced by an optical method based on Frustrated Total Internal Reflection (FTIR). First, a new image segmentation algorithm is described, that allows an automatic detection of the contour of the contact. This algorithm is part of the *imagetools* toolbox, which is presented next. Finally, the *libactivetouch* toolbox is introduced, which contains analysis code dedicated to the ActiveTouch manipulandum presented in Chapter 4. The software described here accompanies the thesis.

C.1. Automatic segmentation of the fingertip contact

A new image segmentation algorithm has been developed to detect the contour of the fingertip contact automatically on these images. This contour encloses all contact points and thus corresponds to the gross or apparent contact area A_{gross}. It is roughly elliptical in shape at initial contact. However, during tangential loading of the fingertip, the contour deforms and often adopts a non-convex shape that depends on fingertip morphology and on the angle formed between the finger and the surface.

The algorithm consists of two major steps. First, a model is learned from images segmented manually, i.e. on which the actual contour was traced by a human operator. Then, after the model is trained for a given set of images, it is applied to segment new images on which it has not been trained. This allows the algorithm to be tuned for a specific set of images relatively easily (the training is performed on less than a hundred images), and then to be applied to a much larger number of images with good performance.

The algorithm is based on a linear classifier discriminating between two classes: (1) the foreground, defined as the interior of the contact, and (2) the background, defined as the exterior of the contact. More precisely, a given image is decomposed into square blocks of 16-by-16 pixels. On each block, several features are computed, that are described below. Then, these features are linearly combined to yield a given number, the weights of this linear combination being learned during the training phase. Therefore, a number is associated with each square in the image. If this number is larger than a given threshold, then the entire square is classified as belonging to the foreground. Otherwise, it is considered belonging to the background. Classifying each square portion of the image yields a binary image of the contact. This image being noisy due to inevitable classification error, some post-processing is needed to obtain a smooth contour.

The post-processing consists of several successive steps. First, the biggest connected component in the foreground is isolated and other, smaller components are discarded. Then, background holes isolated in the foreground are filled and thus changed into foreground. Next, an opening operation is performed on the image, which is a morphological operation consisting in eroding, then dilating the foreground to remove tiny patches of foreground. This opening operation has the effect of smoothing the contour of the contact. Finally, the contour of the foreground is extracted and further smoothed by convolving it with a Gaussian window.

Three features are computed on each square region of the image. They have been chosen because they gave reasonably different values for squares in the foreground and in the background, allowing these two classes to be separated by the linear classifier. The features are the following:

1. Variance of gray level within each square block;
2. Difference between the maximum and the minimum value of gray level within each square block;
3. A measure of the presence of fingerprints within each block, computed using Gabor filters. More precisely, this feature is computed as follows. First, the original image is filtered using 2D

Gabor filters whose spatial period matches the one of the fingerprints. Eight different filters are used, sharing the same spatial period but whose orientations vary regularly with steps of 180/8 degrees. Then, the standard deviation of the gray level is computed across the eight filtered images and is averaged within each square block, which gives the value of the feature within each block. This technique allows the periodic fingerprint patterns that are present in the foreground but absent in the background to be highlighted, effectively separating the foreground from the background.

Finally, because consecutive images in a given sequence do not vary much, the contour computed on a given image is used to limit the expansion of the contour on the next image of the sequence. Of course, this is not applicable to the first image of the sequence.

C.2. *Imagetools* toolbox

This toolbox contains tools dedicated to the analysis of fingertip contact mechanics from fingerprint images. It supports the image analysis workflow described in Chapters 4 and 5. It is based on the image analysis tools developed by Benoit Delhaye during his thesis (Delhaye, 2014) and initially served to analyze data presented in two studies examining the mechanical behavior of the finger pad under tangential loading (Delhaye et al., 2014, 2016). It has then been improved and was used to analyze data presented in this thesis. The formalism used throughout the code of this toolbox in described in the file `formalism.txt` accompanying the code.

C.3. *Libactivetouch* toolbox

This toolbox is used to analyze data acquired with the ActiveTouch manipulandum described in Chapter 4. It makes use of the *imagetools* functions to analyze image data but also contains code to process and visualize force and torque data acquired with the manipulandum as well as supporting function for experimental protocols.

Bibliography

Abraira, V.E., and Ginty, D.D. (2013). The sensory neurons of touch. Neuron *79*, 618–639.

Adams, M.J., Briscoe, B.J., and Johnson, S.A. (2007). Friction and lubrication of human skin. Tribol. Lett. *26*, 239–253.

Adams, M.J., Johnson, S.A., Lefèvre, P., Lévesque, V., Hayward, V., André, T., and Thonnard, J. (2013). Finger pad friction and its role in grip and touch. J. R. Soc. Interface *10*, 20120467.

Albe-Fessard, D., Andres, K.H., Bates, J.A.V., Besson, J.M., Brown, A.G., Burgess, P.R., Darian-Smith, I., v. Düring, M., Gordon, G., Hensel, H., et al. (1973). Handbook of Sensory Physiology Vol. II - Somatosensory System (Berlin, Heidelberg: Springer Berlin Heidelberg).

André, T., Lefèvre, P., and Thonnard, J.-L. (2009). A continuous measure of fingertip friction during precision grip. J. Neurosci. Methods *179*, 224–229.

André, T., Lefèvre, P., and Thonnard, J.-L. (2010). Fingertip moisture is optimally modulated during object manipulation. J. Neurophysiol. *103*, 402–408.

André, T., Lévesque, V., Hayward, V., Lefèvre, P., and Thonnard, J.-L. (2011). Effect of skin hydration on the dynamics of fingertip gripping contact. J. R. Soc. Interface *8*, 1574–1583.

Augurelle, A.-S., Smith, A.M., Lejeune, T., and Thonnard, J. (2003). Importance of cutaneous feedback in maintaining a secure grip during manipulation of hand-held objects. J. Neurophysiol. *89*, 665–671.

Barthel, E. (2008). Adhesive elastic contacts: JKR and more. J. Phys. D. Appl. Phys. *41*, 163001.

Bell, J., Bolanowski, S., and Holmes, M.H. (1994). The structure and function of pacinian corpuscles: A review. Prog. Neurobiol. *42*, 79–128.

Bengisu, M.T., and Akay, A. (1999). Stick–slip oscillations: Dynamics of friction and surface roughness. J. Acoust. Soc. Am. *105*, 194–205.

Bensmaia, S.J. (2008). Tactile intensity and population codes. Behav. Brain Res. *190*, 165–173.

Bensmaia, S.J., and Hollins, M. (2005). Pacinian representations of fine surface texture. Percept. Psychophys. *67*, 842–854.

Bensmaia, S.J., and Hollins, M. (2003). The vibrations of texture. Somatosens. Mot. Res. *20*, 33–43.

Bicchi, A., Scilingo, E.P., and De Rossi, D. (2000). Haptic discrimination of softness in teleoperation: the role of the contact area spread rate. IEEE Trans. Robot. Autom. *16*, 496–504.

Bielfeldt, S., Schoder, V., Ely, U., van der Pol, A., de Sterke, J., and Wilhelm, K.-P. (2009). Assessment of human stratum corneum thickness and its barrier properties by in-vivo confocal Raman spectroscopy. Int. J. Cosmet. Sci. *31*, 479–480.

Binder, M.D., Hirokawa, N., and Windhorst, U. (2009). Encyclopedia of Neuroscience (Berlin, Heidelberg: Springer Berlin Heidelberg).

Birznieks, I., Burstedt, M.K., Edin, B.B., and Johansson, R.S. (1998). Mechanisms for force adjustments to unpredictable frictional changes at individual digits during two-fingered manipulation. J. Neurophysiol. *80*, 1989–2002.

Birznieks, I., Jenmalm, P., Goodwin, A.W., and Johansson, R.S. (2001). Encoding of direction of fingertip forces by human tactile afferents. J. Neurosci. *21*, 8222–8237.

Birznieks, I., Macefield, V.G., Westling, G., and Johansson, R.S. (2009). Slowly adapting mechanoreceptors in the borders of the human fingernail encode fingertip forces. J. Neurosci. *29*, 9370–9379.

Birznieks, I., Wheat, H.E., Redmond, S.J., Salo, L.M., Lovell, N.H., and Goodwin, A.W. (2010). Encoding of tangential torque in responses of tactile afferent fibres innervating the fingerpad of the monkey. J. Physiol. *588*, 1057–1072.

Blake, D.T., Johnson, K.O., and Hsiao, S.S. (1997). Monkey cutaneous SAI and RA responses to raised and depressed scanned patterns: effects of width, height, orientation, and a raised surround. J. Neurophysiol. *78*, 2503–2517.

Bochereau, S., Dzidek, B.M., Adams, M.J., and Hayward, V. (2017). Characterizing and imaging gross and real finger contacts under dynamic loading. IEEE Trans. Haptics, *in press*.

Bouguet, J. (2001). Pyramidal implementation of the affine lucas kanade feature tracker description of the algorithm. Intel Corp. *1*, 1–9.

Boundy-Singer, Z.M., Saal, H.P., and Bensmaia, S.J. (2017). Speed invariance of tactile texture perception. J. Neurophysiol. *118*, 2371–2377.

Brisben, A.J., Hsiao, S.S., and Johnson, K.O. (1999). Detection of vibration transmitted through an object grasped in the hand. J. Neurophysiol. *81*, 1548–1558.

Cadoret, G., and Smith, A.M. (1996). Friction, Not Texture, Dictates Grip Forces Used During Object Manipulation. J. Neurophysiol. *75*, 1963–1969.

Cauna, N. (1956). Nerve supply and nerve endings in Meissner's corpuscles. Am. J. Anat. *99*, 315–350.

Chambers, M.R., Andres, K.H., von Duering, M., and Iggo, A. (1972). The structure and function of the slowly adapting type II mechanoreceptor in hairy skin. Q. J. Exp. Physiol. Cogn. Med. Sci. *57*, 417–445.

Comaish, S., and Bottoms, E. (1971). The skin and friction: deviations from Amonton's laws, and the effects of hydration and lubrication. Br. J. Dermatol. *84*, 37–43.

Crevecoeur, F., McIntyre, J., Thonnard, J.-L., and Lefèvre, P. (2010). Movement stability under uncertain internal models of dynamics. J. Neurophysiol. *104*, 1301–1313.

Crevecoeur, F., Giard, T., Thonnard, J.-L.J.-L., Lefèvre, P., and Lefevre, P. (2011). Adaptive control of grip force to compensate for static and dynamic torques during object manipulation. J. Neurophysiol. *106*, 2973–2981.

Crevecoeur, F., Thonnard, J.-L., Lefevre, P., and Scott, S.H. (2016). Long-Latency Feedback Coordinates Upper-Limb and Hand Muscles during Object Manipulation Tasks. eNeuro *3*.

Crevecoeur, F., Barrea, A., Libouton, X., Thonnard, J.-L., and Lefèvre, P. (2017). Multisensory components of rapid motor responses to fingertip loading. J. Neurophysiol. *118*, 331–343.

Dallmann, C.J., Ernst, M.O., and Moscatelli, A. (2015). The role of vibration in tactile speed perception. J. Neurophysiol. *114*, 3131–3139.

Daly, C.H. (1982). Biomechanical Properties of Dermis. J. Invest. Dermatol. *79*, 17–20.

Davare, M., Andres, M., Cosnard, G., Thonnard, J.-L., and Olivier, E. (2006). Dissociating the role of ventral and dorsal premotor cortex in precision grasping. J. Neurosci. *26*, 2260–2268.

Davare, M., Andres, M., Clerget, E., Thonnard, J.-L., and Olivier, E. (2007). Temporal dissociation between hand shaping and grip force scaling in the anterior intraparietal area. J. Neurosci. *27*, 3974–3980.

Davare, M., Kraskov, A., Rothwell, J.C., and Lemon, R.N. (2011). Interactions between areas of the cortical grasping network. Curr. Opin. Neurobiol. *21*, 565–570.

Delhaye, B.P. (2014). Skin mechanics involved in dynamic touch. Université catholique de Louvain.

Delhaye, B., Hayward, V., Lefèvre, P., and Thonnard, J.-L. (2012). Texture-induced vibrations in the forearm during tactile exploration. Front. Behav. Neurosci. *6*, 37.

Delhaye, B., Lefèvre, P., and Thonnard, J. (2014). Dynamics of fingertip contact during the onset of tangential slip. J. R. Soc. Interface *11*, 20140698.

Delhaye, B., Barrea, A., Edin, B.B., Lefèvre, P., and Thonnard, J.-L. (2016). Surface strain measurements of fingertip skin under shearing. J. R. Soc. Interface *13*, 20150874.

Delmas, P., Hao, J., and Rodat-Despoix, L. (2011). Molecular mechanisms of mechanotransduction in mammalian sensory neurons. Nat. Rev. Neurosci. *12*, 139–153.

Derjaguin, B., Muller, V., and Toporov, Y. (1975). Effect of contact deformations on the adhesion of particles. J. Colloid Interface Sci. *53*, 314–326.

Derler, S., Süess, J., Rao, A., and Rotaru, G.-M. (2013). Influence of variations in the pressure distribution on the friction of the finger pad. Tribol. Int. *63*, 14–20.

Diamond, J.S., Nashed, J.Y., Johansson, R.S., Wolpert, D.M., and Flanagan, J.R. (2015). Rapid Visuomotor Corrective Responses during Transport of Hand-Held Objects Incorporate Novel Object Dynamics. J. Neurosci. *35*, 10572–10580.

Dimitriou, M. (2014). Human Muscle Spindle Sensitivity Reflects the

Balance of Activity between Antagonistic Muscles. J. Neurosci. *34*, 13644–13655.

Dimitriou, M., and Edin, B.B. (2010). Human Muscle Spindles Act as Forward Sensory Models. Curr. Biol. *20*, 1763–1767.

Dostmohamed, H., and Hayward, V. (2005). Trajectory of contact region on the fingerpad gives the illusion of haptic shape. Exp. Brain Res. *164*, 387–394.

Dzidek, B.M., Bochereau, S., Johnson, S.A., Hayward, V., and Adams, M.J. (2016). Frictional dynamics of finger pads are governed by four length-scales and two time-scales. In 2016 IEEE Haptics Symposium (HAPTICS), (IEEE), pp. 161–166.

Dzidek, B.M., Bochereau, S., Johnson, S.A., Hayward, V., and Adams, M.J. (2017a). Why pens have rubbery grips. Proc. Natl. Acad. Sci. 201706233.

Dzidek, B.M., Adams, M.J., Zhang, Z., Johnson, S.A., Hayward, V., and Bochereau, S. (2014). Role of Occlusion in Non-Coulombic Slip of the Finger Pad. In EuroHaptics 2014, Part I. LNCS, Vol. 8618, M. Auvray, and C. Duriez, eds. (Berlin, Heidelberg: Springer Berlin Heidelberg), pp. 109–116.

Dzidek, B.M., Adams, M.J., Andrews, J.W., Zhang, Z., and Johnson, S.A. (2017b). Contact mechanics of the human finger pad under compressive loads. J. R. Soc. Interface *14*, 20160935.

Edin, B.B. (1992). Quantitative analysis of static strain sensitivity in human mechanoreceptors from hairy skin. J. Neurophysiol. *67*, 1105–1113.

Edin, B.B. (2004). Quantitative analyses of dynamic strain sensitivity in human skin mechanoreceptors. J. Neurophysiol. *92*, 3233–3243.

Edin, B.B., and Johansson, N. (1995). Skin strain patterns provide kinaesthetic information to the human central nervous system. J. Physiol. *487*, 243–251.

Edin, B.B., Bäckström, P.A., and Bäckström, L.O. (1988). Single unit retrieval in microneurography: a microprocessor-based device controlled by an operator. J. Neurosci. Methods *24*, 137–144.

Edin, B.B., Westling, G., and Johansson, R.S. (1992). Independent control of human finger-tip forces at individual digits during precision lifting. J. Physiol. *450*, 547–564.

Egawa, M., Hirao, T., and Takahashi, M. (2007). In vivo Estimation of Stratum Corneum Thickness from Water Concentration Profiles Obtained with Raman Spectroscopy. Acta Derm. Venereol. *87*, 4–8.

Ehrsson, H.H., Fagergren, A., Johansson, R.S., and Forssberg, H. (2003). Evidence for the involvement of the posterior parietal cortex in coordination of fingertip forces for grasp stability in manipulation. J. Neurophysiol. *90*, 2978–2986.

Ernst, M.O., and Banks, M.S. (2002). Humans integrate visual and haptic information in a statistically optimal fashion. Nature *415*, 429–433.

Fagiani, R., Massi, F., Chatelet, E., Costes, J.P., and Berthier, Y. (2012). Contact of a Finger on Rigid Surfaces and Textiles: Friction Coefficient and Induced Vibrations. Tribol. Lett. *48*, 145–158.

Farran, L., Ennos, A.R., and Eichhorn, S.J. (2008). The effect of humidity on the fracture properties of human fingernails. J. Exp. Biol. *211*, 3677–3681.

Farran, L., Ennos, A.R., Starkie, M., and Eichhorn, S.J. (2009). Tensile and shear properties of fingernails as a function of a changing humidity environment. J. Biomech. *42*, 1230–1235.

Finlay, A.Y. (1988). The physical properties and function of nails. In The Physical Nature of the Skin, (Dordrecht: Springer Netherlands), pp. 143–154.

Flanagan, J.R., and Wing, A.M. (1993). Modulation of grip force with load force during point-to-point arm movements. Exp. Brain Res. *95*, 131–143.

Flanagan, J.R., and Wing, A.M. (1995). The stability of precision grip forces during cyclic arm movements with a hand-held load. Exp. Brain Res. *105*, 455–464.

Flanagan, J.R., and Wing, A.M. (1997). The role of internal models in motion planning and control: evidence from grip force adjustments during movements of hand-held loads. J. Neurosci. *17*, 1519–1528.

Flanagan, J.R., Bowman, M.C., and Johansson, R.S. (2006). Control strategies in object manipulation tasks. Curr. Opin. Neurobiol. *16*, 650–659.

Flesher, S.N., Collinger, J.L., Foldes, S.T., Weiss, J.M., Downey, J.E., Tyler-Kabara, E.C., Bensmaia, S.J., Schwartz, A.B., Boninger, M.L., and Gaunt, R.A. (2016). Intracortical microstimulation of human somatosensory cortex. Sci. Transl. Med. *8*, 361ra141-361ra141.

Fluhr, J.W., Gloor, M., Lazzerini, S., Kleesz, P., Grieshaber, R., and Berardesca, E. (1999). Comparative study of five instruments measuring stratum corneum hydration (Corneometer CM 820 and CM 825, Skicon 200, Nova DPM 9003, DermaLab). Part II. In vivo. Ski. Res. Technol. *5*, 171–178.

Formby, C., Morgan, L.N., Forrest, T.G., and Raney, J.J. (1992). The role of frequency selectivity in measures of auditory and vibrotactile temporal resolution. J. Acoust. Soc. Am. *91*, 293–305.

Fradet, C., Manfredi, L.R., Bensmaia, S., and Hayward, V. (2017). Fingertip skin as a linear medium for wave propagation. In 2017 IEEE World Haptics Conference (WHC), (IEEE), pp. 507–510.

Fratzl, P., Misof, K., Zizak, I., Rapp, G., Amenitsch, H., and Bernstorff, S. (1998). Fibrillar Structure and Mechanical Properties of Collagen. J. Struct. Biol. *122*, 119–122.

Freeman, A., and Johnson, K. (1982). Cutaneous mechanoreceptors in macaque monkey: temporal discharge patterns evoked by vibration, and a receptor model. J. Physiol. 21–41.

de Freitas, P.B., Uygur, M., and Jaric, S. (2009). Grip force adaptation in manipulation activities performed under different coating and grasping conditions. Neurosci. Lett. *457*, 16–20.

Fruhstorfer, H., Abel, U., Garthe, C.D., and Knüttel, A. (2000). Thickness of the stratum corneum of the volar fingertips. Clin. Anat. *13*, 429–433.

Gao, J., Luedtke, W.D., Gourdon, D., Ruths, M., Israelachvili, J.N., and Landman, U. (2004). Frictional Forces and Amontons' Law: From the Molecular to the Macroscopic Scale. J. Phys. Chem. B *108*, 3410–3425.

Gardner, E.P. (2010). Touch. In Encyclopedia of Life Sciences, (Chichester, UK: John Wiley & Sons, Ltd), pp. 1–12.

Garnett, R., and Stephens, J.A. (1980). The reflex responses of single motor units in human first dorsal interosseous muscle following cutaneous afferent stimulation. J. Physiol. *303*, 351–364.

Gartner, L.P., and Hiatt, J.L. (2015). Cell Biology & Histology (Wolters Kluwer Health).

Ge, W., and Khalsa, P.S. (2002). Encoding of Compressive Stress During Indentation by Slowly Adapting Type I Mechanoreceptors in Rat Hairy Skin. J. Neurophysiol. *87*, 1686–1693.

Giard, T., Crevecoeur, F., McIntyre, J., Thonnard, J.-L., and Lefèvre, P. (2015). Inertial torque during reaching directly impacts grip-force adaptation to weightless objects. Exp. Brain Res. *233*, 3323–3332.

Goodman, J.M., and Bensmaia, S.J. (2017). A Variation Code Accounts for the Perceived Roughness of Coarsely Textured Surfaces. Sci. Rep. *7*, 46699.

Goodwin, A.W., and Wheat, H.E. (2004). Sensory signals in neural populations underlying tactile perception and manipulation. Annu. Rev. Neurosci. *27*, 53–77.

Goodwin, A.W., Browning, A.S., and Wheat, H.E. (1995). Representation of curved surfaces in responses of mechanoreceptive afferent fibers innervating the monkey's fingerpad. J. Neurosci. *15*, 798–810.

Graczyk, E.L., Schiefer, M.A., Saal, H.P., Delhaye, B.P., Bensmaia, S.J., and Tyler, D.J. (2016). The neural basis of perceived intensity in natural and artificial touch. Sci. Transl. Med. *8*, 362ra142-362ra142.

Grafton, S.T. (2010). The cognitive neuroscience of prehension: recent developments. Exp. Brain Res. *204*, 475–491.

Gueorguiev, D., Bochereau, S., Mouraux, A., Hayward, V., and Thonnard, J.-L. (2016). Touch uses frictional cues to discriminate flat materials. Sci. Rep. *6*, 25553.

Guest, S., Mehrabyan, A., Essick, G., Phillips, N., Hopkinson, A., and McGlone, F. (2012). Physics and tactile perception of fluid-covered surfaces. J. Texture Stud. *43*, 77–93.

Hadjiosif, A.M., and Smith, M.A. (2015). Flexible Control of Safety Margins for Action Based on Environmental Variability. J. Neurosci. *35*, 9106–9121.

Haiat, G., Phan Huy, M.C., and Barthel, E. (2003). The adhesive contact of viscoelastic spheres. J. Mech. Phys. Solids *51*, 69–99.

Han, H., Shimada, A., and Kawamura, S. (1996). Analysis of friction on human fingers and design of artificial fingers. In Proceedings of IEEE International Conference on Robotics and Automation, (IEEE), pp. 3061–3066.

Hauck, R.M., Camp, L., Ehrlich, H.P., Saggers, G.C., Banducci, D.R., and Graham, W.P. (2004). Pulp Nonfiction: Microscopic Anatomy of the Digital Pulp Space. Plast. Reconstr. Surg. *113*, 536–539.

Hayward, V. (2011). Is there a "plenhaptic" function? Philos. Trans. R. Soc. Lond. B. Biol. Sci. *366*, 3115–3122.

Heinrich, U., Koop, U., Leneveu-Duchemin, M.-C., Osterrieder, K., Bielfeldt, S., Chkarnat, C., Degwert, J., Hantschel, D., Jaspers, S., Nissen, H.-P., et al. (2003). Multicentre comparison of skin hydration in terms of physical-, physiological- and product-dependent parameters by the capacitive method (Corneometer CM 825). Int. J. Cosmet. Sci. *25*, 45–53.

Ho, V.A., and Hirai, S. (2014). Mechanics of Localized Slippage in Tactile Sensing (Springer).

Ho, V.A., and Hirai, S. (2015). A novel model for assessing sliding mechanics and tactile sensation of human-like fingertips during slip action. Rob. Auton. Syst. *63*, 253–267.

Hollins, M., and Risner, S.R. (2000). Evidence for the duplex theory of tactile texture perception. Percept. Psychophys. *62*, 695–705.

Hollins, M., Bensmaia, S.J., and Washburn, S. (2001). Vibrotactile adaptation impairs discrimination of fine, but not coarse, textures. Somatosens. Mot. Res. *18*, 253–262.

Hsiao, S. (2008). Central mechanisms of tactile shape perception. Curr. Opin. Neurobiol. *18*, 418–424.

Hui, C.-Y., Baney, J.M., and Kramer, E.J. (1998). Contact Mechanics and Adhesion of Viscoelastic Spheres. Langmuir *14*, 6570–6578.

Iggo, A., and Muir, A.R. (1969). The structure and function of a slowly adapting touch corpuscle in hairy skin. J. Physiol. *200*, 763–796.

Iggo, A, and Andres, K.H. (1982). Morphology of cutaneous receptors. Annu. Rev. Neurosci. *5*, 1–31.

Ikeda, R., Cha, M., Ling, J., Jia, Z., Coyle, D., and Gu, J.G. (2014). Merkel Cells Transduce and Encode Tactile Stimuli to Drive Aβ-Afferent Impulses. Cell *157*, 664–675.

Jenmalm, P., Birznieks, I., Goodwin, A.W., and Johansson, R.S. (2003). Influence of object shape on responses of human tactile afferents under conditions characteristic of manipulation. Eur. J. Neurosci. *18*, 164–176.

Jindrich, D.L., Zhou, Y., Becker, T., and Dennerlein, J.T. (2003). Non-linear viscoelastic models predict fingertip pulp force-displacement characteristics during voluntary tapping. J. Biomech. *36*, 497–503.

Johansson, R.S., and Vallbo, Å.B. (1983). Tactile sensory coding in the glabrous skin of the human hand. Trends Neurosci. *100*.

Johansson, R.S., and Westling, G. (1984). Roles of glabrous skin receptors and sensorimotor memory in automatic control of precision grip when lifting rougher or more slippery objects. Exp. Brain Res. 550–564.

Johansson, R.S., and Westling, G. (1987). Signals in tactile afferents from the fingers eliciting adaptive motor responses during precision grip. Exp.

Brain Res. 141–154.

Johansson, R.S., and Birznieks, I. (2004). First spikes in ensembles of human tactile afferents code complex spatial fingertip events. Nat. Neurosci. *7*, 170–177.

Johansson, R.S., and Cole, K.J. (1992). Sensory-motor coordination during grasping and manipulative actions. Curr. Opin. Neurobiol. *2*, 815–823.

Johansson, R.S., and Flanagan, J.R. (2009). Coding and use of tactile signals from the fingertips in object manipulation tasks. Nat. Rev. Neurosci. *10*, 345–359.

Johansson, R.S., and Vallbo, Å.B. (1979). Detection of tactile stimuli. Thresholds of afferent units related to psychophysical thresholds in the human hand. J. Physiol. *297*, 405–422.

Johansson, R.S., Westling, G., Bäckström, A., and Flanagan, J.R. (2001). Eye-hand coordination in object manipulation. J Neurosci *21*, 6917–6932.

Johnson, K.L. (1985). Contact mechanics (Cambridge University Press).

Johnson, K.O. (2002). Neural Basis of Haptic Perception. In Stevens' Handbook of Experimental Psychology, (Hoboken, NJ, USA: John Wiley & Sons, Inc.), pp. 537–580.

Johnson, K.O. (2001). The roles and functions of cutaneous mechanoreceptors. Curr. Opin. Neurobiol. *11*, 455–461.

Johnson, K.L., Kendall, K., and Roberts, A.D. (1971). Surface Energy and the Contact of Elastic Solids. Proc. R. Soc. A Math. Phys. Eng. Sci. *324*, 301–313.

Jones, L.A., and Lederman, S.J. (2006). Human hand function (Oxford University Press).

Jones, L.A., and Tan, H.Z. (2013). Application of psychophysical techniques to haptic research. IEEE Trans. Haptics *6*, 268–284.

Kandel, E.R., Schwartz, J., and Jessell, T. (2000). Principles of Neural Science (McGraw-Hill Companies, Inc.).

Khamis, H., Redmond, S.J., Macefield, V.G., and Birznieks, I. (2014a). Classification of Texture and Frictional Condition at Initial Contact by Tactile Afferent Responses. In EuroHaptics 2014, Part I. LNCS, Vol. 8618, M. Auvray, and C. Duriez, eds. (Berlin, Heidelberg: Springer Berlin Heidelberg), pp. 460–468.

Khamis, H., Birznieks, I., and Redmond, S.J. (2015). Decoding tactile afferent activity to obtain an estimate of instantaneous force and torque applied to the fingerpad. J. Neurophysiol. *114*, 474–484.

Khamis, H., Redmond, S.J., Macefield, V.G., and Birznieks, I. (2014b). Tactile afferents encode grip safety before slip for different frictions. In 2014 36th Annual International Conference of the IEEE Engineering in Medicine and Biology Society, (IEEE), pp. 4123–4126.

Klöcker, A., Wiertlewski, M., Théate, V., Hayward, V., and Thonnard, J.-L. (2013). Physical Factors Influencing Pleasant Touch during Tactile Exploration. PLoS One *8*, e79085.

Körding, K.P., and Wolpert, D.M. (2004). Bayesian integration in sensorimotor learning. Nature *427*, 244–247.

van Kuilenburg, J., Masen, M. a., and van der Heide, E. (2013). A review of fingerpad contact mechanics and friction and how this affects tactile perception. Proc. Inst. Mech. Eng. Part J J. Eng. Tribol.

LaMotte, R.H., and Mountcastle, V.B. (1975). Capacities of humans and monkeys to discriminate vibratory stimuli of different frequency and amplitude: a correlation between neural events and psychological measurements. J. Neurophysiol. *38*, 539–559.

LaMotte, R.H., and Whitehouse, J. (1986). Tactile detection of a dot on a smooth surface: peripheral neural events. J. Neurophysiol. *56*, 1109–1128.

Lemon, R.N., Johansson, R.S., and Westling, G. (1995). Corticospinal control during reach, grasp, and precision lift in man. J. Neurosci. *15*, 6145–6156.

Lesniak, D.R., Marshall, K.L., Wellnitz, S.A., Jenkins, B.A., Baba, Y., Rasband, M.N., Gerling, G.J., and Lumpkin, E.A. (2014). Computation identifies structural features that govern neuronal firing properties in slowly adapting touch receptors. Elife *3*, e01488.

Lévêque, J.L., and Rasseneur, L. (1988). Mechanical properties of stratum corneum: influence of water and lipids. In The Physical Nature of the Skin, (Dordrecht: Springer Netherlands), pp. 155–161.

Levesque, V., and Hayward, V. (2003). Experimental evidence of lateral skin strain during tactile exploration. Proc. Eurohaptics.

Libouton, X., Barbier, O., Plaghki, L., and Thonnard, J.-L. (2010). Tactile roughness discrimination threshold is unrelated to tactile spatial acuity. Behav. Brain Res. *208*, 473–478.

Liu, L.L. (2012). Effects of the Varying Normal Force on the Stick Slip Motion of Systems with Friction. Adv. Mater. Res. *479–481*, 1078–1083.

Liu, X., Lu, Z., Lewis, R., Carré, M.J., and Matcher, S.J. (2013). Feasibility of using optical coherence tomography to study the influence of skin structure on finger friction. Tribol. Int. *63*, 34–44.

Liu, X., Gad, D., Lu, Z., Lewis, R., Carré, M., and Matcher, S. (2015). The contributions of skin structural properties to the friction of human finger-pads. Proc. Inst. Mech. Eng. Part J J. Eng. Tribol. *229*, 294–311.

Liu, X., Carré, M.J., Zhang, Q., Lu, Z., Matcher, S.J., and Lewis, R. (2017). Measuring contact area in a sliding human finger-pad contact. Ski. Res. Technol. 1–14.

Loewenstein, W.R., and Skalak, R. (1966). Mechanical transmission in a Pacinian corpuscle. An analysis and a theory. J. Physiol. *182*, 346–378.

Lucas, B., and Kanade, T. (1981). An iterative image registration technique with an application to stereo vision. In IJCAI'81 Proceedings of the 7th International Joint Conference on Artificial Intelligence, pp. 674–679.

Lumpkin, E.A., and Caterina, M.J. (2007). Mechanisms of sensory transduction in the skin. Nature *445*, 858–865.

Macefield, V.G., and Johansson, R.S. (1996). Control of grip force during restraint of an object held between finger and thumb: responses of muscle and joint afferents from the digits. Exp. Brain Res. *108*, 172–184.

Macefield, V.G., and Johansson, R.S. (2003). Loads applied tangential to a fingertip during an object restraint task can trigger short-latency as well as long-latency EMG responses in hand muscles. Exp. Brain Res. *152*, 143–149.

Macefield, V.G., Häger-Ross, C., and Johansson, R.S. (1996). Control of grip force during restraint of an object held between finger and thumb: responses of cutaneous afferents from the digits. Exp. Brain Res. *108*, 155–171.

Mahns, D.A., Perkins, N.M., Sahai, V., Robinson, L., and Rowe, M.J. (2006). Vibrotactile frequency discrimination in human hairy skin. J. Neurophysiol. *95*, 1442–1450.

Maksimovic, S., Nakatani, M., Baba, Y., Nelson, A.M., Marshall, K.L., Wellnitz, S.A., Firozi, P., Woo, S.-H., Ranade, S., Patapoutian, A., et al. (2014). Epidermal Merkel cells are mechanosensory cells that tune mammalian touch receptors. Nature *509*, 617–621.

Manfredi, L.R., Baker, A.T., Elias, D.O., Dammann, J.F., Zielinski, M.C., Polashock, V.S., and Bensmaia, S.J. (2012). The effect of surface wave propagation on neural responses to vibration in primate glabrous skin. PLoS One *7*, e31203.

Manfredi, L.R., Saal, H.P., Brown, K.J., Zielinski, M.C., Dammann, J.F., Polashock, V.S., and Bensmaia, S.J. (2014). Natural scenes in tactile texture. J. Neurophysiol. *111*, 1792–1802.

Manning, C.D., and Bawa, P. (2011). Heteronymous reflex connections in human upper limb muscles in response to stretch of forearm muscles. J. Neurophysiol. *106*, 1489–1499.

Maricich, S.M., Wellnitz, S.A., Nelson, A.M., Lesniak, D.R., Gerling, G.J., Lumpkin, E. a, and Zoghbi, H.Y. (2009). Merkel cells are essential for light-touch responses. Science *324*, 1580–1582.

Maricich, S.M., Morrison, K.M., Mathes, E.L., and Brewer, B.M. (2012). Rodents rely on Merkel cells for texture discrimination tasks. J. Neurosci. *32*, 3296–3300.

Marsden, C.D., Merton, P.A., and Morton, H.B. (1976). Servo action in the human thumb. J. Physiol. *257*, 1–44.

Martini, F.H., Timmons, M.J., and Tallitsch, R.B. (2012). Human anatomy (Pearson Benjamin Cummings).

Miall, R.C., Weir, D.J., Wolpert, D.M., and Stein, J.F. (1993). Is the Cerebellum a Smith Predictor? J. Mot. Behav. *25*, 203–216.

Monzée, J., Lamarre, Y., and Smith, A.M. (2003). The effects of digital anesthesia on force control using a precision grip. J. Neurophysiol. *89*, 672–683.

Moscatelli, A., Naceri, A., and Ernst, M.O. (2014). Path integration in tactile perception of shapes. Behav. Brain Res. *274*, 355–364.

Moscatelli, A., Bianchi, M., Serio, A., Terekhov, A., Hayward, V., Ernst, M.O., and Bicchi, A. (2016). The Change in Fingertip Contact Area as a Novel Proprioceptive Cue. Curr. Biol. *26*, 1159–1163.

Mountcastle, V.B., LaMotte, R.H., and Carli, G. (1972). Detection thresholds for stimuli in humans and monkeys: comparison with threshold events in mechanoreceptive afferent nerve fibers innervating the monkey hand. J. Neurophysiol. *35*, 122–136.

Muller, V.M., Derjaguin, B.V., and Toporov, Y.P. (1983). On two methods of calculation of the force of sticking of an elastic sphere to a rigid plane. Colloids and Surfaces *7*, 251–259.

Muniak, M.A., Ray, S., Hsiao, S.S., Dammann, J.F., and Bensmaia, S.J. (2007). The neural coding of stimulus intensity: linking the population response of mechanoreceptive afferents with psychophysical behavior. J. Neurosci. *27*, 11687–11699.

Netter, F.H. (2014). Atlas of Human Anatomy (Saunders).

Nowak, D.A., Hermsdörfer, J., Glasauer, S., Philipp, J., Meyer, L., and Mai, N. (2001). The effects of digital anaesthesia on predictive grip force adjustments during vertical movements of a grasped object. Eur. J. Neurosci. *14*, 756–762.

Nowak, D.A., Glasauer, S., Meyer, L., Mai, N., and Hermsdörfer, J. (2002). The role of cutaneous feedback for anticipatory grip force adjustments during object movements and externally imposed variation of the direction of gravity. Somatosens. Mot. Res. *19*, 49–60.

Olausson, H., Wessberg, J., and Kakuda, N. (2000). Tactile directional sensibility: peripheral neural mechanisms in man. Brain Res. *866*, 178–187.

Pacchierotti, C., Prattichizzo, D., and Kuchenbecker, K.J. (2016). Cutaneous Feedback of Fingertip Deformation and Vibration for Palpation in Robotic Surgery. IEEE Trans. Biomed. Eng. *63*, 278–287.

Pailler-Mattei, C., Pavan, S., Vargiolu, R., Pirot, F., Falson, F., and Zahouani, H. (2007). Contribution of stratum corneum in determining bio-tribological properties of the human skin. Wear *263*, 1038–1043.

Paré, M., Elde, R., Mazurkiewicz, J.E., Smith, A.M., and Rice, F.L. (2001). The Meissner corpuscle revised: a multiafferented mechanoreceptor with nociceptor immunochemical properties. J Neurosci *21*, 7236–7246.

Paré, M., Smith, A.M., and Rice, F.L. (2002a). Distribution and terminal arborizations of cutaneous mechanoreceptors in the glabrous finger pads of the monkey. J. Comp. Neurol. *359*, 347–359.

Paré, M., Carnahan, H., and Smith, A.M. (2002b). Magnitude estimation of tangential force applied to the fingerpad. Exp. Brain Res. *142*, 342–348.

Paré, M., Behets, C., and Cornu, O. (2003). Paucity of presumptive ruffini corpuscles in the index finger pad of humans. J. Comp. Neurol. *456*, 260–266.

Pashley, M.D. (1984). Further consideration of the DMT model for elastic contact. Colloids and Surfaces *12*, 69–77.

Pasumarty, S.M., Johnson, S.A., Watson, S.A., and Adams, M.J. (2011). Friction of the Human Finger Pad: Influence of Moisture, Occlusion and Velocity. Tribol. Lett. *44*, 117–137.

Pataky, T.C., Latash, M.L., and Zatsiorsky, V.M. (2005). Viscoelastic response of the finger pad to incremental tangential displacements. J. Biomech. *38*, 1441–1449.

Pawluk, D.T., and Howe, R.D. (1999a). Dynamic lumped element response of the human fingerpad. J. Biomech. Eng. *121*, 178–183.

Pawluk, D.T., and Howe, R.D. (1999b). Dynamic contact of the human fingerpad against a flat surface. J. Biomech. Eng. *121*, 605–611.

Peckham, M., Knibbs, A., and Paxton, S. (2017). The Histology Guide (online).

Pei, Y.-C., Denchev, P. V, Hsiao, S.S., Craig, J.C., and Bensmaia, S.J. (2009). Convergence of submodality-specific input onto neurons in primary somatosensory cortex. J. Neurophysiol. *102*, 1843–1853.

Persson, B.N.J. (2007). Relation between Interfacial Separation and Load: A General Theory of Contact Mechanics. Phys. Rev. Lett. *99*, 125502.

Persson, B.N.J., Kovalev, A., and Gorb, S.N. (2013). Contact Mechanics and Friction on Dry and Wet Human Skin. Tribol. Lett. *50*, 17–30.

Phillips, J.R., and Johnson, K.O. (1981). Tactile spatial resolution. II. Neural representation of Bars, edges, and gratings in monkey primary afferents. J. Neurophysiol. *46*, 1192–1203.

Phillips, J.R., Johansson, R.S., and Johnson, K.O. (1990). Representation of braille characters in human nerve fibres. Exp. Brain Res. *81*, 589–592.

Pires, T., Azambuja, A.P., Horimoto, A., Veroneze, M., Alvim, R., Krieger, J.E., and Pereira, A. (2016). A population-based study of the stratum corneum moisture. Clin. Cosmet. Investig. Dermatol. *9*, 79–87.

Prevost, A., Scheibert, J., and Debrégeas, G. (2009). Effect of fingerprints orientation on skin vibrations during tactile exploration of textured surfaces. 3.

Pruszynski, J.A., and Johansson, R.S. (2014). Edge-orientation processing in first-order tactile neurons. Nat. Neurosci. *17*, 1404–1409.

Pruszynski, J.A., Johansson, R.S., and Flanagan, J.R. (2016). A Rapid Tactile-Motor Reflex Automatically Guides Reaching toward Handheld

Objects. Curr. Biol. *26*, 788–792.

Pruszynski, J.A., Flanagan, J.R., and Johansson, R.S. (2017). Fast and accurate edge orientation processing during object manipulation. bioRxiv.

Purves, D., Augustine, G.J., Fitzpatrick, D., Hall, W.C., LaMantia, A.-S., and White, L. (2012). Neuroscience (Sinauer Associates, Inc.).

Quindlen, J.C., Stolarski, H.K., Johnson, M.D., and Barocas, V.H. (2016). A multiphysics model of the Pacinian corpuscle. Integr. Biol. *8*, 1111–1125.

Raspopovic, S., Capogrosso, M., Petrini, F.M., Bonizzato, M., Rigosa, J., Di Pino, G., Carpaneto, J., Controzzi, M., Boretius, T., Fernandez, E., et al. (2014). Restoring Natural Sensory Feedback in Real-Time Bidirectional Hand Prostheses. Sci. Transl. Med. *6*, 222ra19-222ra19.

Rothwell, J.C., Traub, M.M., and Marsden, C.D. (1982). Automatic and "voluntary" responses compensating for disturbances of human thumb movements. Brain Res. *248*, 33–41.

Saal, H.P., and Bensmaia, S.J. (2014). Touch is a team effort: interplay of submodalities in cutaneous sensibility. Trends Neurosci. *2*, 1–9.

Salada, M., Vishton, P., Colgate, J.E., and Frankel, E. (2004). Two experiments on the perception of slip at the fingertip. In 12th International Symposium on Haptic Interfaces for Virtual Environment and Teleoperator Systems, 2004. HAPTICS '04. Proceedings., (IEEE), pp. 146–153.

Savescu, A. V, Latash, M.L., and Zatsiorsky, V.M. (2008). A technique to determine friction at the fingertips. J. Appl. Biomech. *24*, 43–50.

Schabrun, S.M., Ridding, M.C., and Miles, T.S. (2008). Role of the primary motor and sensory cortex in precision grasping: a transcranial magnetic stimulation study. Eur. J. Neurosci. *27*, 750–756.

Schallamach, A. (1952). The Load Dependence of Rubber Friction. Proc. Phys. Soc. Sect. B *65*, 657–661.

Scheibert, J., Leurent, S., Prevost, A., and Debregeas, G. (2009). The Role of Fingerprints in the Coding of Tactile Information Probed with a Biomimetic Sensor. Science (80-.). *323*, 1503–1506.

Scott, S.H. (2004). Optimal feedback control and the neural basis of volitional motor control. Nat. Rev. Neurosci. *5*, 532–546.

Seah, B.Z.Q., Wu, C.C.H., Sebastin, S.J., and Lahiri, A. (2013). Tactile Sensibility on the Fingernail. J. Hand Surg. Am. *38*, 2159–2163.

Seo, N.J., and Armstrong, T.J. (2009). Friction coefficients in a longitudinal direction between the finger pad and selected materials for different normal forces and curvatures. Ergonomics *52*, 609–616.

Serina, E.R., Mote, C.D., and Rempel, D. (1997). Force response of the fingertip pulp to repeated compression—Effects of loading rate, loading angle and anthropometry. J. Biomech. *30*, 1035–1040.

Shao, Y., Hayward, V., and Visell, Y. (2016). Spatial patterns of cutaneous vibration during whole-hand haptic interactions. Proc. Natl. Acad. Sci. *113*, 4188–4193.

Shi, J., and Tomasi, C. (1994). Good features to track. In Proceedings of IEEE Conference on Computer Vision and Pattern Recognition CVPR-94, (IEEE Comput. Soc. Press), pp. 593–600.

Shultz, C.D., Peshkin, M.A., and Colgate, J.E. (2017). The application of tactile, audible, and ultrasonic forces to human fingertips using broadband electroadhesion. In 2017 IEEE World Haptics Conference (WHC), (IEEE), pp. 119–124.

Singh, T., and Ambike, S. (2017). A soft-contact model for computing safety margins in human prehension. Hum. Mov. Sci., *in press*.

Skedung, L., Arvidsson, M., Chung, J.Y., Stafford, C.M., Berglund, B., and Rutland, M.W. (2013). Feeling Small: Exploring the Tactile Perception Limits. Sci. Rep. *3*, 2617.

Smith, A.M., and Scott, S.H. (1996). Subjective scaling of smooth surface friction. J. Neurophysiol. *75*, 1957–1962.

Smith, A.M., Chapman, C.E., Deslandes, M., Langlais, J.-S., and Thibodeau, M.-P. (2002). Role of friction and tangential force variation in the subjective scaling of tactile roughness. Exp. Brain Res. *144*, 211–223.

Srinivasan, M.A., Whitehouse, J.M., and LaMotte, R.H. (1990). Tactile detection of slip: surface microgeometry and peripheral neural codes. J. Neurophysiol. *63*, 1323–1332.

Sripati, A.P., Bensmaia, S.J., and Johnson, K.O. (2006). A continuum mechanical model of mechanoreceptive afferent responses to indented spatial patterns. J. Neurophysiol. *95*, 3852–3864.

Tada, M., and Kanade, T. (2004). An imaging system of incipient slip for modelling how human perceives slip of a fingertip. Conf. Proc. 26th Annu. Int. Conf. IEEE Eng. Med. Biol. Soc. IEEE Eng. Med. Biol. Soc. Conf. *3*, 2045–2048.

Tada, M., Imai, M., and Ogasawara, T. (2000). Development of simultaneous measurement system of incipient slip and grip/load force. In Proceedings 9th IEEE International Workshop on Robot and Human Interactive Communication. IEEE RO-MAN 2000 (Cat. No.00TH8499), (IEEE), pp. 57–62.

Tada, M., Shibata, T., and Ogasawara, T. (2002). Investigation of the touch processing model in human grasping based on the stick ratio within a fingertip contact interface. In IEEE International Conference on Systems, Man and Cybernetics, (IEEE), p. 6.

Tada, M., Mochimaru, M., and Kanade, T. (2006). How does a fingertip slip? Visualizing partial slippage for modeling of contact mechanics. In EuroHaptics 2006, pp. 415–420.

Talbot, W.H., Darian-Smith, I., Kornhuber, H.H., and Mountcastle, V.B. (1968). The sense of flutter-vibration: comparison of the human capacity with response patterns of mechanoreceptive afferents from the monkey hand. J. Neurophysiol. *31*, 301–334.

Tan, D.W., Schiefer, M.A., Keith, M.W., Anderson, J.R., Tyler, J., and Tyler, D.J. (2014). A neural interface provides long-term stable natural touch perception. Sci. Transl. Med. *6*.

Taoka, M., Toda, T., Iriki, A., Tanaka, M., and Iwamura, Y. (2000). Bilateral receptive field neurons in the hindlimb region of the postcentral somatosensory cortex in awake macaque monkeys. Exp. Brain Res. *134*, 139–146.

Tomlinson, S.E., Lewis, R., and Carré, M.J. (2007). Review of the frictional properties of finger—object contact when gripping. Proc. Inst. Mech. Eng. Part J J. Eng. Tribol. *221*, 841–850.

Tomlinson, S.E., Lewis, R., Liu, X., Texier, C., and Carré, M.J. (2011). Understanding the Friction Mechanisms Between the Human Finger and Flat Contacting Surfaces in Moist Conditions. Tribol. Lett. *41*, 283–294.

Uitto, J. (2008). The role of elastin and collagen in cutaneous aging: intrinsic aging versus photoexposure. J. Drugs Dermatol. *7*, s12-6.

Vallbo, Å.B., and Hagbarth, K.-E. (1968). Activity from skin mechanoreceptors recorded percutaneously in awake human subjects. Exp. Neurol. *21*, 270–289.

Vallbo, Å.B., and Johansson, R.S. (1984). Properties of cutaneous mechanoreceptors in the human hand related to touch sensation. Hum.

Neurobiol. *3*, 3–14.

Vallbo, Å.B., Olsson, K.Å., Westberg, K.-G., and Clark, F.J. (1984). Microstimulation of Single Tactile Afferents From the Human Hand. Brain *107*, 727–749.

Vardar, Y., Guclu, B., and Basdogan, C. (2017). Effect of Waveform on Tactile Perception by Electrovibration Displayed on Touch Screens. IEEE Trans. Haptics *1412*, 1–1.

Vezzoli, E., Ben Messaoud, W., Amberg, M., Giraud, F., Lemaire-Semail, B., and Bueno, M.A. (2015). Physical and perceptual independence of ultrasonic vibration and electrovibration for friction modulation. IEEE Trans. Haptics *8*, 235–239.

Wang, Q., and Hayward, V. (2007). In vivo biomechanics of the fingerpad skin under local tangential traction. J. Biomech. *40*, 851–860.

Warman, P.H., and Ennos, A.R. (2009). Fingerprints are unlikely to increase the friction of primate fingerpads. J. Exp. Biol. *212*, 2016–2022.

Weber, A.I., Saal, H.P., Lieber, J.D., Cheng, J.-W., Manfredi, L.R., Dammann, J.F., and Bensmaia, S.J. (2013). Spatial and temporal codes mediate the tactile perception of natural textures. Proc. Natl. Acad. Sci. U. S. A. *110*, 17107–17112.

Webster, R.J., Murphy, T.E., Verner, L.N., and Okamura, A.M. (2005). A novel two-dimensional tactile slip display: design, kinematics and perceptual experiments. ACM Trans. Appl. Percept. *2*, 150–165.

Wellnitz, S.A., Lesniak, D.R., Gerling, G.J., and Lumpkin, E.A. (2010). The Regularity of Sustained Firing Reveals Two Populations of Slowly Adapting Touch Receptors in Mouse Hairy Skin. J. Neurophysiol. *103*, 3378–3388.

Wenger, M.P.E., Bozec, L., Horton, M.A., and Mesquida, P. (2007). Mechanical Properties of Collagen Fibrils. Biophys. J. *93*, 1255–1263.

Westling, G., and Johansson, R.S. (1984). Factors influencing the force control during precision grip. Exp. Brain Res. *53*, 277–284.

Westling, G., and Johansson, R.S. (1987). Responses in glabrous skin mechanoreceptors during precision grip in humans. Exp. Brain Res. *66*, 128–140.

White, O., Thonnard, J.-L., Wing, A.M., Bracewell, R.M., Diedrichsen, J., and Lefèvre, P. (2011). Grip force regulates hand impedance to optimize object stability in high impact loads. Neuroscience *189*, 269–276.

Wiertlewski, M., and Hayward, V. (2012). Mechanical behavior of the fingertip in the range of frequencies and displacements relevant to touch. J. Biomech. *45*, 1869–1874.

Wiertlewski, M., Endo, S., Wing, A.M., and Hayward, V. (2013). Slip-induced vibration influences the grip reflex: a pilot study. 2013 World Haptics Conf. 627–632.

Wiertlewski, M., Fenton Friesen, R., and Colgate, J.E. (2016). Partial squeeze film levitation modulates fingertip friction. Proc. Natl. Acad. Sci. *113*, 9210–9215.

Wilke, K., Martin, A., Terstegen, L., and Biel, S.S. (2007). A short history of sweat gland biology. Int. J. Cosmet. Sci. *29*, 169–179.

Williams, A.L., Gerling, G.J., Wellnitz, S.A., Bourdon, S.M., and Lumpkin, E.A. (2010). Skin relaxation predicts neural firing rate adaptation in SAI touch receptors. In 2010 Annual International Conference of the IEEE Engineering in Medicine and Biology, (IEEE), pp. 6678–6681.

Witney, A.G., Wing, A., Thonnard, J.-L., and Smith, A.M. (2004). The cutaneous contribution to adaptive precision grip. Trends Neurosci. *27*, 637–643.

Wolfram, L. (1983). Friction of skin. J. Soc. Cosmet. Chem *34*, 465–476.

Wolpert, D.M., and Flanagan, J.R. (2001). Motor prediction. Curr. Biol. *11*, R729–R732.

Yoshioka, T., Bensmaia, S.J., Craig, J.C., and Hsiao, S.S. (2007). Texture perception through direct and indirect touch: an analysis of perceptual space for tactile textures in two modes of exploration. Somat. Mot Res *24*, 53–70.

You, Y., Wang, X., Wang, S., Pan, Y., and Zhou, J. (2008). A new method to demonstrate frustrated total internal reflection in the visible band. Am. J. Phys. *76*, 224–228.

Zhao, C.W., Daley, M.J., and Pruszynski, J.A. (2017). Neural network models of the tactile system develop first-order units with spatially complex receptive fields. bioRxiv.

Zhu, S., Yu, A.W., Hawley, D., and Roy, R. (1986). Frustrated total internal reflection: A demonstration and review. Am. J. Phys. *54*, 601–607.